MIT Libraries | DSpace@MIT

MIT Open Access Articles

Observation of single top quark production and measurement of |Vtb| with CDF

Massachusetts Institute of Technology

Observation of single top quark production and measurement of $|V_{tb}|$ with CDF

T. Aaltonen,[24] J. Adelman,[14] B. Álvarez González,[12,x] S. Amerio,[44b,44a] D. Amidei,[35] A. Anastassov,[39] A. Annovi,[20] J. Antos,[15] G. Apollinari,[18] J. Appel,[18] A. Apresyan,[49] T. Arisawa,[58] A. Artikov,[16] J. Asaadi,[54] W. Ashmanskas,[18] A. Attal,[4] A. Aurisano,[54] F. Azfar,[43] W. Badgett,[18] A. Barbaro-Galtieri,[29] V. E. Barnes,[49] B. A. Barnett,[26] P. Barria,[47c,47a] P. Bartos,[15] G. Bauer,[33] P.-H. Beauchemin,[34] F. Bedeschi,[47a] D. Beecher,[31] S. Behari,[26] G. Bellettini,[47b,47a] J. Bellinger,[60] D. Benjamin,[17] A. Beretvas,[18] A. Bhatti,[51] M. Binkley,[18,a] D. Bisello,[44b,44a] I. Bizjak,[31,ee] R. E. Blair,[2] C. Blocker,[7] B. Blumenfeld,[26] A. Bocci,[17] A. Bodek,[50] V. Boisvert,[50] D. Bortoletto,[49] J. Boudreau,[48] A. Boveia,[11] B. Brau,[11,b] A. Bridgeman,[25] L. Brigliadori,[6b,6a] C. Bromberg,[36] E. Brubaker,[14] J. Budagov,[16] H. S. Budd,[50] S. Budd,[25] K. Burkett,[18] G. Busetto,[44b,44a] P. Bussey,[22] A. Buzatu,[34] K. L. Byrum,[2] S. Cabrera,[17,z] C. Calancha,[32] S. Camarda,[4] M. Campanelli,[31] M. Campbell,[35] F. Canelli,[14,18] A. Canepa,[46] B. Carls,[25] D. Carlsmith,[60] R. Carosi,[47a] S. Carrillo,[19,o] S. Carron,[18] B. Casal,[12] M. Casarsa,[18] A. Castro,[6b,6a] P. Catastini,[47c,47a] D. Cauz,[55a] V. Cavaliere,[47c,47a] M. Cavalli-Sforza,[4] A. Cerri,[29] L. Cerrito,[31,r] S. H. Chang,[28] Y. C. Chen,[1] M. Chertok,[8] G. Chiarelli,[47a] G. Chlachidze,[18] F. Chlebana,[18] K. Cho,[28] D. Chokheli,[16] J. P. Chou,[23] K. Chung,[18,p] W. H. Chung,[60] Y. S. Chung,[50] T. Chwalek,[27] C. I. Ciobanu,[45] M. A. Ciocci,[47c,47a] A. Clark,[21] D. Clark,[7] G. Compostella,[44a] M. E. Convery,[18] J. Conway,[8] M. Corbo,[45] M. Cordelli,[20] C. A. Cox,[8] D. J. Cox,[8] F. Crescioli,[47b,47a] C. Cuenca Almenar,[61] J. Cuevas,[12,x] R. Culbertson,[18] J. C. Cully,[35] D. Dagenhart,[18] N. d'Ascenzo,[45,w] M. Datta,[18] T. Davies,[22] P. de Barbaro,[50] S. De Cecco,[52a] A. Deisher,[29] G. De Lorenzo,[4] M. Dell'Orso,[47b,47a] C. Deluca,[4] L. Demortier,[51] J. Deng,[17,g] M. Deninno,[6a] M. d'Errico,[44b,44a] A. Di Canto,[47b,47a] B. Di Ruzza,[47a] J. R. Dittmann,[5] M. D'Onofrio,[4] S. Donati,[47b,47a] P. Dong,[18] T. Dorigo,[44a] S. Dube,[53] K. Ebina,[58] A. Elagin,[54] R. Erbacher,[8] D. Errede,[25] S. Errede,[25] N. Ershaidat,[45,dd] R. Eusebi,[54] H. C. Fang,[29] S. Farrington,[43] W. T. Fedorko,[14] R. G. Feild,[61] M. Feindt,[27] J. P. Fernandez,[32] C. Ferrazza,[47d,47a] R. Field,[19] G. Flanagan,[49,t] R. Forrest,[8] M. J. Frank,[5] M. Franklin,[23] J. C. Freeman,[18] I. Furic,[19] M. Gallinaro,[51] J. Galyardt,[13] F. Garberson,[11] J. E. Garcia,[21] A. F. Garfinkel,[49] P. Garosi,[47c,47a] H. Gerberich,[25] D. Gerdes,[35] A. Gessler,[27] S. Giagu,[52b,52a] V. Giakoumopoulou,[3] P. Giannetti,[47a] K. Gibson,[48] J. L. Gimmell,[50] C. M. Ginsburg,[18] N. Giokaris,[3] M. Giordani,[55b,55a] P. Giromini,[20] M. Giunta,[47a] G. Giurgiu,[26] V. Glagolev,[16] D. Glenzinski,[18] M. Gold,[38] N. Goldschmidt,[19] A. Golossanov,[18] G. Gomez,[12] G. Gomez-Ceballos,[33] M. Goncharov,[33] O. González,[32] I. Gorelov,[38] A. T. Goshaw,[17] K. Goulianos,[51] A. Gresele,[44b,44a] S. Grinstein,[4] C. Grosso-Pilcher,[14] R. C. Group,[18] U. Grundler,[25] J. Guimaraes da Costa,[23] Z. Gunay-Unalan,[36] C. Haber,[29] S. R. Hahn,[18] E. Halkiadakis,[53] B.-Y. Han,[50] J. Y. Han,[50] F. Happacher,[20] K. Hara,[56] D. Hare,[53] M. Hare,[57] R. F. Harr,[59] M. Hartz,[48] K. Hatakeyama,[5] C. Hays,[43] M. Heck,[27] J. Heinrich,[46] M. Herndon,[60] J. Heuser,[27] S. Hewamanage,[5] D. Hidas,[53] C. S. Hill,[11,d] D. Hirschbuehl,[27] A. Hocker,[18] S. Hou,[1] M. Houlden,[30] S.-C. Hsu,[29] R. E. Hughes,[40] M. Hurwitz,[14] U. Husemann,[61] M. Hussein,[36] J. Huston,[36] J. Incandela,[11] G. Introzzi,[47a] M. Iori,[52b,52a] A. Ivanov,[8,q] E. James,[18] D. Jang,[13] B. Jayatilaka,[17] E. J. Jeon,[28] M. K. Jha,[6a] S. Jindariani,[18] W. Johnson,[8] M. Jones,[49] K. K. Joo,[28] S. Y. Jun,[13] J. E. Jung,[28] T. R. Junk,[18] T. Kamon,[54] D. Kar,[19] P. E. Karchin,[59] Y. Kato,[42,n] R. Kephart,[18] W. Ketchum,[14] J. Keung,[46] V. Khotilovich,[54] B. Kilminster,[18] D. H. Kim,[28] H. S. Kim,[28] H. W. Kim,[28] J. E. Kim,[28] M. J. Kim,[20] S. B. Kim,[28] S. H. Kim,[56] Y. K. Kim,[14] N. Kimura,[58] L. Kirsch,[7] S. Klimenko,[19] K. Kondo,[58] D. J. Kong,[28] J. Konigsberg,[19] A. Korytov,[19] A. V. Kotwal,[17] M. Kreps,[27] J. Kroll,[46] D. Krop,[14] N. Krumnack,[5] M. Kruse,[17] V. Krutelyov,[11] T. Kuhr,[27] N. P. Kulkarni,[59] M. Kurata,[56] S. Kwang,[14] A. T. Laasanen,[49] S. Lami,[47a] S. Lammel,[18] M. Lancaster,[31] R. L. Lander,[8] K. Lannon,[40,v] A. Lath,[53] G. Latino,[47c,47a] I. Lazzizzera,[44b,44a] T. LeCompte,[2] E. Lee,[54] H. S. Lee,[14] J. S. Lee,[28] S. W. Lee,[54,y] S. Leone,[47a] J. D. Lewis,[18] C.-J. Lin,[29] J. Linacre,[43] M. Lindgren,[18] E. Lipeles,[46] A. Lister,[21] D. O. Litvintsev,[18] C. Liu,[48] T. Liu,[18] N. S. Lockyer,[46] A. Loginov,[61] L. Lovas,[15] D. Lucchesi,[44b,44a] J. Lueck,[27] P. Lujan,[29] P. Lukens,[18] G. Lungu,[51] J. Lys,[29] R. Lysak,[15] D. MacQueen,[34] R. Madrak,[18] K. Maeshima,[18] K. Makhoul,[33] P. Maksimovic,[26] S. Malde,[43] S. Malik,[31] G. Manca,[30,f] A. Manousakis-Katsikakis,[3] F. Margaroli,[49] C. Marino,[27] C. P. Marino,[25] A. Martin,[61] V. Martin,[22,l] M. Martínez,[4] R. Martínez-Ballarín,[32] P. Mastrandrea,[52a] M. Mathis,[26] M. E. Mattson,[59] P. Mazzanti,[6a] K. S. McFarland,[50] P. McIntyre,[54] R. McNulty,[30,k] A. Mehta,[30] P. Mehtala,[24] A. Menzione,[47a] C. Mesropian,[51] T. Miao,[18] D. Mietlicki,[35] N. Miladinovic,[7] R. Miller,[36] C. Mills,[23] M. Milnik,[27] A. Mitra,[1] G. Mitselmakher,[19] H. Miyake,[56] S. Moed,[23] N. Moggi,[6a] M. N. Mondragon,[18,o] C. S. Moon,[28] R. Moore,[18] M. J. Morello,[47a] J. Morlock,[27] P. Movilla Fernandez,[18] J. Mülmenstädt,[29] A. Mukherjee,[18] Th. Muller,[27] P. Murat,[18] M. Mussini,[6b,6a] J. Nachtman,[18,p] Y. Nagai,[56] J. Naganoma,[56] K. Nakamura,[56] I. Nakano,[41] A. Napier,[57] J. Nett,[60] C. Neu,[46,bb] M. S. Neubauer,[25] S. Neubauer,[27] J. Nielsen,[29,h] L. Nodulman,[2] M. Norman,[10] O. Norniella,[25] E. Nurse,[31] L. Oakes,[43] S. H. Oh,[17] Y. D. Oh,[28] I. Oksuzian,[19] T. Okusawa,[42] R. Orava,[24] K. Osterberg,[24] S. Pagan Griso,[44b,44a] C. Pagliarone,[55a] E. Palencia,[18] V. Papadimitriou,[18] A. Papaikonomou,[27] A. A. Paramonov,[2] B. Parks,[40] S. Pashapour,[34]

J. Patrick,[18] G. Pauletta,[55b,55a] M. Paulini,[13] C. Paus,[33] T. Peiffer,[27] D. E. Pellett,[8] A. Penzo,[55a] T. J. Phillips,[17] G. Piacentino,[47a] E. Pianori,[46] L. Pinera,[19] K. Pitts,[25] C. Plager,[9] L. Pondrom,[60] K. Potamianos,[49] O. Poukhov,[16,a] F. Prokoshin,[16,aa] A. Pronko,[18] F. Ptohos,[18,j] E. Pueschel,[13] G. Punzi,[47b,47a] J. Pursley,[60] J. Rademacker,[43,d] A. Rahaman,[48] V. Ramakrishnan,[60] N. Ranjan,[49] I. Redondo,[32] P. Renton,[43] M. Renz,[27] M. Rescigno,[52a] S. Richter,[27] F. Rimondi,[6b,6a] L. Ristori,[47a] A. Robson,[22] T. Rodrigo,[12] T. Rodriguez,[46] E. Rogers,[25] S. Rolli,[57] R. Roser,[18] M. Rossi,[55a] R. Rossin,[11] P. Roy,[34] A. Ruiz,[12] J. Russ,[13] V. Rusu,[18] B. Rutherford,[18] H. Saarikko,[24] A. Safonov,[54] W. K. Sakumoto,[50] L. Santi,[55b,55a] L. Sartori,[47a] K. Sato,[56] V. Saveliev,[45,w] A. Savoy-Navarro,[45] P. Schlabach,[18] A. Schmidt,[27] E. E. Schmidt,[18] M. A. Schmidt,[14] M. P. Schmidt,[61,a] M. Schmitt,[39] T. Schwarz,[8] L. Scodellaro,[12] A. Scribano,[47c,47a] F. Scuri,[47a] A. Sedov,[49] S. Seidel,[38] Y. Seiya,[42] A. Semenov,[16] L. Sexton-Kennedy,[18] F. Sforza,[47b,47a] A. Sfyrla,[25] S. Z. Shalhout,[59] T. Shears,[30] P. F. Shepard,[48] M. Shimojima,[56,u] S. Shiraishi,[14] M. Shochet,[14] Y. Shon,[60] I. Shreyber,[37] A. Simonenko,[16] P. Sinervo,[34] A. Sisakyan,[16] A. J. Slaughter,[18] J. Slaunwhite,[40] K. Sliwa,[57] J. R. Smith,[8] F. D. Snider,[18] R. Snihur,[34] A. Soha,[18] S. Somalwar,[53] V. Sorin,[4] P. Squillacioti,[47c,47a] M. Stanitzki,[61] R. St. Denis,[22] B. Stelzer,[34] O. Stelzer-Chilton,[34] D. Stentz,[39] J. Strologas,[38] G. L. Strycker,[35] J. S. Suh,[28] A. Sukhanov,[19] I. Suslov,[16] A. Taffard,[25,g] R. Takashima,[41] Y. Takeuchi,[56] R. Tanaka,[41] J. Tang,[14] M. Tecchio,[35] P. K. Teng,[1] J. Thom,[18,i] J. Thome,[13] G. A. Thompson,[25] E. Thomson,[46] P. Tipton,[61] P. Ttito-Guzmán,[32] S. Tkaczyk,[18] D. Toback,[54] S. Tokar,[15] K. Tollefson,[36] T. Tomura,[56] D. Tonelli,[18] S. Torre,[20] D. Torretta,[18] P. Totaro,[55b,55a] M. Trovato,[47d,47a] S.-Y. Tsai,[1] Y. Tu,[46] N. Turini,[47c,47a] F. Ukegawa,[56] S. Uozumi,[28] N. van Remortel,[24,c] A. Varganov,[35] E. Vataga,[47d,47a] F. Vázquez,[19,o] G. Velev,[18] C. Vellidis,[3] M. Vidal,[32] I. Vila,[12] R. Vilar,[12] M. Vogel,[38] I. Volobouev,[29,y] G. Volpi,[47b,47a] P. Wagner,[46] R. G. Wagner,[2] R. L. Wagner,[18] W. Wagner,[27,cc] J. Wagner-Kuhr,[27] T. Wakisaka,[42] R. Wallny,[9] S. M. Wang,[1] A. Warburton,[34] D. Waters,[31] M. Weinberger,[54] J. Weinelt,[27] W. C. Wester III,[18] B. Whitehouse,[57] D. Whiteson,[46,g] A. B. Wicklund,[2] E. Wicklund,[18] S. Wilbur,[14] G. Williams,[34] H. H. Williams,[46] P. Wilson,[18] B. L. Winer,[40] P. Wittich,[18,i] S. Wolbers,[18] C. Wolfe,[14] H. Wolfe,[40] T. Wright,[35] X. Wu,[21] F. Würthwein,[10] A. Yagil,[10] K. Yamamoto,[42] J. Yamaoka,[17] U. K. Yang,[14,s] Y. C. Yang,[28] W. M. Yao,[29] G. P. Yeh,[18] K. Yi,[18,p] J. Yoh,[18] K. Yorita,[58] T. Yoshida,[42,m] G. B. Yu,[17] I. Yu,[28] S. S. Yu,[18] J. C. Yun,[18] A. Zanetti,[55a] Y. Zeng,[17] X. Zhang,[25] Y. Zheng,[9,e] and S. Zucchelli[6b,6a]

(CDF Collaboration)

[1]*Institute of Physics, Academia Sinica, Taipei, Taiwan 11529, Republic of China*
[2]*Argonne National Laboratory, Argonne, Illinois 60439, USA*
[3]*University of Athens, 157 71 Athens, Greece*
[4]*Institut de Fisica d'Altes Energies, Universitat Autonoma de Barcelona, E-08193, Bellaterra (Barcelona), Spain*
[5]*Baylor University, Waco, Texas 76798, USA*
[6a]*Istituto Nazionale di Fisica Nucleare Bologna, I-40127 Bologna, Italy;*
[6b]*University of Bologna, I-40127 Bologna, Italy*
[7]*Brandeis University, Waltham, Massachusetts 02254, USA*
[8]*University of California, Davis, Davis, California 95616, USA*
[9]*University of California, Los Angeles, Los Angeles, California 90024, USA*
[10]*University of California, San Diego, La Jolla, California 92093, USA*
[11]*University of California, Santa Barbara, Santa Barbara, California 93106, USA*
[12]*Instituto de Fisica de Cantabria, CSIC-University of Cantabria, 39005 Santander, Spain*
[13]*Carnegie Mellon University, Pittsburgh, Pennsylvania 15213, USA*
[14]*Enrico Fermi Institute, University of Chicago, Chicago, Illinois 60637, USA*
[15]*Comenius University, 842 48 Bratislava, Slovakia; Institute of Experimental Physics, 040 01 Kosice, Slovakia*
[16]*Joint Institute for Nuclear Research, RU-141980 Dubna, Russia*
[17]*Duke University, Durham, North Carolina 27708, USA*
[18]*Fermi National Accelerator Laboratory, Batavia, Illinois 60510, USA*
[19]*University of Florida, Gainesville, Florida 32611, USA*
[20]*Laboratori Nazionali di Frascati, Istituto Nazionale di Fisica Nucleare, I-00044 Frascati, Italy*
[21]*University of Geneva, CH-1211 Geneva 4, Switzerland*
[22]*Glasgow University, Glasgow G12 8QQ, United Kingdom*
[23]*Harvard University, Cambridge, Massachusetts 02138, USA*
[24]*Division of High Energy Physics, Department of Physics, University of Helsinki and Helsinki Institute of Physics, FIN-00014, Helsinki, Finland*
[25]*University of Illinois, Urbana, Illinois 61801, USA*
[26]*The Johns Hopkins University, Baltimore, Maryland 21218, USA*
[27]*Institut für Experimentelle Kernphysik, Karlsruhe Institute of Technology, D-76131 Karlsruhe, Germany*

[28]Center for High Energy Physics: Kyungpook National University, Daegu 702-701, Korea;
Seoul National University, Seoul 151-742, Korea;
Sungkyunkwan University, Suwon 440-746, Korea;
Korea Institute of Science and Technology Information, Daejeon 305-806, Korea;
Chonnam National University, Gwangju 500-757, Korea;
Chonbuk National University, Jeonju 561-756, Korea
[29]Ernest Orlando Lawrence Berkeley National Laboratory, Berkeley, California 94720, USA
[30]University of Liverpool, Liverpool L69 7ZE, United Kingdom
[31]University College London, London WC1E 6BT, United Kingdom
[32]Centro de Investigaciones Energeticas Medioambientales y Tecnologicas, E-28040 Madrid, Spain
[33]Massachusetts Institute of Technology, Cambridge, Massachusetts 02139, USA
[34]Institute of Particle Physics, McGill University, Montréal, Québec, Canada H3A 2T8;
Simon Fraser University, Burnaby, British Columbia, Canada V5A 1S6;
University of Toronto, Toronto, Ontario, Canada M5S 1A7;
and TRIUMF, Vancouver, British Columbia, Canada V6T 2A3
[35]University of Michigan, Ann Arbor, Michigan 48109, USA
[36]Michigan State University, East Lansing, Michigan 48824, USA
[37]Institution for Theoretical and Experimental Physics, ITEP, Moscow 117259, Russia
[38]University of New Mexico, Albuquerque, New Mexico 87131, USA
[39]Northwestern University, Evanston, Illinois 60208, USA
[40]The Ohio State University, Columbus, Ohio 43210, USA
[41]Okayama University, Okayama 700-8530, Japan
[42]Osaka City University, Osaka 588, Japan
[43]University of Oxford, Oxford OX1 3RH, United Kingdom
[44a]Istituto Nazionale di Fisica Nucleare, Sezione di Padova-Trento, I-35131 Padova, Italy;
[44b]University of Padova, I-35131 Padova, Italy
[45]LPNHE, Universite Pierre et Marie Curie/IN2P3-CNRS, UMR7585, Paris, F-75252 France
[46]University of Pennsylvania, Philadelphia, Pennsylvania 19104
[47a]Istituto Nazionale di Fisica Nucleare Pisa, I-56127 Pisa, Italy;
[47b]University of Pisa, I-56127 Pisa, Italy;
[47c]University of Siena, I-53100 Siena, Italy;

[a]Deceased

[b]Visitor from University of Massachusetts Amherst, Amherst, MA 01003, USA

[c]Visitor from Universiteit Antwerpen, B-2610 Antwerp, Belgium

[d]Visitor from University of Bristol, Bristol BS8 1TL, United Kingdom

[e]Visitor from Chinese Academy of Sciences, Beijing 100864, China

[f]Visitor from Istituto Nazionale di Fisica Nucleare, Sezione di Cagliari, 09042 Monserrato (Cagliari), Italy

[g]Visitor from University of California Irvine, Irvine, CA 92697, USA

[h]Visitor from University of California Santa Cruz, Santa Cruz, CA 95064, USA

[i]Visitor from Cornell University, Ithaca, NY 14853, USA

[j]Visitor from University of Cyprus, Nicosia CY-1678, Cyprus

[k]Visitor from University College Dublin, Dublin 4, Ireland

[l]Visitor from University of Edinburgh, Edinburgh EH9 3JZ, United Kingdom

[m]Visitor from University of Fukui, Fukui City, Fukui Prefecture, Japan 910-0017

[n]Visitor from Kinki University, Higashi-Osaka City, Japan 577-8502

[o]Visitor from Universidad Iberoamericana, Mexico D.F., Mexico

[p]Visitor from University of Iowa, IA City, IA 52242, USA

[q]Visitor from Kansas State University, Manhattan, KS 66506, USA

[r]Visitor from Queen Mary, University of London, London, E1 4NS, England

[s]Visitor from University of Manchester, Manchester M13 9PL, England

[t]Visitor from Muons, Inc., Batavia, IL 60510, USA

[u]Visitor from Nagasaki Institute of Applied Science, Nagasaki, Japan

[v]Visitor from University of Notre Dame, Notre Dame, IN 46556, USA

[w]Visitor from Obninsk State University, Obninsk, Russia

[x]Visitor from University de Oviedo, E-33007 Oviedo, Spain

[y]Visitor from Texas Tech University, Lubbock, TX 79609, USA

[z]Visitor from IFIC(CSIC-Universitat de Valencia), 56071 Valencia, Spain

[aa]Visitor from Universidad Tecnica Federico Santa Maria, 110v Valparaiso, Chile

[bb]Visitor from University of Virginia, Charlottesville, VA 22906, USA

[cc]Visitor from Bergische Universität Wuppertal, 42097 Wuppertal, Germany

[dd]Visitor from Yarmouk University, Irbid 211-63, Jordan

[ee]On leave from J. Stefan Institute, Ljubljana, Slovenia

[47d]*Scuola Normale Superiore, I-56127 Pisa, Italy*
[48]*University of Pittsburgh, Pittsburgh, Pennsylvania 15260, USA*
[49]*Purdue University, West Lafayette, Indiana 47907, USA*
[50]*University of Rochester, Rochester, New York 14627, USA*
[51]*The Rockefeller University, New York, New York 10021, USA*
[52a]*Istituto Nazionale di Fisica Nucleare, Sezione di Roma 1, I-00185 Roma, Italy;*
[52b]*Sapienza Università di Roma, I-00185 Roma, Italy*
[53]*Rutgers University, Piscataway, New Jersey 08855, USA*
[54]*Texas A&M University, College Station, Texas 77843, USA*
[55a]*Istituto Nazionale di Fisica Nucleare Trieste/Udine, I-34100 Trieste, I-33100 Udine, Italy;*
[55b]*University of Trieste/Udine, I-33100 Udine, Italy*
[56]*University of Tsukuba, Tsukuba, Ibaraki 305, Japan*
[57]*Tufts University, Medford, Massachusetts 02155, USA*
[58]*Waseda University, Tokyo 169, Japan*
[59]*Wayne State University, Detroit, Michigan 48201, USA*
[60]*University of Wisconsin, Madison, Wisconsin 53706, USA*
[61]*Yale University, New Haven, Connecticut 06520, USA*

We report the observation of electroweak single top quark production in 3.2 fb^{-1} of $p\bar{p}$ collision data collected by the Collider Detector at Fermilab at $\sqrt{s} = 1.96$ TeV. Candidate events in the W + jets topology with a leptonically decaying W boson are classified as signal-like by four parallel analyses based on likelihood functions, matrix elements, neural networks, and boosted decision trees. These results are combined using a super discriminant analysis based on genetically evolved neural networks in order to improve the sensitivity. This combined result is further combined with that of a search for a single top quark signal in an orthogonal sample of events with missing transverse energy plus jets and no charged lepton. We observe a signal consistent with the standard model prediction but inconsistent with the background-only model by 5.0 standard deviations, with a median expected sensitivity in excess of 5.9 standard deviations. We measure a production cross section of $2.3^{+0.6}_{-0.5}$(stat + sys) pb, extract the value of the Cabibbo-Kobayashi-Maskawa matrix element $|V_{tb}| = 0.91^{+0.11}_{-0.11}$(stat + sys) $\pm$ 0.07 (theory), and set a lower limit $|V_{tb}| > 0.71$ at the 95% C.L., assuming $m_t = 175$ GeV/c^2.

I. INTRODUCTION

The top quark is the most massive known elementary particle. Its mass, m_t, is 173.3 ± 1.1 GeV/c^2 [1], about 40 times larger than that of the bottom quark, the second-most massive standard model (SM) fermion. The top quark's large mass, at the scale of electroweak symmetry breaking, hints that it may play a role in the mechanism of mass generation. The presence of the top quark was established in 1995 by the CDF and D0 Collaborations with approximately 60 pb^{-1} of $p\bar{p}$ data collected per collaboration at $\sqrt{s} = 1.8$ TeV [2,3] in Run I at the Fermilab Tevatron. The production mechanism used in the observation of the top quark was $t\bar{t}$ pair production via the strong interaction.

Since then, larger data samples have enabled detailed study of the top quark. The $t\bar{t}$ production cross section [4], the top quark's mass [1], the top quark decay branching fraction to Wb [5], and the polarization of W bosons in top quark decay [6] have been measured precisely. Nonetheless, many properties of the top quark have not yet been tested as precisely. In particular, the Cabibbo-Kobayashi-Maskawa (CKM) matrix element V_{tb} remains poorly constrained by direct measurements [7]. The strength of the coupling, $|V_{tb}|$, governs the decay rate of

the top quark and its decay width into Wb; other decays are expected to have much smaller branching fractions. Using measurements of the other CKM matrix elements, and assuming a three-generation SM with a 3×3 unitary CKM matrix, $|V_{tb}|$ is expected to be very close to unity.

Top quarks are also expected to be produced singly in $p\bar{p}$ collisions via weak, charged-current interactions. The dominant processes at the Tevatron are the *s*-channel process, shown in Fig. 1(a), and the *t*-channel process [8], shown in Fig. 1(b). The next-to-leading-order (NLO) cross
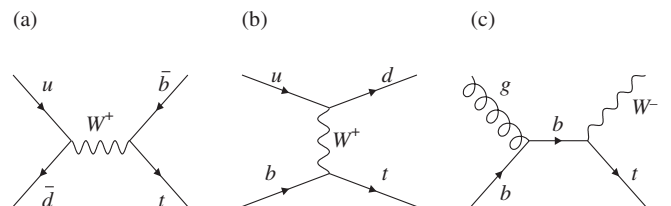

FIG. 1. Representative Feynman diagrams of single top quark production. Figures (a) and (b) are *s*- and *t*-channel processes, respectively, while figure (c) is associated Wt production, which contributes a small amount to the expected cross section at the Tevatron.

sections for these two processes are $\sigma_s = 0.88 \pm 0.11$ pb and $\sigma_t = 1.98 \pm 0.25$ pb, respectively [9,10]. This cross-section is the sum of the single t and the single $\bar{t}$ predictions. Throughout this paper, charge conjugate states are implied; all cross sections and yields are shown summed over charge conjugate states. A calculation has been performed resumming soft gluon corrections and calculating finite-order expansions through next-to-next-to-next-to-leading order (NNNLO) [11], yielding $\sigma_s = 0.98 \pm 0.04$ pb and $\sigma_t = 2.16 \pm 0.12$ pb, also assuming $m_t = 175$ GeV/c^2. Newer calculations are also available [12–14]. A third process, the associated production of a W boson and a top quark, shown in Fig. 1(c), has a very small expected cross section at the Tevatron.

Measuring the two cross sections σ_s and σ_t provides a direct determination of $|V_{tb}|$, allowing an overconstrained test of the unitarity of the CKM matrix, as well as an indirect determination of the top quark's lifetime. We assume that the top quark decays to Wb 100% of the time in order to measure the production cross sections. This assumption does not constrain $|V_{tb}|$ to be near unity, but instead it is the same as assuming $|V_{tb}|^2 \gg |V_{ts}|^2 + |V_{td}|^2$. Many extensions to the SM predict measurable deviations of σ_s or σ_t from their SM values. One of the simplest of these is the hypothesis that a fourth generation of fermions exists beyond the three established ones. Aside from the constraint that its neutrino must be heavier than $M_Z/2$ [15] and that the quarks must escape current experimental limits, the existence of a fourth generation of fermions remains possible. If these additional sequential fermions exist, then a 4×4 version of the CKM matrix would be unitary, and the 3×3 submatrix may not necessarily be unitary. The presence of a fourth generation would in general reduce $|V_{tb}|$, thereby reducing the single top quark production cross sections σ_s and σ_t. Precision electroweak constraints provide some information on possible values of $|V_{tb}|$ in this extended scenario [16], but a direct measurement provides a test with no additional model dependence.

Other new physics scenarios predict larger values of σ_s and σ_t than those expected in the SM. A flavor-changing Ztc coupling, for example, would manifest itself in the production of $p\bar{p} \rightarrow t\bar{c}$ events, which may show up in either the measured value of σ_s or σ_t depending on the relative acceptances of the measurement channels. An additional charged gauge boson W' may also enhance the production cross sections. A review of new physics models affecting the single top quark production cross section and polarization properties is given in [17].

Even in the absence of new physics, assuming the SM constraints on $|V_{tb}|$, a measurement of the t-channel single top production cross section provides a test of the b parton distribution function of the proton.

Single top quark production is one of the background processes in the search for the Higgs boson H in the $WH \rightarrow \ell\nu b\bar{b}$ channel, since they share the same final state, and a direct measurement of single top quark production may improve the sensitivity of the Higgs boson search. Furthermore, the backgrounds to the single top quark search are backgrounds to the Higgs boson search. Careful understanding of these backgrounds lays the groundwork for future Higgs boson searches. Since the single top quark processes have larger cross sections than the Higgs boson signal in the $WH \rightarrow \ell\nu b\bar{b}$ mode [18], and since the single top signal is more distinct from the backgrounds than the Higgs boson signal is, we must pass the milestone of observing single top quark production along the way to testing for Higgs boson production.

Measuring the single top quark cross section is well motivated but it is also extremely challenging at the Tevatron. The total production cross section is expected to be about one-half of that of $t\bar{t}$ production [19], and with only one top quark in the final state instead of two, the signal is far less distinct from the dominant background processes than $t\bar{t}$ production is. The rate at which a W boson is produced along with jets, at least one of which must have a displaced vertex which passes our requirements for B hadron identification (we say in this paper that such jets are b-tagged), is approximately 12 times the signal rate. The *a priori* uncertainties on the background processes are about a factor of 3 larger than the expected signal rate. In order to expect to observe single top quark production, the background rates must be small and well constrained, and the expected signal must be much larger than the uncertainty on the background. A much more pure sample of signal events therefore must be separated from the background processes in order to make observation possible.

Single top quark production is characterized by a number of kinematic properties. The top quark mass is known, and precise predictions of the distributions of observable quantities for the top quark and the recoil products are also available. Top quarks produced singly via the weak interaction are expected to be nearly 100% polarized [20,21]. The background $W +$ jets and $t\bar{t}$ processes have characteristics which differ from those of single top quark production. Kinematic properties, coupled with the b-tagging requirement, provide the keys to purification of the signal. Because signal events differ from background events in several ways, such as in the distribution of the invariant mass of the final-state objects assigned to be the decay products of the top quark and the rapidity of the recoiling jets, and because the task of observing single top quark production requires the maximum separation, we apply multivariate techniques. The techniques described in this paper together achieve a signal-to-background ratio of more than 5:1 in a subset of events with a significant signal expectation. This high purity is needed in order to overcome the uncertainty in the background prediction.

The effect of the background uncertainty is reduced by fitting for both the signal and the background rates together

to the observed data distributions, a technique which is analogous to fitting the background in the sidebands of a mass peak, but which is applied in this case to multivariate discriminant distributions. Uncertainties are incurred in this procedure—the shapes of the background distributions are imperfectly known from simulations. We check in detail the modeling of the distributions of the inputs and the outputs of the multivariate techniques, using events passing our selection requirements, and also separately using events in control samples depleted in signal. We also check the modeling of the correlations between pairs of these variables. In general we find excellent agreement, with some imperfections. We assess uncertainties on the shapes of the discriminant outputs both from *a priori* uncertain parameters in the modeling, as well as from discrepancies observed in the modeling of the data by the Monte Carlo (MC) simulations. These shape uncertainties are included in the signal rate extraction and in the calculation of the significance.

Both the CDF and the D0 Collaborations have searched for single top quark production in $p\bar{p}$ collision data taken at $\sqrt{s} = 1.96$ TeV in Run II at the Fermilab Tevatron. The D0 Collaboration reported evidence for the production of single top quarks in 0.9 fb^{-1} of data [22,23] and observation of the process in 2.3 fb^{-1} [24]. More recently, D0 has conducted a measurement of the single top production cross section in the τ + jets final state using 4.8 fb^{-1} of data [25]. The CDF Collaboration reported evidence in 2.2 fb^{-1} of data [26] and observation in 3.2 fb^{-1} of data [27]. This paper describes in detail the four W + jets analyses of [27]; the analyses are based on multivariate likelihood functions (LF), artificial neural networks (NN), matrix elements (ME), and boosted decision trees (BDT). These analyses select events with a high-p_T charged lepton, large missing transverse energy $\not{E}_T$, and two or more jets, at least one of which is b tagged. Each analysis separately measures the single top quark production cross section and calculates the significance of the observed excess. We report here a single set of results and therefore must combine the information from each of the four analyses. Because there is 100% overlap in the data and Monte Carlo events selected by the analyses, a natural combination technique is to use the individual analyses' discriminant outputs as inputs to a super discriminant function evaluated for each event. The distributions of this super discriminant are then interpreted in the same way as those of each of the four component analyses.

A separate analysis is conducted on events without an identified charged lepton, in a data sample which corresponds to 2.1 fb^{-1} of data. Missing transverse energy plus jets, one of which is b tagged, is the signature used for this fifth analysis (MJ), which is described in detail in [28]. There is no overlap of events selected by the MJ analysis and the W + jets analyses. The results of this analysis are combined with the results of the super discriminant analysis to yield the final results: the measured total cross section $\sigma_s + \sigma_t$, $|V_{tb}|$, the separate cross sections σ_s and σ_t, and the statistical significance of the excess. With the combination of all analyses, we observe single top quark production with a significance of 5.0 standard deviations.

The analyses described in this paper were blind to the selected data when they were optimized for their expected sensitivities. Furthermore, since the publication of the 2.2 fb^{-1} W + jets results [26], the event selection requirements, the multivariate discriminants for the analyses shared with that result, and the systematic uncertainties remain unchanged; new data were added without further optimization or retraining. When the 2.2 fb^{-1} results were validated, they were done so in a blind fashion. The distributions of all relevant variables were first checked for accurate modeling by our simulations and data-based background estimations in control samples of data that do not overlap with the selected signal sample. Then the distributions of the discriminant input variables, and also other variables, were checked in the sample of events passing the selection requirements. After that, the modeling of the low signal-to-background portions of the final output histograms was checked. Only after all of these validation steps were completed were the data in the most sensitive regions revealed. Two new analyses, BDT and MJ, have been added for this paper, and they were validated in a similar way.

This paper is organized as follows: Sec. II describes the CDF II detector, Sec. III describes the event selection, Sec. IV describes the simulation of signal events and the acceptance of the signal, Sec. V describes the background rate and kinematic shape modeling, Sec. VI describes a neural-network flavor separator which helps separate b jets from others, Sec. VII describes the four W + jets multivariate analysis techniques, Sec. VIII describes the systematic uncertainties we assess, Sec. IX describes the statistical techniques for extraction of the signal cross section and the significance, Sec. X describes the super discriminant, Sec. XI presents our results for the cross section, $|V_{tb}|$, and the significance, Sec. XII describes an extraction of σ_s and σ_t in a joint fit, and Sec. XIII summarizes our results.

II. THE CDF II DETECTOR

The CDF II detector [29–31] is a general-purpose particle detector with azimuthal and forward-backward symmetry. Positions and angles are expressed in a cylindrical coordinate system, with the z axis directed along the proton beam. The azimuthal angle ϕ around the beam axis is defined with respect to a horizontal ray running outwards from the center of the Tevatron, and radii are measured with respect to the beam axis. The polar angle θ is defined with respect to the proton beam direction, and the pseudorapidity η is defined to be $\eta = -\ln[\tan(\theta/2)]$. The transverse energy (as measured by the calorimetry) and
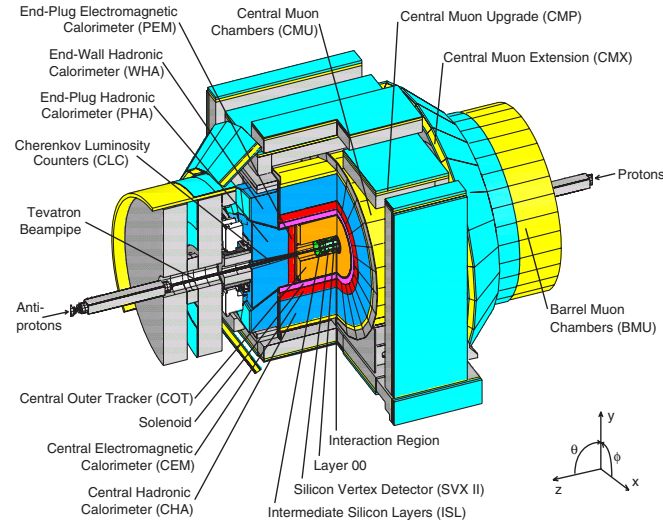
FIG. 2 (color online). Cutaway isometric view of the CDF II detector.

momentum (as measured by the tracking systems) of a particle are defined as $E_T = E \sin\theta$ and $p_T = p \sin\theta$, respectively. Figure 2 shows a cutaway isometric view of the CDF II detector.

A silicon tracking system and an open-cell drift chamber are used to measure the momenta of charged particles. The CDF II silicon tracking system consists of three subdetectors: a layer of single-sided silicon microstrip detectors, located immediately outside the beam pipe (layer 00) [32]; a five-layer, double-sided silicon microstrip detector (SVX II) covering the region between 2.5 to 11 cm from the beam axis [33]; and intermediate silicon layers (ISL) [34] located at radii between 19 cm and 29 cm which provide linking between track segments in the drift chamber and the SVX II. The typical intrinsic hit resolution of the silicon detector is 11 μm. The impact parameter resolution is $\sigma(d_0) \approx 40$ μm, of which approximately 35 μm is due to the transverse size of the Tevatron interaction region. The entire system reconstructs tracks in three dimensions with the precision needed to identify displaced vertices associated with b and c hadron decays.

The central outer tracker (COT) [35], the main tracking detector of CDF II, is an open-cell drift chamber, 3.1 m in length. It is segmented into eight concentric superlayers. The drift medium is a mixture of argon and ethane. Sense wires are arranged in eight alternating axial and $\pm 2°$ stereo superlayers with 12 layers of wires in each. The active volume covers the radial range from 40 cm to 137 cm. The tracking efficiency of the COT is nearly 100% in the range $|\eta| \leq 1$, and with the addition of silicon coverage, the tracks can be detected within the range $|\eta| < 1.8$.

The tracking systems are located within a superconducting solenoid, which has a diameter of 3.0 m, and which generates a 1.4 T magnetic field parallel to the beam axis. The magnetic field is used to measure the charged particle momentum transverse to the beamline. The momentum

resolution is $\sigma(p_T)/p_T \approx 0.1\% \cdot p_T$ for tracks within $|\eta| \leq 1.0$ and degrades with increasing $|\eta|$.

Front electromagnetic lead-scintillator sampling calorimeters [36,37] and rear hadronic iron-scintillator sampling calorimeters [38] surround the solenoid and measure the energy flow of interacting particles. They are segmented into projective towers, each one covering a small range in pseudorapidity and azimuth. The full array has an angular coverage of $|\eta| < 3.6$. The central region $|\eta| < 1.1$ is covered by the central electromagnetic calorimeter (CEM) and the central and end-wall hadronic calorimeters (CHA and WHA). The forward region $1.1 < |\eta| < 3.6$ is covered by the end-plug electromagnetic calorimeter (PEM) and the end-plug hadronic calorimeter (PHA). Energy deposits in the electromagnetic calorimeters are used for electron identification and energy measurement. The energy resolution for an electron with transverse energy E_T (measured in GeV) is given by $\sigma(E_T)/E_T \approx 13.5\%/\sqrt{E_T} \oplus 1.5\%$ and $\sigma(E_T)/E_T \approx 16.0\%/\sqrt{E_T} \oplus 1\%$ for electrons identified in the CEM and PEM, respectively. Jets are identified and measured through the energy they deposit in the electromagnetic and hadronic calorimeter towers. The calorimeters provide jet energy measurements with a resolution of approximately $\sigma(E_T) \approx 0.1 \cdot E_T + 1.0$ GeV [39]. The CEM and PEM calorimeters have two-dimensional readout strip detectors located at shower maximum [36,40]. These detectors provide higher resolution position measurements of electromagnetic showers than are available from the calorimeter tower segmentation alone, and also provide local energy measurements. The shower-maximum detectors contribute to the identification of electrons and photons, and help separate them from π^0 decays.

Beyond the calorimeters resides the muon system, which provides muon detection in the range $|\eta| < 1.5$. For the analyses presented in this article, muons are detected in four separate subdetectors. Muons with $p_T > 1.4$ GeV/c penetrating the five absorption lengths of the calorimeter are detected in the four layers of planar multiwire drift chambers of the central muon detector (CMU) [41]. Behind an additional 60 cm of steel, a second set of four layers of drift chambers, the central muon upgrade (CMP) [29,42], detects muons with $p_T > 2.2$ GeV/c. The CMU and CMP cover the same part of the central region $|\eta| < 0.6$. The central muon extension (CMX) [29,42] extends the pseudorapidity coverage of the muon system from 0.6 to 1.0 and thus completes the coverage over the full fiducial region of the COT. Muons with $1.0 < |\eta| < 1.5$ are detected by the barrel muon chambers (BMU) [43].

The Tevatron collider luminosity is determined with multicell gas Cherenkov detectors [44] located in the region $3.7 < |\eta| < 4.7$, which measure the average number of inelastic $p\bar{p}$ collisions per bunch crossing. The total uncertainty on the luminosity is $\pm 6.0\%$, of which 4.4% comes from the acceptance and the operation of the lumi-
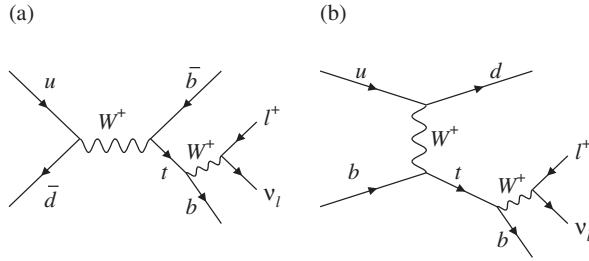
(a)   (b)

FIG. 3. Feynman diagrams showing the final states of the dominant (a) *s*-channel and (b) *t*-channel processes, with leptonic *W* boson decays. Both final states contain a charged lepton, a neutrino, and two jets, at least one of which originates from a *b* quark.

nosity monitor and 4.0% comes from the uncertainty of the inelastic $p\bar{p}$ cross section [45].

III. SELECTION OF CANDIDATE EVENTS

Single top quark events (see Fig. 3) have jets, a charged lepton, and a neutrino in the final state. The top quark decays into a W boson and a b quark before hadronizing. The quarks recoiling from the top quark, and the b quark from top quark decay, hadronize to form jets, motivating our event selection which requires two or three energetic jets (the third can come from a radiated gluon), at least one of which is b tagged, and the decay products of a W boson. In order to reduce background from multijet production via the strong interaction, we focus our event selection on the decays of the W boson to $e\nu_e$ or $\mu\nu_\mu$ in these analyses. Such events have one charged lepton (an electron or a muon), missing transverse energy resulting from the undetected neutrino, and at least two jets. These events constitute the W + jets sample. We also include the acceptance for signal and background events in which $W \rightarrow \tau\nu_\tau$, and the MJ analysis also is sensitive to W boson decays to τ leptons.

Since the $p\bar{p}$ collision rate at the Tevatron exceeds the rate at which events can be written to tape by 5 orders of magnitude, CDF has an elaborate trigger system with three levels. The first level uses special-purpose hardware [46] to reduce the event rate from the effective beam-crossing frequency of 1.7 MHz to approximately 15 kHz, the maximum rate at which the detector can be read out. The second level consists of a mixture of dedicated hardware and fast software algorithms and takes advantage of the full information read out of the detector [47]. At this level the trigger rate is reduced further to less than 800 Hz. At the third level, a computer farm running fast versions of the offline event reconstruction algorithms refines the trigger selections based on quantities that are nearly the same as those used in offline analyses [48]. In particular, detector calibrations are applied before the trigger requirements are imposed. The third-level trigger selects events for permanent storage at a rate of up to 200 Hz.

Many different trigger criteria are evaluated at each level, and events passing specific criteria at one level are considered by a subset of trigger algorithms at the next level. A cascading set of trigger requirements is known as a trigger path. This analysis uses the trigger paths which select events with high-p_T electron or muon candidates. The acceptance of these triggers for tau leptons is included in our rate estimates but the triggers are not optimized for identifying tau leptons. An additional trigger path, which requires significant $\not{E}_T$ plus at least two high-p_T jets, is also used to add W + jets candidate events with nontriggered leptons, which include charged leptons outside the fiducial volumes of the electron and muon detectors, as well as tau leptons.

The third-level central electron trigger requires a COT track with $p_T > 9$ GeV/c matched to an energy cluster in the CEM with $E_T > 18$ GeV. The shower profile of this cluster as measured by the shower-maximum detector is required to be consistent with those measured using test-beam electrons. Electron candidates with $|\eta| > 1.1$ are required to deposit more than 20 GeV in a cluster in the PEM, and the ratio of hadronic energy to electromagnetic energy E_{PHA}/E_{PEM} for this cluster is required to be less than 0.075. The third-level muon trigger requires a COT track with $p_T > 18$ GeV/c matched to a track segment in the muon chambers. The $\not{E}_T$ + jets trigger path requires $\not{E}_T > 35$ GeV and two jets with $E_T > 10$ GeV.

After offline reconstruction, we impose further requirements on the electron candidates in order to improve the purity of the sample. A reconstructed track with $p_T > 9$ GeV/c must match to a cluster in the CEM with $E_T > 20$ GeV. Furthermore, we require $E_{HAD}/E_{EM} < 0.055 + 0.00045 \times E/$GeV and the ratio of the energy of the cluster to the momentum of the track E/p has to be smaller than $2.0c$ for track momenta ≤ 50 GeV/c. For electron candidates with tracks with $p > 50$ GeV/c, no requirement on E/p is made as the misidentification rate is small. Candidate objects which fail these requirements are more likely to be hadrons or jets than those that pass.

Electron candidates in the forward direction (PHX) are defined by a cluster in the PEM with $E_T > 20$ GeV and $E_{HAD}/E_{EM} < 0.05$. The cluster position and the primary vertex position are combined to form a search trajectory in the silicon tracker and seed the pattern recognition of the tracking algorithm.

Electron candidates in the CEM and PHX are rejected if an additional high-p_T track is found which forms a common vertex with the track of the electron candidate and has the opposite sign of the curvature. These events are likely to stem from the conversion of a photon. Figure 4(a) shows the (η, ϕ) distributions of CEM and PHX electron candidates.

Muon candidates are identified by requiring the presence of a COT track with $p_T > 20$ GeV/c that extrapolates to a track segment in one or more muon chambers. The muon
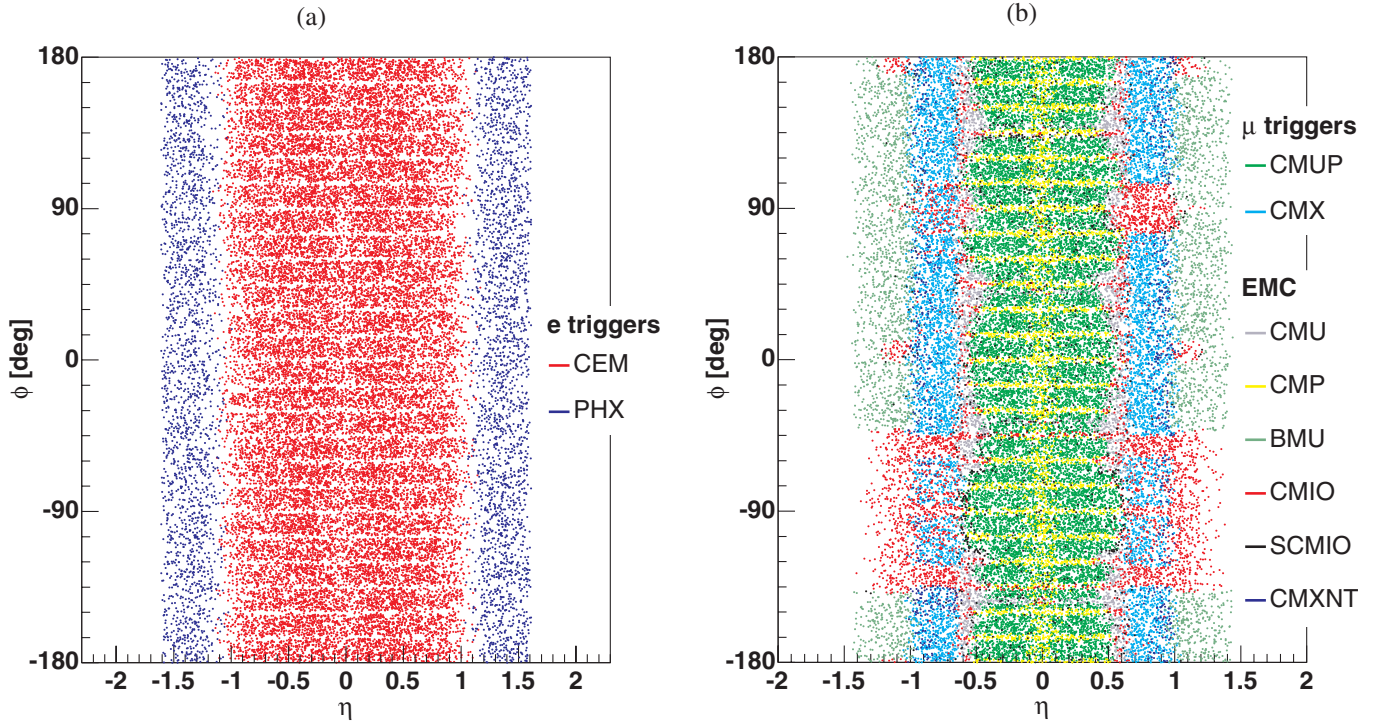
FIG. 4 (color online). Distributions in ($\phi - \eta$) space of the (a) electron and (b) muon selection categories, showing the coverage of the detector that each lepton category provides. The muon categories are more complicated due to the geometrical limitations of the several different muon detectors of CDF.

trigger may be satisfied by two types of muon candidates, called CMUP and CMX. A CMUP muon candidate is one in which track segments matched to the COT track are found in both the CMU and the CMP chambers. A CMX muon is one in which the track segment is found in the CMX muon detector. In order to minimize background contamination, further requirements are imposed. The energy deposition in the electromagnetic and hadronic calorimeters has to correspond to that expected from a minimum-ionizing particle. To reject cosmic-ray muons and muons from in-flight decays of long-lived particles such as K_S^0, K_L^0, and Λ particles, the distance of closest approach of the track to the beam line in the transverse plane is required to be less than 0.2 cm if there are no silicon hits on the muon candidate's track, and less than 0.02 cm if there are silicon hits. The remaining cosmic rays are reduced to a negligible level by taking advantage of their characteristic track timing and topology.

In order to add acceptance for events containing muons that cannot be triggered on directly, several additional muon types are taken from the extended muon coverage (EMC) of the $\not{E}_T$ + jets trigger path: a track segment only in the CMU and a COT track not pointing to CMP (CMU), a track segment only in the CMP and COT track not pointing to CMU (CMP), a track segment in the BMU (BMU), an isolated track not fiducial to any muon chambers (CMIO), an isolated track matched to a muon segment that is not considered fiducial to a muon detector (SCMIO),

and a track segment only in the CMX but in a region that can not be used in the trigger due to tracking limitations of the trigger (CMXNT). Figure 4(b) shows the (η, ϕ) distributions of muon candidates in each of these categories.

We require exactly one isolated charged lepton candidate with $|\eta| < 1.6$. A candidate is considered isolated if the E_T not assigned to the lepton inside a cone defined by $R \equiv \sqrt{(\Delta\eta)^2 + (\Delta\phi)^2} < 0.4$ centered around the lepton is less than 10% of the lepton E_T (p_T) for electrons (muons). This lepton is called a tight lepton. Loose charged lepton candidates pass all of the lepton selection criteria except for the isolation requirement. We reject events which have an additional tight or loose lepton candidate in order to reduce the Z/γ^* + jets and diboson background rates.

Jets are reconstructed using a cone algorithm by summing the transverse calorimeter energy E_T in a cone of radius $R \leq 0.4$. The energy deposition of an identified electron candidate, if present, is not included in the jet energy sum. The E_T of a cluster is calculated with respect to the z coordinate of the primary vertex of the event. The energy of each jet is corrected [49] for the η dependence and the nonlinearity of the calorimeter response. Routine calibrations of the calorimeter response are performed and these calibrations are included in the jet energy corrections. The jet energies are also adjusted by subtracting the extra deposition of energy from additional inelastic $p\bar{p}$ collisions on the same bunch crossing as the triggered event.

Reconstructed jets in events with identified charged lepton candidates must have corrected $E_T > 20$ GeV and detector $|\eta| < 2.8$. Detector η is defined as the pseudorapidity of the jet calculated with respect to the center of the detector. Only events with exactly two or three jets are accepted. At least one of the jets must be tagged as containing a B hadron by requiring a displaced secondary vertex within the jet, using the SECVTX algorithm [31]. Secondary vertices are accepted if the transverse decay length significance ($\Delta L_{xy}/\sigma_{xy}$) is greater than or equal to 7.5.

Events passing the $\not{E}_T$ + jets trigger path and the EMC muon segment requirements described above are also required to have two sufficiently separated jets: $\Delta R_{jj} > 1$. Furthermore, one of the jets must be central, with $|\eta_{jet}| < 0.9$, and both jets are required to have transverse energies above 25 GeV. These offline selection requirements ensure full efficiency of the $\not{E}_T$ + jets trigger path.

The vector missing E_T ($\vec{\not{E}}_T$) is defined by

$$\vec{\not{E}}_T = -\sum_i E_T^i \hat{n}_i, \tag{1}$$

$$i = \text{calorimeter tower number with } |\eta| < 3.6, \tag{2}$$

where $\hat{n}_i$ is a unit vector perpendicular to the beam axis and pointing at the i-th calorimeter tower. We also define $\not{E}_T = |\vec{\not{E}}_T|$. Since this calculation is based on calorimeter towers, $\not{E}_T$ is adjusted for the effect of the jet corrections for all jets.

A correction is applied to $\vec{\not{E}}_T$ for muons since they traverse the calorimeters without showering. The transverse momenta of all identified muons are added to the measured transverse energy sum and the average ionization energy is removed from the measured calorimeter energy deposits. We require the corrected $\not{E}_T$ to be greater than 25 GeV in order to purify a sample containing leptonic W boson decays.

A portion of the background consists of multijet events which do not contain W bosons. We call these "non-W" events below. We select against the non-W background by applying additional selection requirements which are based on the assumption that these events do not have a large $\not{E}_T$ from an escaping neutrino, but rather the $\not{E}_T$ that is observed comes from lost or mismeasured jets. In events lacking a W boson, one would expect small values of the transverse mass, defined as

$$M_T^W = \sqrt{2(p_T^\ell \not{E}_T - p_x^\ell \not{E}_T^x - p_y^\ell \not{E}_T^y)}. \tag{3}$$

Because the $\not{E}_T$ in events that do not contain W bosons often comes from jets which are erroneously identified as charged leptons, $\vec{\not{E}}_T$ often points close to the lepton candidate's direction, giving the event a low transverse mass. Thus, the transverse mass is required to be above 10 GeV for muons and 20 GeV for electrons, which have more of these events.

Further removal of non-W events is performed with a variable called $\not{E}_T$ significance ($\not{E}_{T,\text{sig}}$), defined as

$$\not{E}_{T,\text{sig}} = \frac{\not{E}_T}{\sqrt{\sum_{\text{jets}} C_{\text{JES}}^2 \cos^2(\Delta\phi_{\text{jet},\vec{\not{E}}_T}) E_{T,\text{jet}}^{\text{raw}} + \cos^2(\Delta\phi_{\vec{E}_{T,\text{uncl}},\vec{\not{E}}_T}) \sum E_{T,\text{uncl}}}}, \tag{4}$$

where C_{JES} is the jet energy correction factor [49], $E_{T,\text{jet}}^{\text{raw}}$ is a jet's energy before corrections are applied, $\vec{E}_{T,\text{uncl}}$ refers to the vector sum of the transverse components of calorimeter energy deposits not included in any reconstructed jets, and $\sum E_{T,\text{uncl}}$ is the sum of the magnitudes of these unclustered energies. The angle between the projections in the $r\phi$ plane of a jet and $\vec{\not{E}}_T$ is denoted $\Delta\phi_{\text{jet},\vec{E}_{T,\text{uncl}}}$, and the angle between the projections in the $r\phi$ plane of $\sum E_{T,\text{uncl}}$ and $\vec{\not{E}}_T$ is denoted $\Delta\phi_{\vec{E}_{T,\text{uncl}},\vec{\not{E}}_T}$. When the energies in Eq. (4) are measured in GeV, $\not{E}_{T,\text{sig}}$ is an approximate significance, as the dispersion in the measured $\not{E}_T$ in events with no true $\not{E}_T$ is approximated by the denominator. Central electron events are required to have $\not{E}_{T,\text{sig}} > 3.5 - 0.05 M_T$ and $\not{E}_{T,\text{sig}} > 2.5 - 3.125\Delta\phi_{\text{jet}2,\vec{\not{E}}_T}$, where jet 2 is the jet with the second-largest E_T, and all energies are measured in GeV. Plug electron events must have $\not{E}_{T,\text{sig}} > 2$ and $\not{E}_T > 45 - 30\Delta\phi_{\text{jet},\vec{\not{E}}_T}$ for all jets in the event. These requirements reduce the amount of contamination from non-W events substantially, as shown in the plots in Fig. 5.

To remove events containing Z bosons, we reject events in which the trigger lepton candidate can be paired with an oppositely signed track such that the invariant mass of the pair is within the range 76 GeV/$c^2 \leq m_{\ell,\text{track}} \leq 106$ GeV/c^2. Additionally, if the trigger lepton candidate is identified as an electron, the event is rejected if a cluster is found in the electromagnetic calorimeter that, when paired with the trigger lepton candidate, forms an invariant mass in the same range.

IV. SIGNAL MODEL

In order to perform a search for a previously undetected signal such as single top quark production, accurate models predicting the characteristics of expected data are needed for both the signal being tested and the SM background processes. This analysis uses Monte Carlo programs to generate simulated events for each signal and background process, except for non-W QCD multijet events for which events in data control samples are used.
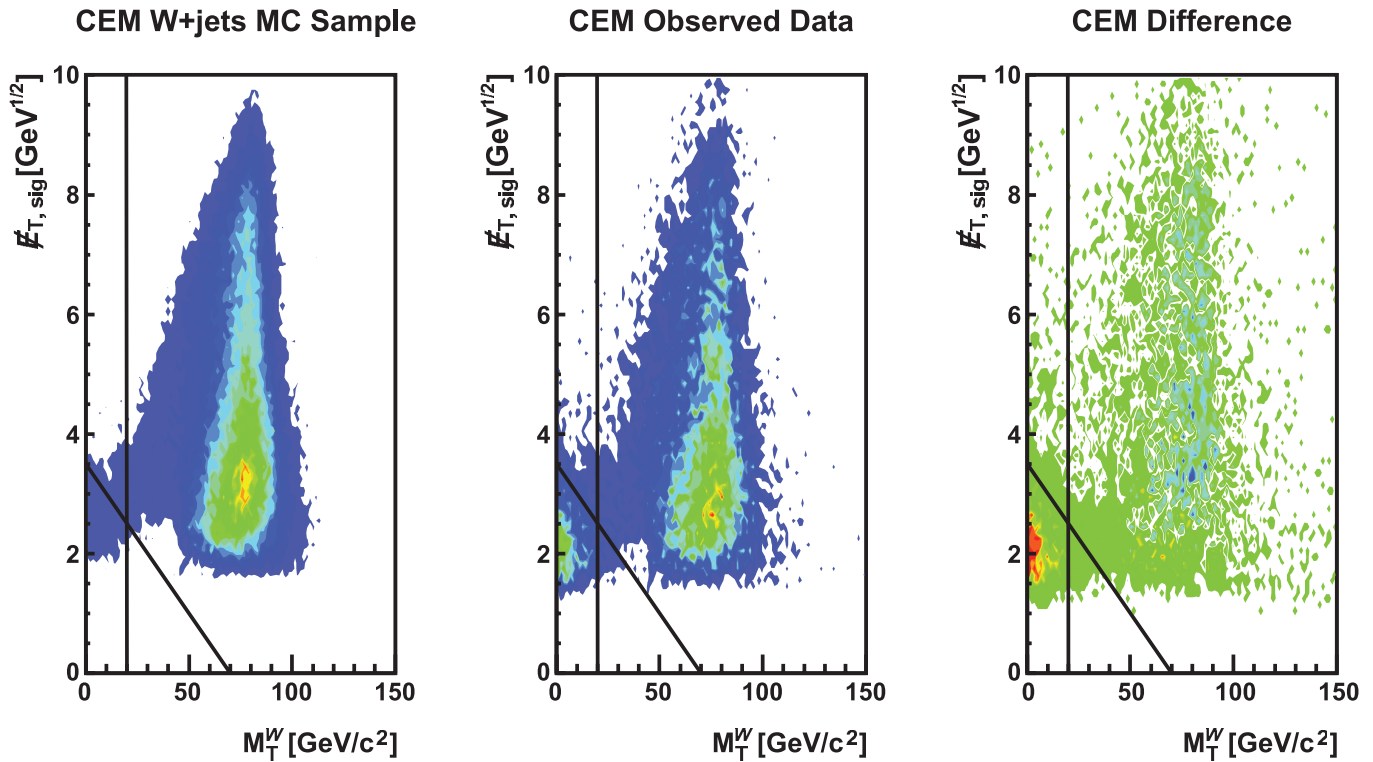
FIG. 5 (color online).   Plots of $\not{E}_{\mathrm{T,sig}}$ vs M_{T}^{W} for W + jets Monte Carlo, the selected data in the $\ell + \not{E}_{\mathrm{T}} + 2$ jet sample, and the two distributions subtracted for all CEM candidates. The black lines indicate the requirements which are applied. Events with lower $\not{E}_{\mathrm{T,sig}}$ or M_{T}^{W} are not selected.

A. s-channel single top quark model

The matrix element generator MADEVENT [50] is used to produce simulated events for the signal samples. The generator is interfaced to the CTEQ5L [51] parametrization of the parton distribution functions (PDFs). The PYTHIA [52,53] program is used to perform the parton shower and hadronization. Although MADEVENT uses only a leading-order matrix element calculation, studies [10,54] indicate that the kinematic distributions of s-channel events are only negligibly affected by NLO corrections. The parton shower simulates the higher-order effects of gluon radiation and the splitting of gluons into quarks, and the Monte Carlo samples include contributions from initial-state sea quarks via the proton PDFs.

B. t-channel single top quark model

The t-channel process is more complicated. Several authors point out [10,55–57] that the leading-order contribution to t-channel single top quark production as modeled in parton-shower Monte Carlo programs does not adequately represent the expected distributions of observable jets, which are better predicted by NLO calculations.

The leading-order process is a $2 \rightarrow 2$ process with a b quark in the initial state: $b + u \rightarrow d + t$, as shown in Fig. 6(a). For antitop quark production, the charge conjugate processes are implied. A parton distribution function for the initial-state b quark is used for the calculation.

Since flavor is conserved in the strong interaction, a $\bar{b}$ quark must be present in the event as well. In what follows, this $\bar{b}$ quark is called the spectator b quark. Leading-order parton-shower programs create the spectator b quark through backward evolution following the DGLAP scheme [58–60]. Only the low-p_{T} portion of the transverse momentum distribution of the spectator b quark is modeled well, while the high-p_{T} tail is not estimated adequately [10]. In addition, the pseudorapidity distribution of the spectator b quark, as simulated by the leading-order process, is biased towards higher pseudorapidities than predicted by NLO theoretical calculations.

We improve the modeling of the t-channel single top quark process by using two samples: one for the leading $2 \rightarrow 2$ process $b + q \rightarrow q' + t$, and a second one for the
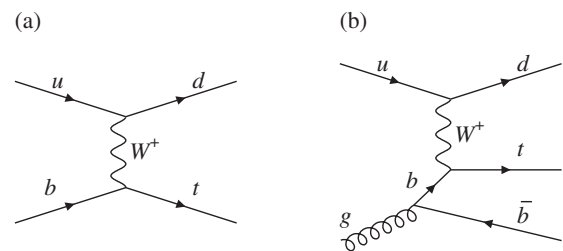
FIG. 6.   The two different t-channel processes considered in our signal model: (a) the $2 \rightarrow 2$ process and (b) the $2 \rightarrow 3$ process.

$2 \rightarrow 3$ process in which an initial-state gluon splits into $b\bar{b}$, $g + q \rightarrow q' + t + \bar{b}$. In the second process the spectator b quark is produced directly in the hard scattering described by the matrix element [Fig. 6(b)]. This sample describes the most important NLO contribution to t-channel production and is therefore suitable to describe the high-p_T tail of the spectator b quark p_T distribution. This sample, however, does not adequately describe the low-p_T portion of the spectrum of the spectator b quark. In order to construct a Monte Carlo sample which closely follows NLO predictions, the $2 \rightarrow 2$ process and the $2 \rightarrow 3$ process must be combined.

A joint event sample was created by matching the p_T spectrum of the spectator b quark to the differential cross section predicted by the ZTOP program [10] which operates at NLO. The matched t-channel sample consists of $2 \rightarrow 2$ events for spectator b quark transverse momenta below a cutoff, called K_T, and of $2 \rightarrow 3$ events for transverse momenta above K_T. The rates of $2 \rightarrow 2$ and $2 \rightarrow 3$ Monte Carlo events are adjusted to ensure the continuity of the spectator b quark p_T spectrum at K_T. The value of K_T is adjusted until the prediction of the fraction of t-channel signal events with a detectable spectator b quark jet—with $p_T > 20$ GeV/c and $|\eta| < 2.8$—matches the prediction by ZTOP. We obtain $K_T = 20$ GeV/c. All detectable spectator b quarks with $p_T > 20$ GeV/c of the joint t-channel sample are simulated using the $2 \rightarrow 3$ sample.

Figure 7 illustrates the matching procedure and compares the outcome with the differential p_T and $Q_\ell \cdot \eta$ cross sections of the spectator b quark, where Q_ℓ is the charge of the lepton from W boson decay. Both the falling p_T spectrum of the spectator b quark and the slightly asymmetric shape of the $Q_\ell \cdot \eta$ distribution are well modeled by the matched MADEVENT sample. Figure 7(a) shows the p_T distribution of the spectator b quark on a logarithmic scale. The combined sample of t-channel events has a much harder p_T spectrum of spectator b quarks than the $2 \rightarrow 2$ sample alone provides. The tail of the distribution extends beyond 100 GeV/c, while the $2 \rightarrow 2$ sample predicts very few spectator b quarks with p_T above 50 GeV/c.

C. Validation

It is important to evaluate quantitatively the modeling of single top quark events. We compare the kinematic distributions of the primary partons obtained from the s-channel and the matched t-channel MADEVENT samples to theoretical differential cross sections calculated with ZTOP [10]. We find, in general, very good agreement. For the t-channel process, in particular, the pseudorapidity distributions of the spectator b quark in the two predictions are nearly identical, even though that variable was not used to match the two t-channel samples.

One can quantify the remaining differences between the Monte Carlo simulation and the theoretical calculation by
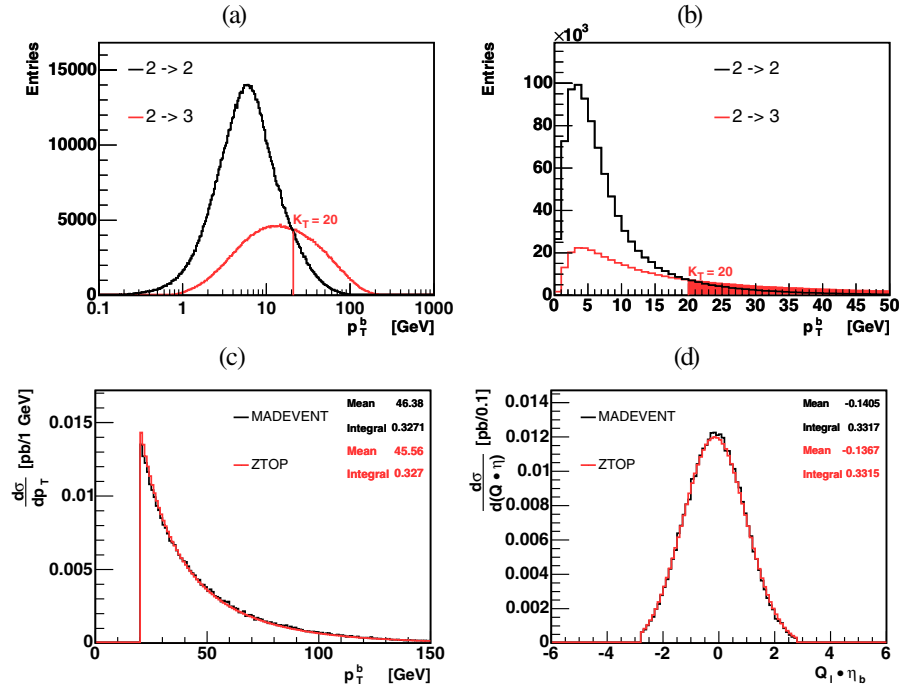
FIG. 7 (color online).   Matching of t-channel single top quark events of the $2 \rightarrow 2$ and the $2 \rightarrow 3$ processes. The p_T distributions of the spectator b quark are shown, (a) on a logarithmic p_T scale, and (b) on a linear p_T scale. The ratio of $2 \rightarrow 2$ to $2 \rightarrow 3$ events is adjusted such that the rate of spectator b quarks with $p_T > 20$ GeV/c and $|\eta| < 2.8$ matches the theoretical prediction. The fraction of these events is illustrated in (b) by the shaded area. The matched MADEVENT sample reproduces both the rate and the shape of the differential ZTOP (c) p_T and (d) $Q_\ell \cdot \eta$ cross-section distributions of the spectator b quark.

assigning weights to simulated events. The weight is derived from a comparison of six kinematic distributions: the p_T and the η of the top quark and of the two highest-E_T jets which do not originate from the top quark decay. In case of t-channel production, we distinguish between b-quark jets and light-quark jets. The correlation between the different variables, parametrized by the covariance matrix, is determined from the simulated events generated by MADEVENT. We apply the single top quark event selection to the Monte Carlo events and add the weights. This provides an estimate of the deviation of the acceptance in the simulation compared to the NLO prediction. In the $W +$ 2 jet sample we find a fractional discrepancy of $(-1.8 \pm 0.9)\%$ (MC stat.) for the t-channel, implying that the Monte Carlo estimate of the acceptance is a little higher than the NLO prediction. In the s-channel we find excellent agreement: $-0.3\% \pm 0.7\%$ (MC stat.). More details on the t-channel matching procedure and the comparison to ZTOP can be found in Refs. [61,62]. The general conclusion from our studies is that the MADEVENT Monte Carlo events represent faithfully the NLO single top quark production predictions. The matching procedure for the t-channel sample takes the main NLO effects into account. The remaining difference is covered by a systematic uncertainty of $\pm 1\%$ or $\pm 2\%$ on the acceptance for s- and t-channel events, respectively.

Recently, an even higher-order calculation of the t-channel production cross section and kinematic distributions has been performed [56,57], treating the $2 \rightarrow 3$ process itself at NLO. The production cross section in this calculation remains unchanged, but a larger fraction of events have a high-p_T spectator b within the detector acceptance. This calculation became available after the analyses described in this paper were completed. The net effect is to slightly decrease the predicted t-channel signal rate in the dominant sample with two jets and one b tag, and to significantly raise the comparatively low signal prediction in the double-tagged samples and the three-jet samples, compensating each other. Thus, the expected as well as the observed change of the outcome is insignificant for the combined and the separate extraction of the signal cross section and significance.

D. Expected signal yields

The number of expected events is given by

$$\hat{\nu} = \sigma \cdot \varepsilon_{\text{evt}} \cdot \mathcal{L}_{\text{int}}, \qquad (5)$$

where σ is the theoretically predicted cross section of the respective process, ε_{evt} is the event detection efficiency, and $\mathcal{L}_{\text{int}}$ is the integrated luminosity. The predicted cross sections for t-channel and s-channel single top quark production are quoted in Sec. I. The integrated luminosity used for the analyses presented in this article is $\mathcal{L}_{\text{int}} = 3.2 \text{ fb}^{-1}$.

The event detection efficiency is estimated by performing the event selection on the samples of simulated events. Control samples in the data are used to calibrate the efficiencies of the trigger, the lepton identification, and the b tagging. These calibrations are then applied to the Monte Carlo samples we use.

We do not use a simulation of the trigger efficiency in the Monte Carlo samples; instead we calibrate the trigger efficiency using data collected with alternate trigger paths and also $Z \rightarrow \ell^+ \ell^-$ events in which one lepton triggers the event and the other lepton is used to calculate the fraction of the time it, too, triggers the event. We use these data samples to calculate the efficiency of the trigger for charged leptons as a function of the lepton's E_T and η. The uncorrected Monte Carlo based efficiency prediction, ε_{MC} is reduced by the trigger efficiency $\varepsilon_{\text{trig}}$. The efficiency of the selection requirements imposed to identify charged leptons is estimated with data samples with high-p_T triggered leptons. We seek in these events oppositely signed tracks forming the Z mass with the triggered lepton. The fraction of these tracks passing the lepton selection requirements gives the lepton identification efficiency. The Z vetoes in the single top quark candidate selection requirements enforce the orthogonality of our signal samples and these control samples we use to estimate the trigger and identification efficiencies.

A similar strategy is adopted for using the data to calibrate the b-tag efficiency. At LEP, for example, single- and double-b-tagged events were used [63] to extract the b-tag efficiency and the b-quark fraction in Z decay. Jet formation in $p\bar{p}$ collisions involves many more processes, however, and the precise rates are poorly predicted. A jet originating from a b quark produced in a hard scattering process, for example, may recoil against another b jet, or it may recoil against a gluon jet. The invariant mass requirement used in the lepton identification procedure to purify a sample of Z decays is not useful for separating a sample of $Z \rightarrow b\bar{b}$ decays because of the low signal-to-background ratio [64].

We surmount these challenges and calibrate the b-tag efficiency in the data using the method described in Ref. [31], and which is briefly summarized here. We select dijet events in which one jet is tagged with the SECVTX algorithm, and the other jet has an identified electron candidate with a large transverse momentum with respect to the jet axis in it, to take advantage of the characteristic semileptonic decays of B hadrons. The purity of $b\bar{b}$ events in this sample is nearly unity. We determine the flavor fractions in the jets containing electron candidates by fitting the distribution of the invariant mass of the reconstructed displaced vertices to templates for b jets, charm jets, and light-flavor jets, in order to account for the presence of non-b contamination.

The fraction of jets with electrons in them passing the SECVTX tag is used to calibrate the SECVTX tagging effi-

ciency of b jets which contain electrons. This efficiency is compared with that of b jets passing the same selection requirements in the Monte Carlo, and the ratio of the efficiencies is applied to the Monte Carlo efficiency for all b jets. Systematic uncertainites to cover differences in Monte Carlo mismodeling of semileptonic and inclusive B hadron jets are assessed. The b-tagging efficiency is approximately 45% per b jet from top quark decay, for b jets with at least two tracks and which have $|\eta| < 1$. The ratio between the data-derived efficiency and the Monte Carlo prediction does not show a noticeable dependence on the $|\eta|$ of the jet or the jet's E_T.

The differences in the lepton identification efficiency and the b tagging between the data and the simulation are accounted for by a correction factor ε_{corr} on the single top quark event detection efficiency. Separate correction factors are applied to the single b-tagged events and the double b-tagged events. Systematic uncertainties are assessed on the signal acceptance due to the uncertainties on these correction factors.

The samples of simulated events are produced such that the W boson emerging from top quark decay is only allowed to decay into leptons, that is $e\nu_e$, $\mu\nu_\mu$, and $\tau\nu_\tau$. Tau lepton decay is simulated with TAUOLA [65]. The value

TABLE I. Summary of the predicted numbers of signal and background events with exactly one b tag, with systematic uncertainties on the cross section and Monte Carlo efficiencies included. The total numbers of observed events passing the event selections are also shown. The $W + 2$ jet and $W + 3$ jet samples are used to test for the signal, while the $W + 1$ jet and $W + 4$ jet samples are used to check the background modeling.

	$W + 1$ jet	$W + 2$ jets	$W + 3$ jets	$W + 4$ jets
$Wb\bar{b}$	823.7 ± 249.6	581.1 ± 175.1	173.9 ± 52.5	44.8 ± 13.7
$Wc\bar{c}$	454.7 ± 141.7	288.5 ± 89.0	95.7 ± 29.4	27.2 ± 8.5
Wcj	709.6 ± 221.1	247.3 ± 76.2	50.8 ± 15.6	10.2 ± 3.2
Mistags	1147.8 ± 166.0	499.1 ± 69.1	150.3 ± 21.0	39.3 ± 6.2
Non-W	62.9 ± 25.2	88.4 ± 35.4	35.4 ± 14.1	7.6 ± 3.0
$t\bar{t}$ production	17.9 ± 2.6	167.6 ± 24.0	377.3 ± 54.8	387.4 ± 54.8
Diboson	29.0 ± 3.0	83.3 ± 8.5	28.1 ± 2.9	7.1 ± 0.7
$Z/\gamma^* +$ jets	38.6 ± 6.3	34.8 ± 5.3	14.6 ± 2.2	4.0 ± 0.6
Total Background	3284.1 ± 633.8	1989.9 ± 349.6	926.0 ± 113.4	527.7 ± 60.3
s-channel	10.7 ± 1.6	45.3 ± 6.4	14.7 ± 2.1	3.3 ± 0.5
t-channel	24.9 ± 3.7	85.3 ± 12.6	22.7 ± 3.3	4.4 ± 0.6
Total Prediction	3319.7 ± 633.8	2120.4 ± 350.1	963.4 ± 113.5	535.4 ± 60.3
Observation	3516	2090	920	567

TABLE II. Summary of predicted numbers of signal and background events with two or more b tags, with systematic uncertainties on the cross-section and Monte Carlo efficiencies included. The total numbers of observed events passing the event selections are also shown. The $W + 2$ jet and $W + 3$ jet samples are used to test for the signal, while the $W + 4$ jet sample are used to check the background modeling.

	$W + 2$ jet	$W + 3$ jet	$W + 4$ jet
$Wb\bar{b}$	75.9 ± 23.6	27.4 ± 8.5	8.2 ± 2.6
$Wc\bar{c}$	3.7 ± 1.2	2.4 ± 0.8	1.1 ± 0.4
Wcj	3.2 ± 1.0	1.3 ± 0.4	0.4 ± 0.1
Mistags	2.2 ± 0.6	1.6 ± 0.4	0.7 ± 0.2
Non-W	2.3 ± 0.9	0.2 ± 0.1	2.4 ± 1.0
$t\bar{t}$ production	36.4 ± 6.0	104.7 ± 17.3	136.0 ± 22.4
Diboson	5.0 ± 0.6	2.0 ± 0.3	0.6 ± 0.1
$Z/\gamma^* +$ jets	1.7 ± 0.3	1.0 ± 0.2	0.3 ± 0.1
Total Background	130.4 ± 26.8	140.6 ± 19.7	149.8 ± 22.5
s-channel	12.8 ± 2.1	4.5 ± 0.7	1.0 ± 0.2
t-channel	2.4 ± 0.4	3.5 ± 0.6	1.1 ± 0.2
Total Prediction	145.6 ± 26.9	148.6 ± 19.7	151.9 ± 22.5
Observation	139	166	154

of ε_{MC}, the fraction of all signal MC events passing our event selection requirements, is multiplied by the branching fraction of W bosons into leptons, $\varepsilon_{BR} = 0.324$. The selection efficiencies for events in which the W boson decays to electrons and muons are similar, but the selection efficiency for $W \rightarrow \tau \nu_\tau$ decays is less, because many tau decays do not contain leptons, and also because the p_T spectrum of tau decay products is softer than those of electrons and muons. In total, the event detection efficiency is given by

$$\varepsilon_{evt} = \varepsilon_{MC} \cdot \varepsilon_{BR} \cdot \varepsilon_{corr} \cdot \varepsilon_{trig}. \qquad (6)$$

Including all trigger and identification efficiencies we find $\varepsilon_{evt}(t\text{-channel}) = (1.2 \pm 0.1)\%$ and $\varepsilon_{evt}(s\text{-channel}) = (1.8 \pm 0.1)\%$. The predicted signal yields for the selected two- and three-jet events with one and two (or more) b-tagged jets are listed in Tables I and II.

V. BACKGROUND MODEL

The final state of a single top quark event—a charged lepton, missing transverse energy from the undetected neutrino, and two or three jets with one or more B hadrons, is also the final state of the $Wb\bar{b}$ process, which has a much larger cross-section. Other processes which produce similar final states, such as $Wc\bar{c}$ and $t\bar{t}$, also mimic the single top quark signature because of misreconstruction or because of the loss of one or more components of the expected final state. A detailed understanding of the rates and of the kinematic properties of the background processes is necessary in order to accurately measure the single top quark production cross section.

The largest background process is the associated production of a leptonically decaying W boson and two or more jets. Representative Feynman diagrams are shown in Fig. 8. The cross section for W + jets production is much larger than that of the single top quark signal, and the W + jets production cross sections are difficult to calculate theoretically. Furthermore, W + jets events can be kinematically quite similar to the signal events we seek, and in the case that the jets contain b quarks, the final state can be identical to that of single top quark production. The narrow top quark width, the lack of resonant structure in W + jets events, and color suppression make the quantum-

FIG. 9. Feynman diagrams of the $t\bar{t}$ background to single top quark production. To pass the event selection, these events must have (a) one charged lepton , or (b) one or two hadronic jets, that go undetected.
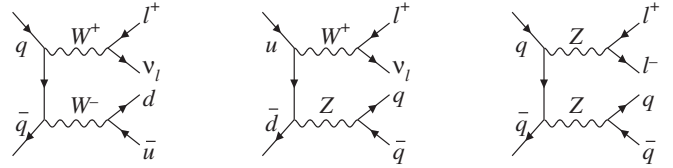
FIG. 10. Feynman diagrams for diboson production, which provides a small background for single top quark production.

mechanical interference between the signal and the background very small.

Top quark pair production, in which one or two jets, or one charged lepton, has been lost, also constitutes an important background process (Fig. 9). There are also contributions from the diboson production processes WW, WZ, and ZZ, which are shown in Fig. 10, Z/γ^* + jets processes in which one charged lepton from Z boson decay is missed, [Fig. 11(a)], and QCD multijet events, which do not contain W bosons but instead have a fake lepton and mismeasured $\not{E}_T$ [Fig. 11(b)]. The rates and kinematic properties of these processes must be carefully modeled and validated with data in order to make a precise measurement of single top quark production.

Because there are many different background processes, we use a variety of methods to predict the background rates. Some are purely based on Monte Carlo simulations scaled to high-order predictions of the cross section (such
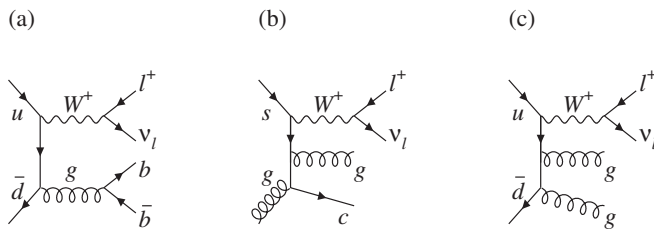

FIG. 8. Some representative diagrams of W + jets production. The production cross sections of these processes are much larger than that of single top quark production.
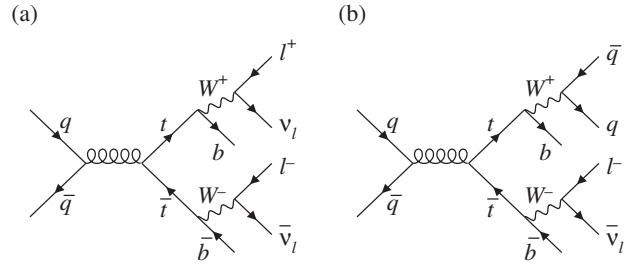

FIG. 11. Representative Feynman diagrams for (a) Z/γ^* + jets production and (b) non-W events, in which a jet has to be misidentified as a lepton and $\not{E}_T$ must be mismeasured to pass the event selection.

as $t\bar{t}$); some are purely data-based (non-W); and some require a combination of Monte Carlo and data (W + jets).

A. Monte Carlo based background processes

We use samples of simulated Monte Carlo events to estimate the contributions of $t\bar{t}$, diboson, and Z/γ^{*} + jets production to the b-tagged lepton + jets sample. The corresponding event detection efficiencies $\varepsilon_{\mathrm{evt}}$ are calculated in the same way as the single top quark processes described in Sec. IV and Eq. (6). We apply Eq. (5) to calculate the final number of expected events. Therefore, it is essential that the given physical process is theoretically well understood, i.e., the kinematics are well described in simulated events and the cross section is well known.

To model the $t\bar{t}$ production contribution to our selected samples, we use PYTHIA [53] Monte Carlo samples, scaled to the NLO theoretical cross-section prediction [66,67] of $\sigma_{t\bar{t}} = (6.70 \pm 0.83)$ pb, assuming $m_t = 175$ GeV/c^2. The systematic uncertainty contains a component which covers the differences between the calculation chosen and others [19,68]. The event selection efficiencies and the kinematic distributions of $t\bar{t}$ events are predicted using these PYTHIA samples. Because the Monte Carlo efficiencies for lepton identification and b tagging differ from those observed in the data, the $t\bar{t}$ efficiencies estimated from the Monte Carlo are adjusted by factors ϵ_{corr}, which are functions of the numbers of leptonically decaying W bosons and b-tagged jets.

To estimate the expected number of diboson events in our selected data sample we use the theoretical cross section predicted for a center-of-mass energy of $\sqrt{s} = 2.00$ TeV using the MCFM program [69] and extrapolate the values to $\sqrt{s} = 1.96$ TeV. This leads to $\sigma_{WW} = (13.30 \pm 0.80)$ pb, $\sigma_{WZ} = (3.96 \pm 0.34)$ pb, and $\sigma_{ZZ} = (1.57 \pm 0.21)$ pb. The cross-section uncertainties reported in [69] are smaller than those obtained with MCFM Version 5.4; we quote here the larger uncertainties. The event selection efficiencies and the kinematic distributions of diboson events are e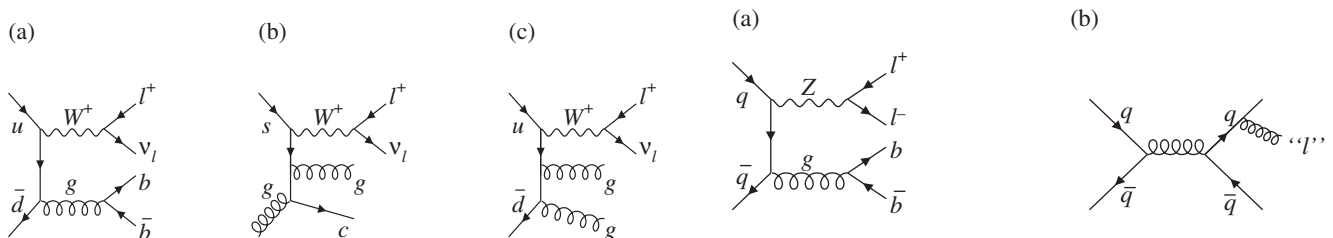stimated with PYTHIA Monte Carlo samples, with corrections applied to bring the lepton identification and b-tagging efficiency in line with those estimated from data samples.

Events with Z/γ^{*} boson production in association with jets are simulated using ALPGEN [70], with PYTHIA used to model the parton shower and hadronization. The Z/γ^{*} + jets cross section is normalized to that measured by CDF in the $Z/\gamma^{*}(\rightarrow e^{+}e^{-})$ + jets sample [71], within the kinematic range of the measurement, separately for the different numbers of jets. Lepton universality is assumed in Z decay.

B. Non-W multijet events

Estimating the non-W multijet contribution to the sample is challenging because of the difficulty of simulating these events. A variety of QCD processes produce copious amounts of multijet events, but only a tiny fraction of these events pass our selection requirements. In order for an event lacking a leptonic W boson decay to be selected, it must have a fake lepton or a real lepton from a heavy-flavor quark decay. In the same event, the $\not{E}_{\mathrm{T}}$ must be mismeasured. The rate at which fake leptons are reconstructed and the amount of mismeasured $\not{E}_{\mathrm{T}}$ are difficult to model reliably in Monte Carlo.

The non-W background is modeled by selecting data samples which have less stringent selection requirements than the signal sample. These samples, which are described below, are dominated by non-W events with similar kinematic distributions as the non-W contribution to the signal sample. The normalization of the non-W prediction is separately determined by fitting templates of the $\not{E}_{\mathrm{T}}$ distribution to the data sample.

We use three different data samples to model the non-W multijet contributions. One sample is based on the principle that non-W events must have a jet which passes all lepton identification requirements. A data sample of inclusive jets is subjected to all of our event selection requirements except the lepton identification requirements. In lieu of an identified lepton, a jet is required with $E_{\mathrm{T}} > 20$ GeV. This jet must contain at least four tracks in order to reduce contamination from real electrons from W and Z boson decay, and 80–95% of the jet's total calorimetric energy must be in the electromagnetic calorimeter, in order to simulate a misidentified electron. The b-tagging requirement on other jets in the event is relaxed to requiring a taggable jet instead of a tagged jet in order to increase the size of the selected sample. A taggable jet is one that is within the acceptance of the silicon tracking detector and which has at least two tracks in it. This sample is called the jet-based sample.

The second sample takes advantage of the fact that fake leptons from non-W events have difficulty passing the lepton selection requirements. We look at lepton candidates in the central electron trigger that fail at least two of five identification requirements that do not depend on the kinematic properties of the event, such as the fraction of energy in the hadronic calorimeter. These objects are treated as leptons and all other selection requirements are applied. This sample has the advantage of having the same kinematic properties as the central electron sample. This sample is called the ID-based sample.

The two samples described above are designed to model events with misidentified electron candidates. Because of the similarities in the kinematic properties of the ID-based and the jet-based events, we use the union of the jet-based and ID-based samples as our non-W model for triggered central electrons (the CEM sample). Remarkably, the same samples also simulate the kinematics of events with misidentified triggered muon candidates; we use the samples again to model those events (the CMUP and CMX samples). The jet-based sample alone is used to model

the non-W background in the PHX sample because the angular coverage is greater.

The kinematic distributions of the reconstructed objects in the EMC sample are different from those in the CEM, PHX, CMUP, and CMX samples due to the trigger requirements, and thus a separate sample must be used to model the non-W background in the EMC data. This third sample consists of events that are collected with the $\not{E}_T$ + jets trigger path and which have a muon candidate passing all selection requirements except for the isolation requirement. It is called the nonisolated sample.

The non-W background must be determined not only for the data sample passing the event selection requirements, but also for the control samples which are used to determine the W + jets backgrounds, as described in Secs. V C and V D. The expected numbers of non-W events are estimated in pretag events—events in which all selection criteria are applied except the secondary vertex tag requirement. We require that at least one jet in a pretagged event is taggable. In order to estimate the non-W rates in this sample, we also remove the $\not{E}_T$ event selection requirement, but we retain all other non-W rejection requirements. We fit templates of the $\not{E}_T$ distributions of the W + jets and

the non-W samples to the $\not{E}_T$ spectra of the pretag data, holding constant the normalizations of the additional templates needed to model the small diboson, $t\bar{t}$, Z + jets, and single top backgrounds. The fractions of non-W events are then calculated in the sample with $\not{E}_T > 25$ GeV. The inclusion or omission of the single top contribution to these fits has a negligible impact on the non-W fractions that are fit. These fits are performed separately for each lepton category (CEM, PHX, CMUP, CMX, and EMC) because the instrumental fake lepton fractions are different for electrons and muons, and for the different detector components. In all lepton categories except PHX, the full $\not{E}_T$ spectrum is used in the fit. For the PHX electron sample, we require $\not{E}_T > 15$ GeV in order to minimize sensitivity to the trigger. The fits in the pretag region are also used to estimate the W + jets contribution in the pretag region, as described in Sec. V C. As Fig. 12 shows, the resulting fits describe the data quite well.

Estimates of the non-W yields in the tagged samples used to search for the single top signal are also needed. These samples are more difficult because the non-W modeling samples are too small to apply tagging directly—only a few events pass the secondary vertex requirement.
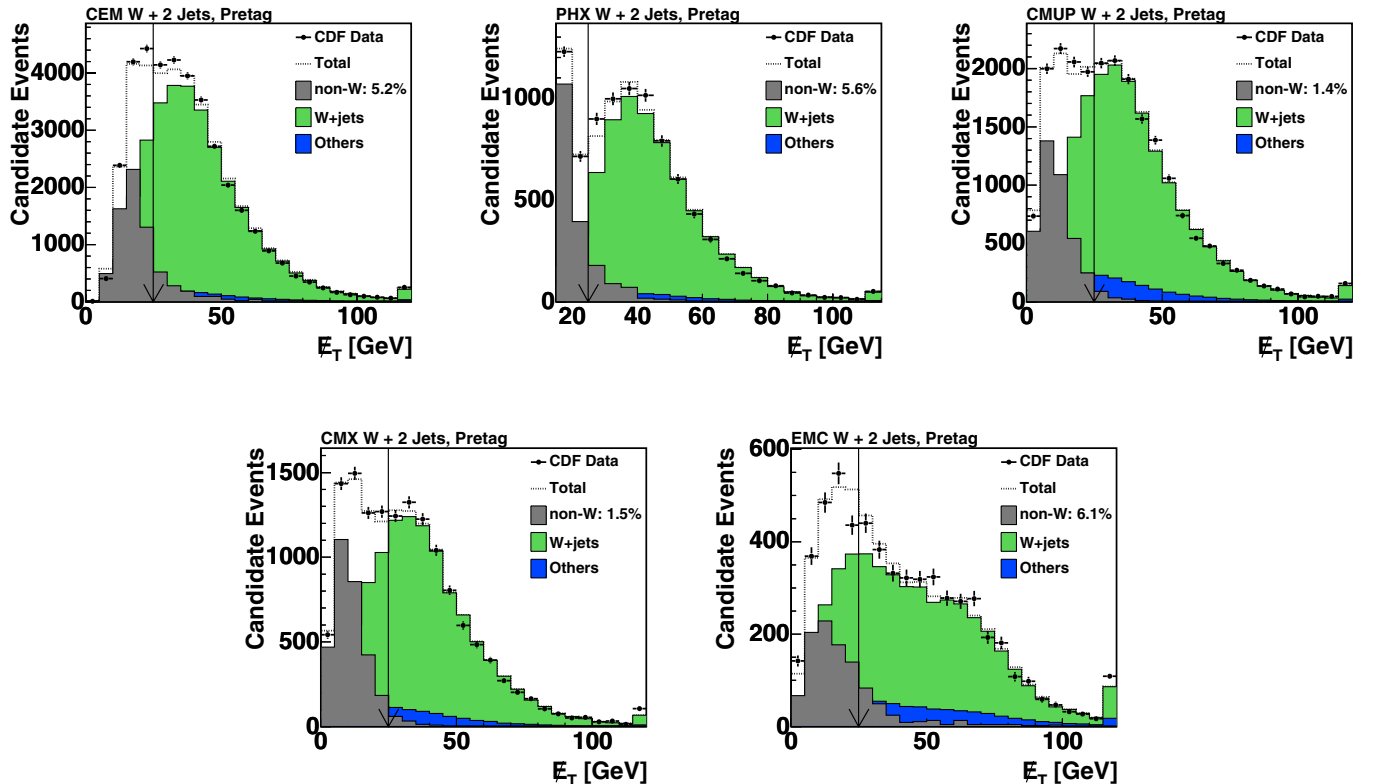
FIG. 12 (color online). Fits to $\not{E}_T$ distributions in the pretag samples for the five different lepton categories (CEM, PHX, CMUP, CMX, EMC) in W + 2 jet events. The fractions of non-W events are estimated from the portions of the templates above the $\not{E}_T$ thresholds shown by the arrows. Overflows are collected in the highest bin of each histogram. The data are indicated with points with error bars, and the shaded histograms show the best-fit predictions. The non-W templates are not shown stacked, but the W + jets and "Others" templates are stacked. The unshaded histogram is the sum of the fitted shapes.
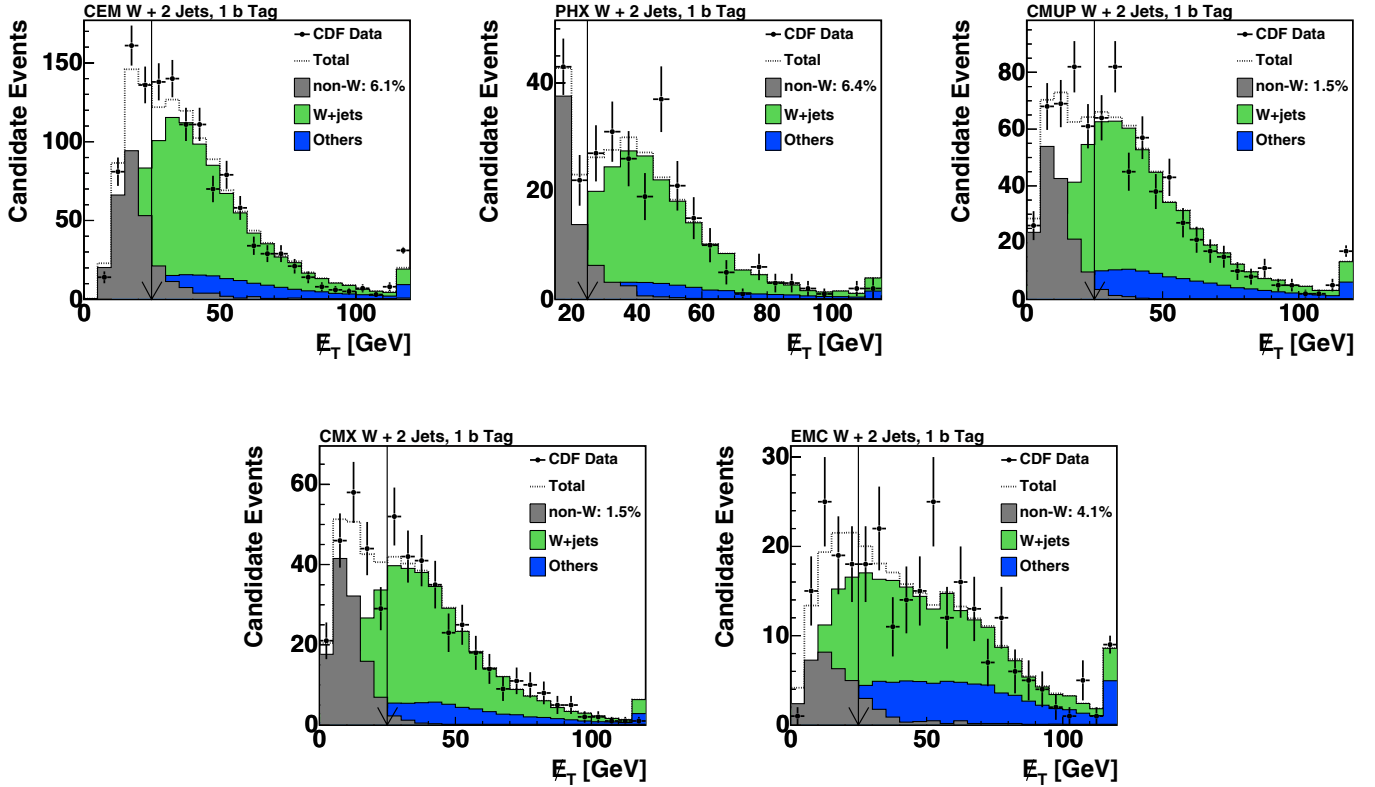
FIG. 13 (color online). Fits to $\not\!\!E_{\mathrm{T}}$ distributions in the single-tagged sample for the five different lepton categories (CEM, PHX, CMUP, CMX, EMC) in $W + 2$ jet events. The fraction of non-W events is estimated from the fraction of the template above the $\not\!\!E_{\mathrm{T}}$ threshold shown by the arrows. Overflows are collected in the highest bin of each histogram. The data are indicated with points with error bars, and the shaded histograms show the best-fit predictions. The non-W template is not shown stacked, but the $W + $ jets and Others templates are stacked. The unshaded histogram is the sum of the fitted shapes.

However, since the data show no dependence of the b-tagging rate on $\not\!\!E_{\mathrm{T}}$, we use the untagged non-W templates in the fits to the $\not\!\!E_{\mathrm{T}}$ distributions in the tagged samples. These fits are used to extract the non-W fractions in the signal samples. As before, the Monte Carlo predictions of diboson, $t\bar{t}$, $Z + $ jets, and single top production are held constant and only the normalizations of the $W + $ jets and the non-W templates are allowed to float. The resulting shapes are shown in Fig. 13 for the single-tagged sample, and these are used to derive the non-W fractions in the signal samples. As before, the inclusion or omission of the single top contributions in the fits has a negligible effect on the fitted non-W fractions. Because of the uncertainties in the tagging rates, the template shapes, and the estimation methods, the estimated non-W rates are given systematic uncertainties of $\pm 40\%$ in single-tagged events and $\pm 80\%$ in double-tagged events. These uncertainties cover the differences in the results obtained by fitting variables other than $\not\!\!E_{\mathrm{T}}$, as well as by changing the histogram binning, varying the fit range, and using alternative samples to model the non-W background. The uncertainty in the double-tagged non-W prediction is larger because of the larger statistical uncertainty arising from the smaller size of the double-tagged sample.

C. $W + $ Heavy flavor contributions

Events with a W boson accompanied by heavy-flavor production constitute the majority of the b-tagged lepton + jets sample. These processes are $Wb\bar{b}$, shown in Fig. 8(a), $Wc\bar{c}$, which is the same process as $Wb\bar{b}$, but with charm quarks replacing the b quarks, and Wcj, which is shown in Fig. 8(b). Each process may be accompanied by more jets and pass the event selection requirements for the $W + 3$ jets signal sample. Jets may fail to be detected, or they may fail to pass our selection requirements, and such events may fall into the $W + 1$ jet control sample. While these events can be simulated using the ALPGEN generator, the theory uncertainties on the cross sections of these processes remain large compared with the size of the single top quark signal [72–79]. It is because of these large *a priori* uncertainties on the background predictions and the small signal-to-background ratios in the selected data samples that we must use advanced analysis techniques to purify further the signal. We also use the data itself, both in control samples and *in situ* in the samples passing all selection requirements, to constrain the background rates, reducing their systematic uncertainties. The *in situ* fits are described in Sec. IX, and the control sample fits are described below.

The control samples used to estimate the $W +$ heavy flavor predictions and uncertainties are the pretagged $W + n$ jet samples and the tagged $W + 1$ jet sample. We use the ALPGEN + PYTHIA Monte Carlo model to extrapolate the measurements in the control samples to make predictions of the $W +$ heavy flavor background contributions in the data samples passing our signal selection requirements. The pretagged $W + n$ jet samples are used to scale the ALPGEN predictions, and the tagged $W + 1$ jet sample is used to check and adjust ALPGEN's predictions of the fractions of $W +$ jets events which are $Wb\bar{b}$, $Wc\bar{c}$, and Wcj events. A full description of the method follows.

The number of pretag $W +$ jets events is estimated by assuming that events not included in the predictions based on Monte Carlo (these are the $t\bar{t}$ and diboson predictions—the single top quark signal is a negligible component of the pretag sample) or non-W multijet events, are $W +$ jets events. That is

$$N_{W+\text{jets}}^{\text{pretag}} = N_{\text{data}}^{\text{pretag}} \times (1 - f_{\text{non-}W}^{\text{pretag}}) - N_{\text{MC}}^{\text{pretag}}, \qquad (7)$$

where $N_{\text{data}}^{\text{pretag}}$ is the number of observed events in the pretag sample, $f_{\text{non-}W}^{\text{pretag}}$ is the fraction of non-W events in the pretag sample, as determined from the fits described in Sec. V B, and $N_{\text{MC}}^{\text{pretag}}$ is the expected number of pretag $t\bar{t}$ and diboson events. ALPGEN typically underestimates the inclusive $W +$ jets rates by a factor of roughly 1.4 [80]. To estimate the yields of $Wb\bar{b}$, $Wc\bar{c}$, and Wcj events, we multiply this data-driven estimate of the $W +$ jets yield by heavy-flavor fractions.

The heavy-flavor fractions in $W +$ jets events are also not well predicted by our ALPGEN + PYTHIA model. In order to improve the modeling of these fractions, we perform fits to templates of flavor-separating variables in the b-tagged $W + 1$ jet data sample, which contains a vanishingly small component of single top quark signal events and is not otherwise used in the final signal extraction procedure. This sample is quite large and is almost entirely composed of $W +$ jets events. We include Monte Carlo models of the small contributions from $t\bar{t}$ and diboson events as separate templates, normalized to their SM expected rates, in the fits to the data. Care must be exercised in the estimation of the $W +$ heavy flavor fractions, because fitting in the $W + 1$ jet sample and using the fit values for the $W + 2$ jet and $W + 3$ jet samples is an extrapolation. We seek to estimate the b and charm fractions in these events with as many independent methods as possible and we assign generous uncertainties that cover the differences between the several estimations of the rates.

We fit the distribution of the jet-flavor separator b_{NN} described in Sec. VI. Template distributions are created based on ALPGEN + PYTHIA Monte Carlo samples for the $W + \text{LF}$, $Wc\bar{c}$, Wcj, $Wb\bar{b}$, and $Z/\gamma^* +$ jets processes, where $W + \text{LF}$ events are those in which none of the jets accompanying the leptonically decaying W boson contains

a b or c quark. The template distributions for these five processes are shown in Fig. 14(a). The $t\bar{t}$ and diboson templates are created using PYTHIA Monte Carlo samples. The non-W model described in Sec. V B is also used. The $W + \text{LF}$ template's rate is constrained by the data-derived mistag estimate, described in Sec. V D, within its uncertainty; the other $W +$ jets templates' rates are not constrained. The $t\bar{t}$, diboson, $Z/\gamma^* +$ jets, and non-W contributions are constrained within their uncertainties. The $Wb\bar{b}$ and $Wc\bar{c}$ components float in the fit but are scaled with the same scaling factor, as the same diagrams, with b and c quarks interchanged, contribute in the ALPGEN model, and we expect a similar correspondence for the leading processes in the data. We also let the Wcj fraction float in the fit. The best fit in the $W + 1$ jet sample is shown in Fig. 14(b).

The fit indicates that the ALPGEN-predicted $Wb\bar{b} + Wc\bar{c}$ fraction must be multiplied by 1.4 ± 0.4 in order for the templates to match the data, and the best-fit value of the Wcj fraction is also 1.4 ± 0.4 larger than that predicted by ALPGEN. In addition to the fit to the b_{NN} distribution, we also fit the $W +$ heavy flavor fractions in the b-tagged $W + 1$-jet sample with another variable, the reconstructed invariant mass of the secondary vertex. We perform this alternate fit in our standard b-tagged sample as well as in one with loosened b-tag requirements.

We obtain additional information from [81], in which a direct measurement of the Wc fraction is made using lepton charge correlations. The central value of this measurement agrees well with the Monte Carlo predictions. We thus set the multiplicative factor of the Wc component to 1.0 ± 0.3 for use in the two- and three-jet bins.

The 30% uncertainties assessed on the $Wb\bar{b} + Wc\bar{c}$ and Wcj yields cover the differences in the measured fit values and also approximates our uncertainty in extrapolating this fraction to $W + 2$ and 3 jet events. We check these extrapolations in the $W + 2$ and 3 jet events as shown in Figs. 14(c) and 14(d); no additional fit is performed for this comparison. The rates and flavor compositions match very well with the observed data in these samples. The uncertainties in the fit fractions arising from the uncertainties on the shapes of the b_{NN} templates discussed in Sec. VI are a negligible component of the total uncertainty.

Since the yields of $W +$ heavy flavor events are estimated from b-tagged data using the same SECVTX algorithm as is used for the candidate event selection, the uncertainty in the b-tagging efficiency does not factor into the prediction of these rates.

D. Rates of events with mistagged jets

Some $W + \text{LF}$ events pass our event selection requirements due to the presence of mistagged jets. A mistagged jet is one which does not contain a weakly-decaying B or charm hadron but nonetheless passes all of the secondary
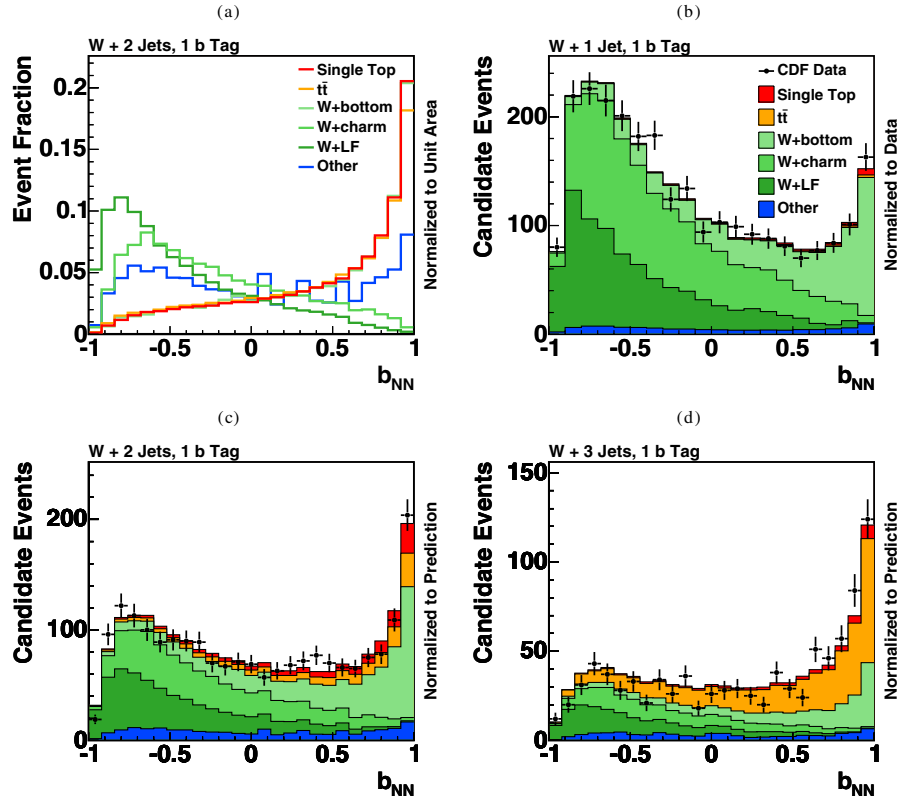
FIG. 14 (color online). Templates (a) of the jet flavor separator b_{NN} for W + light, W + charm (adding the $Wc\bar{c}$ and Wcj contributions because of their similar shapes), and W + bottom events. The template labeled "Other" represents the diboson and Z/γ^* + jets contributions. The strong discrimination b_{NN} provides to separate jet flavors makes it a powerful variable in multivariate analyses. Panel (b) shows the outcome of the fit to the W + 1 jet data sample allowing the b, c, and light-flavor components to float as described in Sec. V. Panels (c) and (d) compare the data and the corresponding predictions in the W + 2 jet and W + 3 jet samples. In panels (b) through (d), the data are indicated with points with error bars, and the model predictions are shown with shaded histograms stacked in the same order as the legend.

vertex tagging requirements of the SECVTX algorithm [31]. Jets are mistagged for several reasons: tracking errors such as hit misassignment or resolution effects cause the reconstruction of false secondary vertices, the multiprong decays of long-lived particles like the K_s^0 and the Λ^0 supply real secondary vertices, and nuclear interactions with the detector material also provide a real source of non-b/c secondary vertices.

The estimation of the background yields from tracking resolution related mistags is accomplished without the use of detector simulation. The procedure is to measure the fractions of jets which have negative decay lengths (defined below) to estimate the fraction of light-flavor jets which have incorrect positive decay lengths. This fraction is adjusted in order to account for the asymmetry between the negative decay length distribution and the positive decay length distribution, and to account for the heavy-flavor contribution in the jet data, to obtain the mistag probability. This probability is multiplied by an estimate of W + LF jet yield in each of our samples, separately for each lepton category and jet-

number category. Each of these steps is described in detail below.

Events passing inclusive jet triggers with vertices with negative two-dimensional (2D) decay lengths comprise the control sample used to estimate the mistag rate. The 2D decay length L_{xy} is the magnitude of the displacement from the primary vertex to the reconstructed secondary vertex, projected first onto the plane perpendicular to the beam axis, and then projected again onto the jet axis's projection in the plane perpendicular to the beam axis. The sign is given by the sign of the dot product of the 2D decay length and the jet momentum. Tracking resolution effects are expected to produce a symmetric distribution of the 2D decay length of light-flavor misreconstructed secondary vertices, centered on zero. A jet is said to be "negatively tagged" if the transverse decay length significance $L_{xy}/\sigma_{L_{xy}} < -7.5$, while $L_{xy}/\sigma_{L_{xy}} > 7.5$ defines a "positively tagged" jet.

The per-jet mistag rate is not a single number but rather it is parametrized as a function of six kinematic variables: the E_T and η of the jet, the number of tracks in the jet, the

scalar sum of transverse energy of the tight jets, the number of reconstructed primary vertices, and the z coordinate of the primary vertex associated with the jet. Since the negative tag rate does not fully reflect the positive mistags due to the decays of long-lived particles and interactions with the detector material, a correction factor $\alpha\beta$ for the mistag asymmetry is applied. The factor α corrects for the asymmetry between the positive and negative tag rates of light-flavor jets, and the factor β corrects for the presence of b jets in the jet samples used to derive the mistag rate. These correction factors are extracted from fits to distributions of the invariant mass of the reconstructed secondary vertex in tagged jets in an inclusive jet sample. A systematic uncertainty is derived from fits to templates of pseudo-$c\tau$, which is defined as $L_{xy}\frac{m}{p_T}$ [31], where m is the invariant mass of the tracks in the displaced vertex, and p_T is the magnitude of the vector sum of the transverse momenta of the tracks in the displaced vertex. The systematic uncertainty on the asymmetry factor $\alpha\beta$ is the largest component of the uncertainty on the mistag estimate. Another component is estimated from the differences in the negative tag rates computed with different jet data samples with varying trigger requirements. The average rate for jets to be mistagged is approximately 1%, although it depends strongly on the jet E_T.

The per-jet mistag probabilities are multiplied by data-driven estimates of the W + LF yields, although we must subtract the yields of the other components. We subtract the pretagged W + heavy flavor contributions from the pretagged W + jets yield of Eq. (7) to estimate the W + LF yield:

$$N_{W+\text{LF}}^{\text{pretag}} = N_{W+\text{jets}}^{\text{pretag}} - N_{Wb\bar{b}}^{\text{pretag}} - N_{Wc\bar{c}}^{\text{pretag}} - N_{Wcj}^{\text{pretag}}. \qquad (8)$$

The pretagged W + heavy flavor contributions are estimated by dividing the tagged W + heavy flavor contributions by the b-tagging efficiencies for each event category. The mistag parametrization is applied to each of the Monte Carlo and data samples used in Eqs. (7) and (8), in order for the total mistag yield prediction not to be biased by differences in the kinematics of the several W + jets flavor categories.

We use ALPGEN + PYTHIA Monte Carlo samples to predict the kinematics of W + LF events for use in the analyses of this paper. The mistag rate parametrization described above is applied to each jet in W + LF MC events, and these rates are used to weight the events to predict the yield of mistagged events in each bin of each histogram of each variable.

The predicted numbers of background events, signal events, and the overall expected normalizations are given in Tables I, for events with exactly one b tag, and in Table II for events with two or three b tags. Only two selected events in the data have three b tags, consistent with the expectation assuming that the third tag is a mistag. The observed event counts and predicted yields are sum-
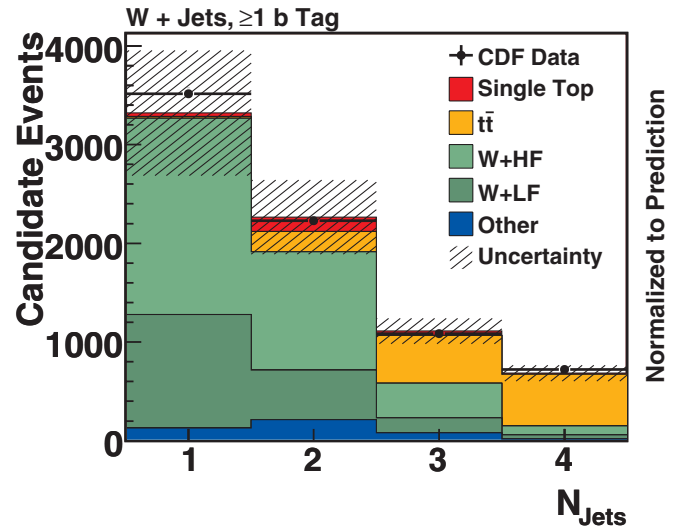
FIG. 15 (color online).   The number of events predicted and observed for W + jets events in which at least one jet is b tagged. The data are indicated with points, and the shaded histograms show the signal and background predictions, which are stacked to form the total prediction. The stacking order is the same as the legend. The systematic uncertainty on the rates is far too large to use a simple counting experiment to measure the single top quark cross section.

marized graphically as functions of jet multiplicity in Fig. 15.

E. Validation of Monte Carlo simulation

Because multivariate analyses depend so heavily on properly simulating events, it is very important to validate the modeling of the distributions in Monte Carlo by checking them with the data. We do this by comparing hundreds of data and Monte Carlo distributions. We make comparisons in control samples in which no jets have been b-tagged to test the W + LF shapes, we test the modeling of W + 1 jet events to examine W + heavy flavor fraction and shapes, we compare the data and Monte Carlo distributions of kinematic variables in the signal regions of tagged 2- and 3-jet events to check the modeling of all of these variables, and we verify the modeling of the correlations between the discriminating variables.

A sample of the validation plots we examine is shown in Figs. 16–18. The close match of the distributions gives confidence in the results. The validations of the modeling of other observable quantities are shown later in this paper.

Out of the hundreds of distributions checked for discrepancies, only two distributions in the untagged W + jets data were found to be poorly simulated by our Monte Carlo model: the pseudorapidity of the lowest-energy jet in both W + 2 jet and W + 3 jet events and the distance between the two jets in $\phi - \eta$ space in W + 2 jet events. These discrepancies are used to estimate systematic uncertainties on the shapes of our final discrimi-

FIG. 16 (color online).   Validation plots comparing data and Monte Carlo for basic kinematic quantities for events passing the event selection requirements with two jets and at least one *b* tag. The data are indicated with points, and the shaded histograms show the signal and background predictions which are stacked to form the total prediction. The stacking order follows that of the legend.
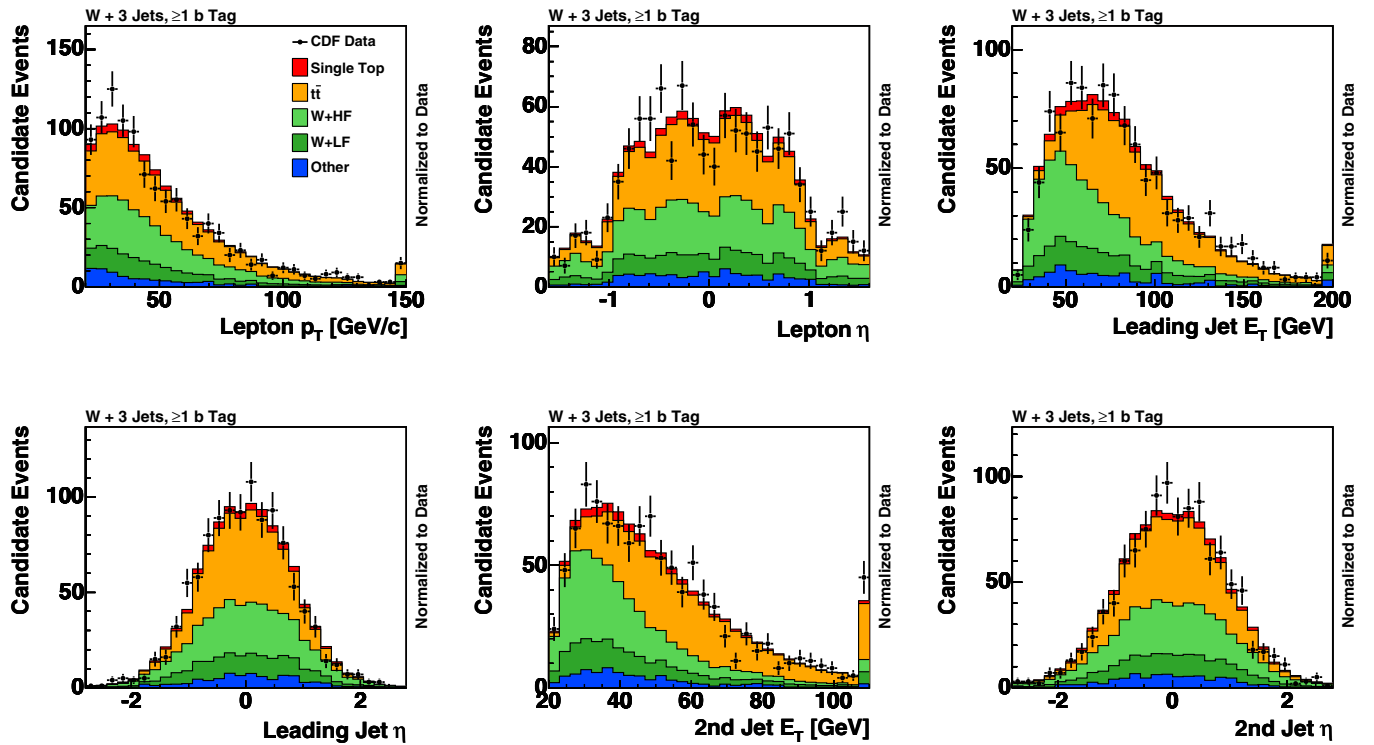
FIG. 17 (color online).   Validation plots comparing data and Monte Carlo for basic kinematic quantities for events passing the event selection requirements with three identified jets and at least one *b* tag. The data are indicated with points, and the shaded histograms show the signal and background predictions which are stacked to form the total prediction. The stacking order follows that of the legend.

FIG. 18 (color online).   Validation plots comparing data and Monte Carlo for missing transverse energy for events passing our event selection requirements with (a) two jets and (b) three jets, both with at least one b tag. The data are indicated with points, and the shaded histograms show the s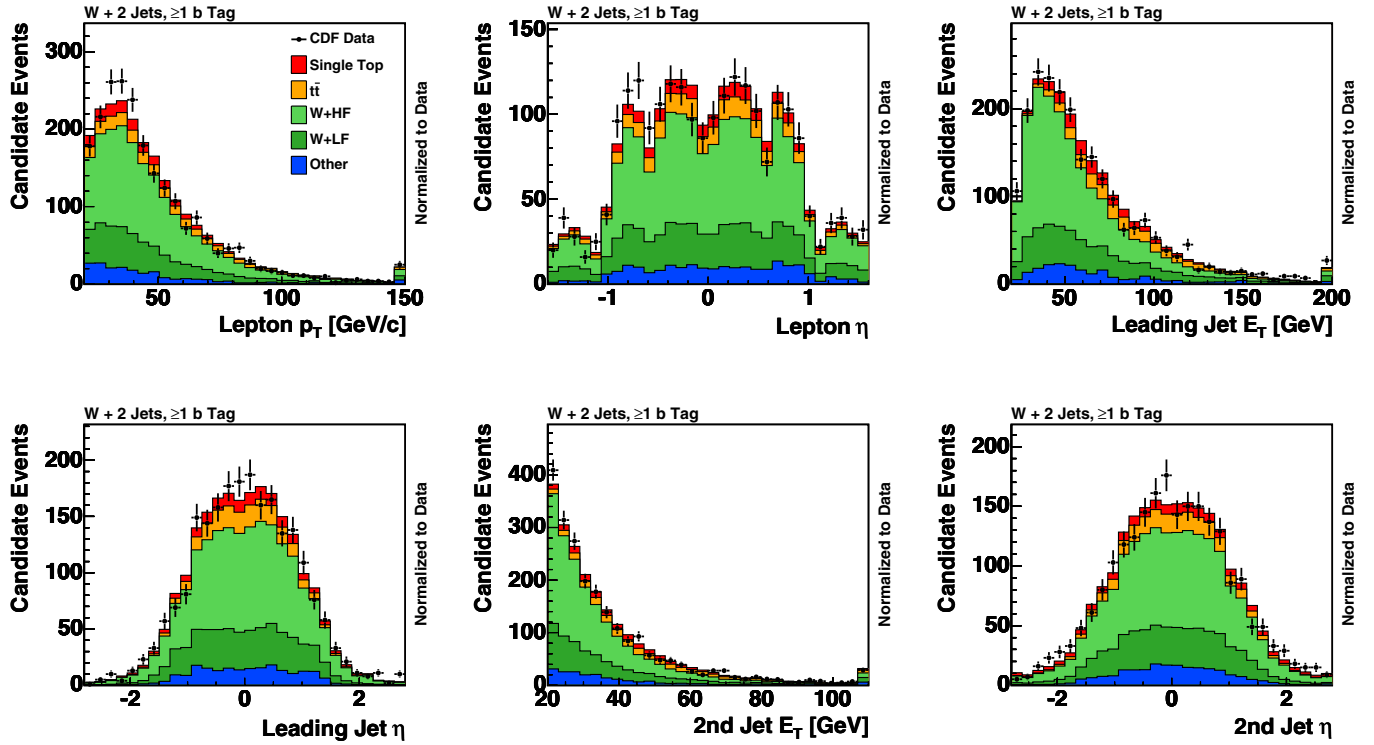ignal and background predictions which are stacked to form the total prediction. The stacking order follows that of the legend.
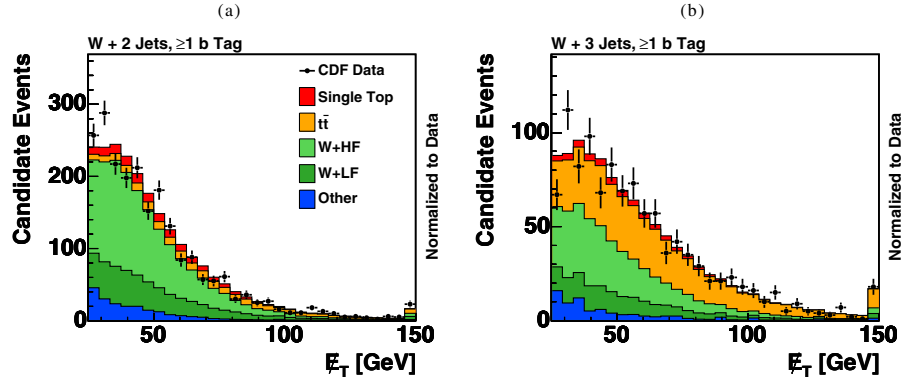
nant variables. These distributions and the discussion of associated systematic uncertainties are presented in Sec. VIII.

VI. JET FLAVOR SEPARATOR

In our event selection, we identify b-quark jets by requiring a reconstructed secondary vertex. A large fraction, 48%, of the expected background events with b-tagged jets have no B hadrons in them at all. This is due to the long lifetime and the mass of charm hadrons, the false reconstruction of secondary vertices in light jets, and the fact that the fraction of pretagged W + jets events containing B hadrons is small compared with the charm and light-flavored components. Tagged jets without B hadrons in them can be separated from those containing B hadrons by extending the vertex requirement using reconstructed quantities that differentiate the two classes of jets. These quantities take advantage of the long lifetime ($\tau \approx 1.6$ ps) and the large mass ($m \approx 5$ GeV/c^2) of B hadrons.

The invariant mass of the tracks in the reconstructed vertex is larger on average for vertices arising from a B hadron decay than it is in vertices in jets that do not contain B hadrons. The number of tracks in the secondary vertex is also on average larger, and the significance of the transverse decay length ($\Delta L_{xy}/\sigma_{xy}$) is larger for B hadron vertices.

In addition to the vertex properties, attributes of the tracks in the jet are suitable to discriminate jets containing a B hadron. Tracks of charged particles originating from the decay of a B hadron have larger impact parameters and higher transverse momenta relative to the jet axis. The presence of semileptonic B hadron decays increases the number and transverse momenta relative to the jet axis of electrons and muons in b jets as compared to non-b jets.

To make full use of all discriminating quantities and their correlations, the variables are used as inputs to a neural network which is applied to jets selected by the SECVTX secondary vertex tagger [82]. This network is trained with simulated events of single top quark production and the main background processes, mixed according to the background estimation. Processes with secondary vertices due to B hadron decays are treated as signal events, namely, single top quark, $t\bar{t}$, and $Wb\bar{b}$ production. Physical processes containing no b quarks but charm and light flavors are treated as background: $Wc\bar{c}$, Wcj, and W + light jets.

The NEUROBAYES package [83] used for the neural-network jet flavor separator combines a three-layer feed forward neural network with a complex robust preprocessing. Transforming the input variables to be distributed as unit-width Gaussians reduces the influence of long tails; diagonalization and rotation transform the covariance matrix of the variables into a unit matrix. The neural network uses Bayesian regularization techniques for the training process. The network infrastructure consists of one input node for each input variable plus one bias node, ten hidden nodes, and one output node which gives a continuous output variable b_{NN} in the interval $[-1, 1]$. Jets with secondary vertices induced by the decay of a B hadron tend to have b_{NN} values close to 1, while jets with falsely reconstructed vertices tend to have b_{NN} values near -1.

The significances of the training variables are determined automatically during the preprocessing in NEUROBAYES. The correlation matrix of all preprocessed input variables is calculated, including the correlation of all variables to the target variable, which is $+1$ for jets with B hadron decays and -1 for all other jets. The variables are omitted one at a time to determine the loss of total correlation to the target caused by their removal. The variable with the smallest loss of correlation is discarded leading to an $(n-1)$-dimensional correlation matrix. The same procedure is repeated with the reduced correlation matrix to find the least important of the $(n-1)$ remaining variables. The significance of each variable is calculated by dividing the loss of correlation induced by its removal by the square

root of the sample size. We investigated 50 candidate input variables but chose to include as inputs only those with a significance larger than 3.0, of which there are 25.

Because the neural-network jet flavor separator is trained using simulated events, it is essential to verify that the input and output distributions are modeled well, and to assess systematic uncertainties where discrepancies are seen. The shapes of the input variable distributions in the data are found to be reasonably well reproduced by the simulation. We also examine the distribution of b_{NN} for both b signal and non-b background. The b signal distribution is checked with double-SECVTX-tagged dijet events and compared against Monte Carlo jets with B hadron decays. One jet in addition is required to have an electron with a large transverse momentum with respect to the jet axis, in order to purify further the b content of the sample. The jet opposite to the electron-tagged jet is probed for its distribution of the neural-network output. The distribution of b_{NN} in these jets is well simulated by that of b jets in the Monte Carlo [82].

To test the response of the network to light-flavored jets, negative-tagged jets were tested in data and Monte Carlo. A correction function was derived [82] to adjust for the small discrepancy observed in the output shape. This correction function is parametrized in the sum of transverse energies in the event, the number of tracks per jet, and the transverse energy of the jet. The correction function is applied to light-flavored and charm Monte Carlo jets in the analyses presented in this paper, but not to b jets. The uncorrected neural-network outputs are used to evaluate systematic uncertainties on the shapes of the final discriminant distributions.

The resulting network output b_{NN} distinguishes the b signal from the charm and light-flavored background processes with a purity that increases with increasing b_{NN}, as can be seen in Fig. 14(a). Furthermore, the network gives very similar shapes for different b-quark–producing processes, indicating that it is sensitive to the properties of b-quark jets and does not depend on the underlying processes that produce them.

Not only is b_{NN} a valuable tool for separating the single top quark signal from background processes that do not contain b jets, it is also valuable for separating the different flavors of $W +$ jets events, which is crucial in estimating the background composition. As described in Sec. V, the distribution of b_{NN} is fit in b-tagged $W + 1$ jet events, and the heavy-flavor fractions for b and charm jets are extracted. Using also a direct measurement of the Wc rate [81], predictions are made of the b and charm jet fractions in the two- and three-jet bins. These predictions are used to scale the ALPGEN Monte Carlo samples, which are then compared with the data in the two- and three-jet b-tagged samples, without refitting the heavy-flavor composition, as shown in Figs. 14(c) and 14(d). The three-jet sample has a larger sample of $t\bar{t}$ events which are enriched in b jets. The

successful modeling of the changing flavor composition as a function of the number of identified jets provides confidence in the correctness of the background simulation.

All multivariate methods described here use b_{NN} as an input variable, and thus we need b_{NN} values for all Monte Carlo and data events used to model the final distributions. For the mistagged $W + $ LF shape prediction, we use the $W + $ LF Monte Carlo sample, where the events are weighted by the data-based mistag prediction for each taggable jet. This procedure improves the modeling over what would be obtained if Monte Carlo mistags were used, as the mistag probabilities are based on the data, and it increases the sample size we use for the mistag modeling. An issue that arises is that parametrized mistagged events do not have b_{NN} values and random values must be chosen for them from the distribution in light-flavor events. If a $W + $ LF event has more than one taggable jet, then random values are assigned to both jets. These events are used for both the single-mistag prediction and the double-mistag prediction with appropriate weights. The randomly chosen flavor separator values must be the same event-by-event and jet-by-jet for each of the four analyses in this paper in order for the super discriminant combination method to be consistent.

The distributions of b_{NN} for non-W multijet events are more difficult to predict because the flavor composition of the jets in these events is poorly known. Specifically, since a non-W event must have a fake lepton (or a lepton from heavy-flavor decay), and also mismeasured $\not{E}_T$, the flavor composition of events passing the selection requirements depends on the details of the detector response, particularly in the tails of distributions which are difficult to model. It is necessary therefore to constrain these flavor fractions with CDF data, and the flavor fractions thus estimated are specific to this analysis. The non-W event yields are constrained by the data as explained in Sec. V B.

The fraction of each flavor: b, charm, and light-flavored jets (originating from light quarks or gluons), is estimated by applying the jet flavor separator to b-tagged jets in the $15 < \not{E}_T < 25$ GeV sideband of the data. In this sample, we find a flavor composition of 45% b quark jets, 40% c quark jets, and 15% light-flavored jets. Each event in the non-W modeling samples (see Sec. V B) is randomly assigned a flavor according to the fraction given above and then assigned a jet flavor separator value chosen at random from the appropriate flavor distribution. The fractions of the non-W events in the signal sample are uncertain both due to the uncertainties in the sideband fit and the extrapolation to the signal sample. We take as an alternative flavor composition estimate 60% b quark jets, 30% c quark jets, and 10% light-flavored jets, which is the most b-like possibility of the errors on the flavor measurement. This alternative flavor composition affects the shapes of the final discriminant distribution through the different flavor separator neural-network values.

VII. MULTIVARIATE ANALYSIS

The search for single top quark production and the measurement of its cross section present substantial experimental challenges. Compared with the search for $t\bar{t}$ production, the search for single top quarks suffers from a lower SM production rate and a larger background. Single top quark events are also kinematically more similar to W + jets events than $t\bar{t}$ events are, since there is only one heavy top quark and thus only one W boson in the single top quark events, while there are two top quarks, each decaying to Wb, in $t\bar{t}$ events. The most serious challenge arises from the systematic uncertainty on the background prediction, which is approximately 3 times the size of the expected signal. Simply counting events which pass our selection requirements will not yield a precise measurement of the single top quark cross section no matter how much data are accumulated because the systematic uncertainty on the background is so large. In fact, in order to have sufficient sensitivity to expect to observe a signal at the 5σ level, the systematic uncertainty on the background must be less than one-fifth of the expected signal rate.

Further separation of the signal from the background is required. Events that are classified as being more signal-like are used to test for the presence of single top quark production and measure the cross section, and events that are classified as being more background-like improve our knowledge of the rates of background processes. In order to optimize our sensitivity, we construct discriminant functions based on kinematic and b-tag properties of the events, and we classify the events on a continuous spectrum that runs from very signal-like for high values of the discriminants to very background-like for low values of the discriminants. We fit the distributions of these discriminants to the background and signal + background predictions, allowing uncertain parameters, listed in Sec. VIII, to float in a manner described in Sec. IX.

To separate signal events from background events, we look for properties of the events that differ between signal and background. Events from single top quark production have distinctive energy and angular properties. The backgrounds, too, have distinctive features which can be exploited to help separate them. Many of the variables we compute for each selected candidate event are motivated by a specific interpretation of the event as a signal event or a background event. It is not necessary that all variables used in a discriminant are motivated by the same interpretation of an event, nor do we rely on the correctness of the motivation for the interpretation of any given event. Indeed, each analysis is made more optimal when it includes a mixture of variables that are based on different ways to interpret the measured particles in the events. We optimize our analyses by using variables for which the distributions are maximally different between signal events and background events, and for which we have reliable modeling as verified by the data.

We list below some of the most sensitive variables, and explain why they are sensitive in terms of the differences between the signal and background processes that they exploit. The three multivariate discriminants, likelihood functions, neural networks, and boosted decision trees, use these variables, or variations of them, as inputs; the analyses also use other variables. The matrix element analysis uses all of these features implicitly, and it uses b_{NN} explicitly. Normalized Monte Carlo predictions ("templates") and modeling comparisons of these variables are shown in Figs. 19 and 20.

(i) $M_{\ell\nu b}$: the invariant mass of the charged lepton, the neutrino, and the b jet from the top quark decay. The p_z of the neutrino, which cannot be measured, is inferred by constraining $M_{\ell\nu}$ to the W boson mass, using the measured charged lepton candidate's momentum and setting $p_{\mathrm{T}}^{\nu} = E_{\mathrm{T}}$. The neutrino's p_z is the solution of a quadratic equation, which may have two real solutions, one real solution, or two complex solutions. For the case with two real solutions, the one with the lower $|p_z|$ is chosen. For the complex case, the real part of the p_z solution is chosen. Some analyses use variations of this variable with different treatments of the unmeasured $|p_z|$ of the neutrino. The distribution of $M_{\ell\nu b}$ peaks near m_t for signal events, with broader spectra for background events from different processes.

(ii) H_{T}: the scalar sum of the transverse energies of the jets, the charged lepton, and E_{T} in the event. This quantity is much larger for $t\bar{t}$ events than for W + jets events; single top quark events populate the region in between W + jets events and $t\bar{t}$ events in this variable.

(iii) M_{jj}: the invariant dijet mass, which is substantially higher on average for events containing top quarks than it is for events with W + jets.

(iv) $Q \times \eta$: the sign of the charge of the lepton times the pseudorapidity of the light-quark jet [84]. Large $Q \times \eta$ is characteristic of t-channel single top quark events, because the light quark recoiling from the single top quark often retains much of the momentum component along the z axis it had before radiating the W boson. It, therefore, often produces a jet which is found at high $|\eta|$. Multiplying η by the sign of the lepton's charge Q improves the separation power of this variable since 2/3 of single top quark production in the t channel is initiated by a u quark in the proton or a $(\bar{u})$ quark in the antiproton, and the sign of the lepton's charge determines the sign of the top quark's charge and is correlated with the sign of the η of the recoiling light-flavored jet. The other 1/3 of single top quark production is initiated by down-type quarks and has the opposite charge-η correlation. W + jets and $t\bar{t}$ events lack this corre-

FIG. 19 (color online).   Monte Carlo templates (left) and validation plots (right) comparing data and Monte Carlo for variables with good discriminating power for events passing our selection requirements with two or three identified jets and at least one b tag. The data are indicated with points, and the shaded histograms show the signal and background predictions which are stacked to form the total prediction. The stacking order follows that of the legend. Overflows are collected in the highest bin of each histogram.

lation, and also have fewer jets passing our E_T requirement at large $|\eta|$ than the single top quark signal.

(v) $\cos\theta_{\ell j}$: the cosine of the angle between the charged lepton and the light-quark jet [20]. For t-channel events, this tends to be positive because of the $V - A$ angular dependence of the W boson vertex. This variable is most powerful when computed in the rest frame of the top quark.

(vi) b_{NN}: the jet flavor separator described in Sec. VI. This variable is a powerful tool to separate the signal from $W + \mathrm{LF}$ and $W + \mathrm{charm}$ events.

(vii) M_{T}^W: the "transverse mass" of the charged lepton candidate and the $\vec{E}_T$ vector. The transverse mass is

defined to be the invariant mass of the projections of the three-momentum components in the plane perpendicular to the beam axis, and is so defined as to be independent of the unmeasured p_z of the neutrino. Events without W bosons in them (but with fake leptons and mismeasured E_T) have lower M_{T}^W on average than $W + \mathrm{jets}$ events, signal events, and $t\bar{t}$ events. Events with two leptonically decaying W bosons—some diboson and $t\bar{t}$ events—have even higher average values of M_{T}^W. The distribution of M_{T}^W is an important cross-check of the non-W background rate and shape modeling.

While there are many distinctive properties of a single top quark signal, no single variable is sufficiently sensitive
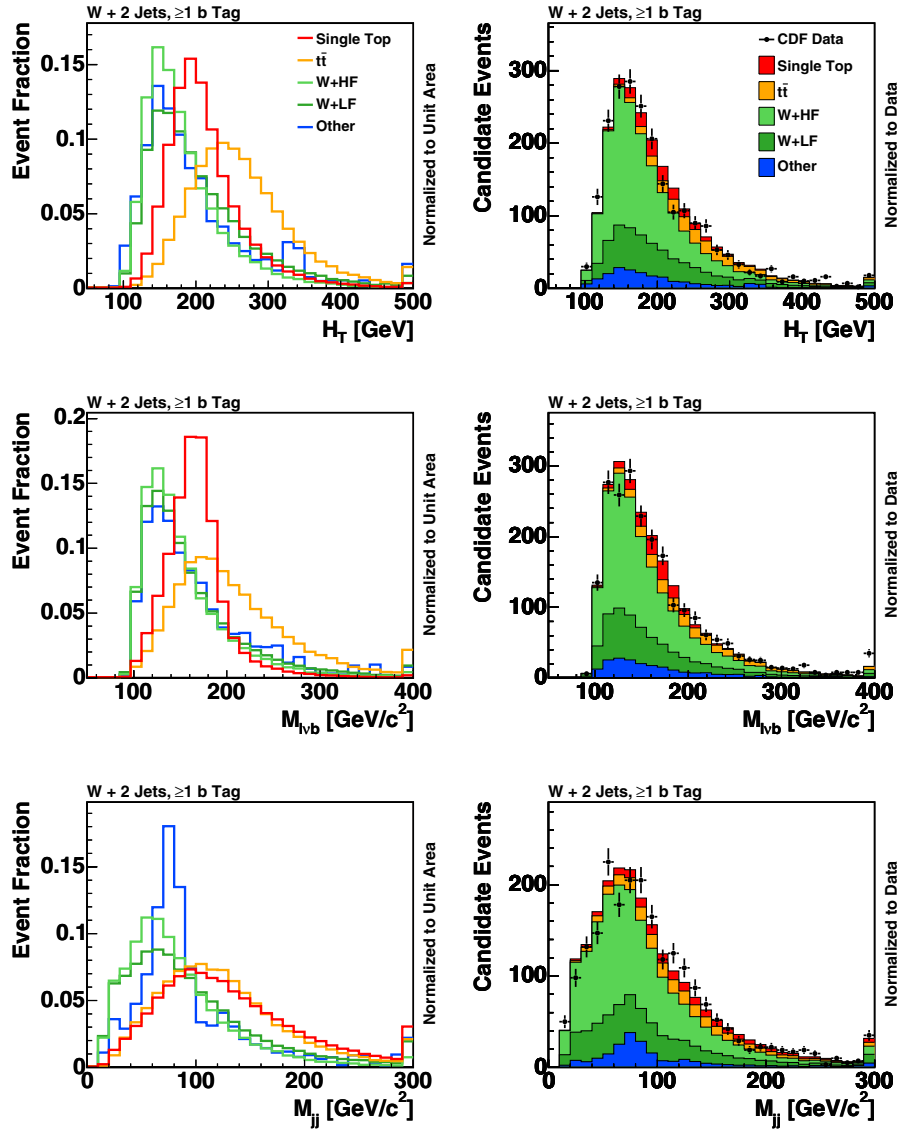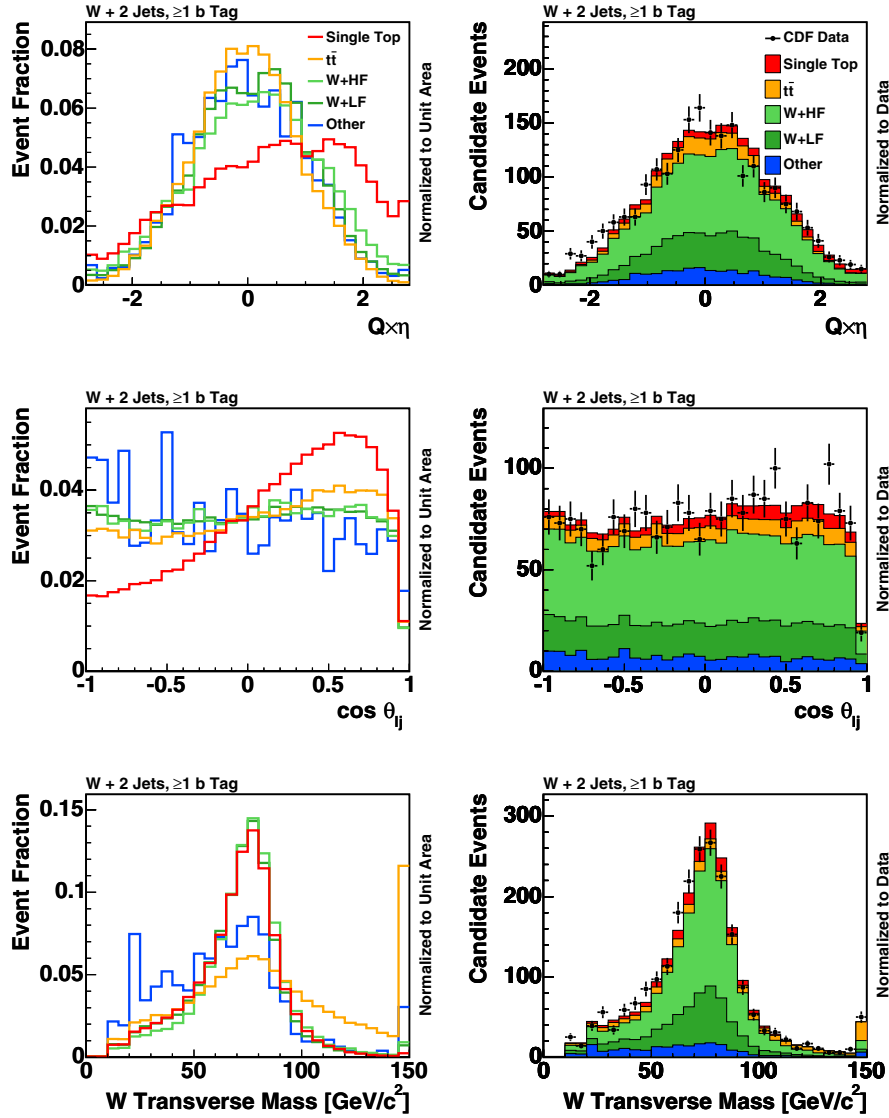
FIG. 20 (color online). Monte Carlo templates (left) and validation plots (right) comparing data and Monte Carlo for variables with good discriminating power for events passing our selection requirements with two identified jets and at least one b tag. The data are indicated with points, and the shaded histograms show the signal and background predictions which are stacked to form the total prediction. The stacking order follows that of the legend. Overflows are collected in the highest bin of each histogram.

to extract the signal with the present data sample. We must therefore use techniques that combine the discrimination power of many variables. We use four such techniques in the W + jets sample, a multivariate likelihood function, a matrix element method, an artificial neural network, and a boosted decision tree. These are described in detail in the following sections. Each of these techniques makes use of the most sensitive variables described above in different ways, and in combination with other variables. The measurements using the separate techniques are highly correlated because the same events are analyzed with each technique and because many of the same features are used, but the differences between the techniques provide more discrimination power in combination as well as

the ability to cross-check each result with the others separately.

The measured single top quark cross section and the significance of the result depend on the proper modeling of the input variable distributions for the signals and the background processes. We examine the distributions of all input variables in the selected candidate events, comparing the data to the sum of the background and SM signal predictions, and we also compare the distributions in a sample of events with no b tags but which pass all other event selection requirements. The untagged event sample is much larger than the tagged data sample and has no overlap with it, providing very precise checks of the Monte Carlo's modeling of the data. We do not limit the

investigation to input variables but also check the distributions of other kinematic variables not used in the discriminants. We also check the distributions of each discriminant output variable in events with no b tags. Each of these investigations is done for each technique, for 2-jet and 3-jet events separately, and for each category of charged lepton candidates, requiring the examination of thousands of histograms.

A. Multivariate likelihood function

A multivariate likelihood function [85] is one method for combining several sensitive variables. This method makes use of the relative probabilities of finding an event in histograms of each input variable, compared between the signal and the background.

The likelihood function L_k for event class k is constructed using binned probability density functions for each input variable. The probability that an event from sample k will populate bin j of input variable i is defined to be f_{ijk}. The probabilities are normalized so that $\sum_j f_{ijk} = 1$ for all variables i and all samples k. For the signal, $k = 1$, and in this paper, four background classes are used to construct the likelihood function: $Wb\bar{b}$, $t\bar{t}$, $Wc\bar{c}/Wc$, and $W + \text{LF}$, which are event classes $k = 2$, 3, 4, and 5, respectively. Histogram underflows and overflows are properly accounted for. The likelihood function for an event is computed in two steps. First, for each reconstructed variable i, the bin j in which the event falls is obtained, and the quantities

$$p_{ik} = \frac{f_{ijk}}{\sum_{m=1}^{5} f_{ijm}} \qquad (9)$$

are computed for each variable i and each event class k. The p_{ik} are used to compute

$$\mathcal{L}_k = \frac{\prod_{i=1}^{n_{\text{var}}} p_{ik}}{\sum_{m=1}^{5} \prod_{i=1}^{n_{\text{var}}} p_{im}}, \qquad (10)$$

where n_{var} is the number of input variables. The signal likelihood function, referred to as the LF discriminant in the following, is the one which corresponds to the signal class of events, $\mathcal{L}_1$. This method does not take advantage of the correlations between input variables, which may be different between the signal and the background processes. The predicted distributions of the likelihood functions are made from fully simulated Monte Carlo and data sets where appropriate, with all correlations in them, and so while correlations are not taken advantage of, they are included in the necessary modeling. The reduced dependence on the correlations makes the LF analysis an important cross-check on the other analyses, which make use of the correlations. More detailed information on this method can be found in [86,87].

Three likelihood functions are computed for use in the search for single top quark production. The first, L_t, is optimized for the t-channel signal; it is used for events with two jets and one b tag. Another, L_s, is optimized for the s-channel signal; it is applied to events with two jets and two b tags. The L_s-based analysis was separately labeled the LFS analysis in [27]. The third, L_{3j}, is optimized for the sum of both s- and t-channel single top quark production; it is applied to events with three jets. The inputs to these three likelihood functions are described in Secs. VII A 2–VII A 4, respectively.

1. Kinematic constraints

The likelihood function input variables include the squares of the quantum-mechanical matrix elements, using MADGRAPH [50], computed with the measured four-vectors. These calculations depend very strongly on the invariant masses of the $\ell\nu$ system and the $\ell\nu b$ system, which result from the W boson and top quark decay, respectively. The neutrino leaves no trace in the detector; $\not{E}_T$ is an approximation to its transverse momentum, and p_z^ν is not measured. The b quark is also imperfectly reconstructed; a b-tagged jet's energy is an approximation to the b quark's momentum. We solve for the p_z of the neutrino and the energy of the b quark while requiring that $M_{\ell\nu} = M_W$ and $M_{\ell\nu b} = m_t$. The W boson mass constraint results in two solutions. If both are real, the one with the smaller $|p_z|$ is used. If both are complex, a minimal amount of additional $\not{E}_T$ is added parallel to the jet axis assigned to be the b from the top quark's decay until a real solution for $|p_z^\nu|$ can be obtained. In rare cases in which this procedure still fails to produce a real $|p_z^\nu|$, additional $\not{E}_T$ is added along the b-jet axis to minimize the imaginary part of $|p_z^\nu|$, and then a minimal amount of $\not{E}_T$ is added perpendicular to the b-jet axis until a real $|p_z^\nu|$ is obtained.

The top quark mass constraint can be satisfied by scaling the b-jet's energy, holding the direction fixed, until $M_{\ell\nu b} = m_t$. As the b-jet's energy is scaled, the $\not{E}_T$ is adjusted to be consistent with the change. We then recalculate p_z^ν using the M_W constraint described above, and the process is iterated until $M_{\ell\nu b} = m_t$. The resulting four-vectors of the b quark and the neutrino are then used with the measured four-vector of the charged lepton in the matrix element expressions to construct discriminant variables that separate the signal from the background.

2. 2-Jet t-channel likelihood function

The t-channel likelihood function $\mathcal{L}_t$ uses seven variables, and assumes the b-tagged jet comes from top quark decay. The variables used are
 (i) H_T: the scalar sum of the E_T's of the two jets, the lepton E_T, and $\not{E}_T$.
 (ii) $Q \times \eta$: the charge of the lepton times the pseudorapidity of the jet which is not b tagged.

(iii) χ^2_{kin}: the χ^2 of the comparison of the measured b jet energy and the one the kinematic constraints require in order to make $M_{\ell\nu b} = m_t$ and $M_{\ell\nu} = M_W$, using the nominal uncertainty in the b jet's energy. Any additional $\not{E}_{\text{T}}$ which is added to satisfy the $m_{\ell\nu} = M_W$ constraint is added to χ^2_{kin} using the nominal uncertainty in the $\not{E}_{\text{T}}$ measurement.

(iv) $\cos\theta_{\ell j}$: the cosine of the angle between the charged lepton and the untagged jet in the top quark decay frame.

(v) M_{jj}: the invariant mass of the two jets.

(vi) $\text{ME}_{t\text{-chan}}$: the differential cross section for the t-channel process, as computed by MADGRAPH using thef constrained four-vectors of the b, ℓ, and ν.

(vii) The jet flavor separator output b_{NN} described in Sec. VI.

3. 2-Jet s-channel likelihood function

The s-channel likelihood function L_s uses nine variables. Because these events have exactly two jets, both of which are required to be b tagged, we decide which jet comes from the top quark decay with a separate likelihood function that includes the transverse momentum of the b quark, the invariant mass of the b quark and the charged lepton, and the product of the scattering angle of the b jet in the initial quarks' rest frame and the lepton charge. To compute this last variable, the p_z of the neutrino has been solved for using the m_W constraint.

The variables input to L_s are

(i) M_{jj}: the invariant mass of the two jets.

(ii) p_{T}^{jj}: the transverse momentum of the two-jet system.

(iii) ΔR_{jj}: the separation between the two jets in ϕ-η space.

(iv) $M_{\ell\nu b}$: the invariant mass of the charged lepton, the neutrino, and the jet assigned to be the b jet from the top quark decay.

(v) $E_{\text{T}}^{j_1}$: the transverse energy of the leading jet, that is, the jet with the largest E_{T}.

(vi) η_{j_2}: the pseudorapidity of the nonleading jet.

(vii) p_{T}^{ℓ}: the transverse momentum of the charged lepton.

(viii) $Q \times \eta$: the charge of the lepton times the pseudorapidity of the jet which is not assigned to have come from the top quark decay.

(ix) The logarithm of the likelihood ratio constructed by matrix elements computed by MADGRAPH, using the p_z^{ν} solution which maximizes the likelihood described in the next point. This likelihood ratio is defined as $\frac{\text{ME}_s + \text{ME}_t}{\text{ME}_s + \text{ME}_t + \text{ME}_{Wbb}}$.

(x) The output of a kinematic fitter which chooses a solution of p_z^{ν} that maximizes the likelihood of the solution by allowing the values of p_x^{ν} and p_y^{ν} to vary within their uncertainties. This likelihood is multiplied by the likelihood used to choose the b jet that comes from the top quark, and their product is used as a discriminating variable.

4. 3-Jet likelihood function

Three-jet events have more ambiguity in the assignment of jets to quarks than two-jet events. A jet must be assigned to be the one originating from the b quark from top quark decay, and another jet must be assigned to be the recoiling jet, which is a light-flavored quark in the t-channel case and a b quark in the s-channel case. In all there are six possible assignments of jets to quarks not allowing for grouping of jets together. The same procedure described in Sec. VII A 1 is used on all six possible jet assignments. If only one jet is b tagged, it is assumed to be the b quark from top quark decay. If two jets are b tagged, the jet with the highest $-\ln\chi^2 + 0.005 p_{\text{T}}$ is chosen, where χ^2 is the smaller of the outputs of the kinematic fitter, one for each p_z^{ν} solution. This algorithm correctly assigns the b jet 75% of the time.

There is still an ambiguity regarding the proper assignment of the other jets. If exactly one of the remaining jets is b tagged, it is assumed to be from a b quark, and the untagged jet assigned to be the t-channel recoiling jet; otherwise, the jet with larger E_{T} is assigned to be the t-channel recoiling jet. In all cases, the smaller $|p_z^{\nu}|$ solution is used.

The likelihood function L_{3j} is defined with the following input variables:

(i) $M_{\ell\nu b}$: the invariant mass of the charged lepton, the neutrino, and the jet assigned to be the b jet from the top quark decay.

(ii) b_{NN}: the output of the jet-flavor separator.

(iii) The number of b-tagged jets.

(iv) $Q \times \eta$: the charge of the lepton times the pseudorapidity of the jet assigned to be the t-channel recoiling jet.

(v) The smallest ΔR between any two jets, where ΔR is the distance in the ϕ-η plane between a pair of jets.

(vi) The invariant mass of the two jets not assigned to have come from top quark decay.

(vii) $\cos\theta_{\ell j}$: the cosine of the angle between the charged lepton and the jet assigned to be the t-channel recoiling jet in the top quark's rest frame.

(viii) The transverse momentum of the lowest-E_{T} jet.

(ix) The pseudorapidity of the reconstructed W boson.

(x) The transverse momentum of the b jet from top quark decay.

5. Distributions

In each data sample, distinguished by the number of identified jets and the number of b tags, a likelihood function is constructed with the input variables described above. The outputs lie between zero and one, where zero is background-like and one is signal-like. The predicted distributions of the signals and the expected background

processes are shown in Fig. 21 for the four *b*-tag and jet categories. The templates, each normalized to unit area, are shown separately, indicating the separation power for the small signal. The sums of predictions normalized to our signal and background models, which are described in Secs. IV and V, respectively, are compared with the data. Figure 22(a) shows the discriminant output distributions for the data and the predictions summed over all four *b*-tag and jet categories.

6. Validation

The distributions of the input variables to each likelihood function are checked in the zero-, one-, and two-tag samples for two- and three-jet events. Some of the most important variables' validation plots are shown in Secs V E and VII. The good agreement seen between the predictions and the observations in both the input variables and the output variables gives confidence in the validity of the technique.

Each likelihood function is also tested in the untagged sample, although the input variables which depend on *b*-tagging are modified in order to make the test. For example, b_{NN} is fixed to -1 for untagged events, $Q \times \eta$ uses the jet with the largest $|\eta|$ instead of the untagged jet, and the taggable jet with the highest E_T is used as the *b*-tagged jet in variables which use the *b*-tagged jet as an input. The modeling of the modified likelihood function in the untagged events is not perfect, as can be seen in Fig. 22(b). This mismodeling is covered by the systematic uncertainties on the ALPGEN modeling of $W +$ jets events which constitute the bulk of the background. Specifically, using the untagged data as the model for mistagged $W +$ jets events as well as shape uncertainties on ΔR_{jj} and η_{j2} cover the observed discrepancy.

7. Background likelihood functions

Another validation of the Monte Carlo modeling and the likelihood function discriminant technique is given by constructing discriminants that treat each background contribution separately as a signal. These discriminants then can be used to check the modeling of the rates and distributions of the likelihood function outputs for each background in turn by purifying samples of the targeted backgrounds and separating them from the other components. The same procedure of Eq. (10) is followed, except $k = 2$, 3, 4, or 5, corresponding to the $Wb\bar{b}$, $t\bar{t}$, $Wc\bar{c}/Wc$, and the $W +$ LF samples, respectively, changing only the numerator of Eq. (10). Each of these discriminants acts in the same way as the signal discriminant, but instead it separates one category of background from the other categories and also from the signals. Distributions of $L_{W+bottom}$, $L_{t\bar{t}}$, $L_{W+charm}$, and L_{W+LF} are shown in Fig. 23 for *b*-tagged $W + 2$ jet events passing our event selection. The modeling of the rates and shapes of these distributions gives us confidence that the individual back-

ground rates are well predicted and that the input variables to the likelihood function are well modeled for the main background processes, specifically in the way that they are used for the signal discriminant.

B. Matrix element method

The ME method relies on the evaluation of event probabilities for signal and background processes based on calculations of the relevant SM differential cross sections. These probabilities are calculated on an event-by-event basis for the signal and background hypotheses and quantify how likely it is for the event to have originated from a given signal or background process. Rather than combine many complicated variables, the matrix element method uses only the measured energy-momentum four-vectors of each particle to perform its calculation. The mechanics of the method as it is used here are described below. Further information about this method can be found in [88].

1. Event probability

If we could measure the four-vectors of the initial and final-state particles very precisely, the event probability for a specific process would be

$$P_{\text{evt}} \sim \frac{d\sigma}{\sigma},$$

where the differential cross section is given by [7] and

$$d\sigma = \frac{(2\pi)^4 |\mathcal{M}|^2}{4\sqrt{(q_1 \cdot q_2)^2 - m_{q_1}^2 m_{q_2}^2}} d\Phi_n(q_1 + q_2; p_1, \ldots, p_n),$$

(11)

where $\mathcal{M}$ is the Lorentz-invariant matrix element for the process under consideration; q_1, q_2 and m_{q_1}, m_{q_2} are the four momenta and masses of the incident particles; and $d\Phi_n$ is the *n*-body phase space given by [7]

$$d\Phi_n(q_1 + q_2; p_1, \ldots, p_n)$$
$$= \delta^4 \left(q_1 + q_2 - \sum_{i=1}^{n} p_i \right) \prod_{i=1}^{n} \frac{d^3 p_i}{(2\pi)^3 2E_i}. \quad (12)$$

However, several effects have to be considered: (1) the partons in the initial state cannot be measured, (2) neutrinos in the final state are not measured directly, and (3) the energy resolution of the detector cannot be ignored. To address the first point, the differential cross section is weighted by parton distribution functions. To address the second and third points, we integrate over all particle momenta which we do not measure (the momentum of the neutrino), or do not measure well, due to resolution effects (the jet energies). The integration gives a weighted sum over all possible parton-level variables *y* leading to the observed set of variables *x* measured with the CDF detector. The mapping between the particle variables *y* and the measured variables *x* is established with the transfer func-
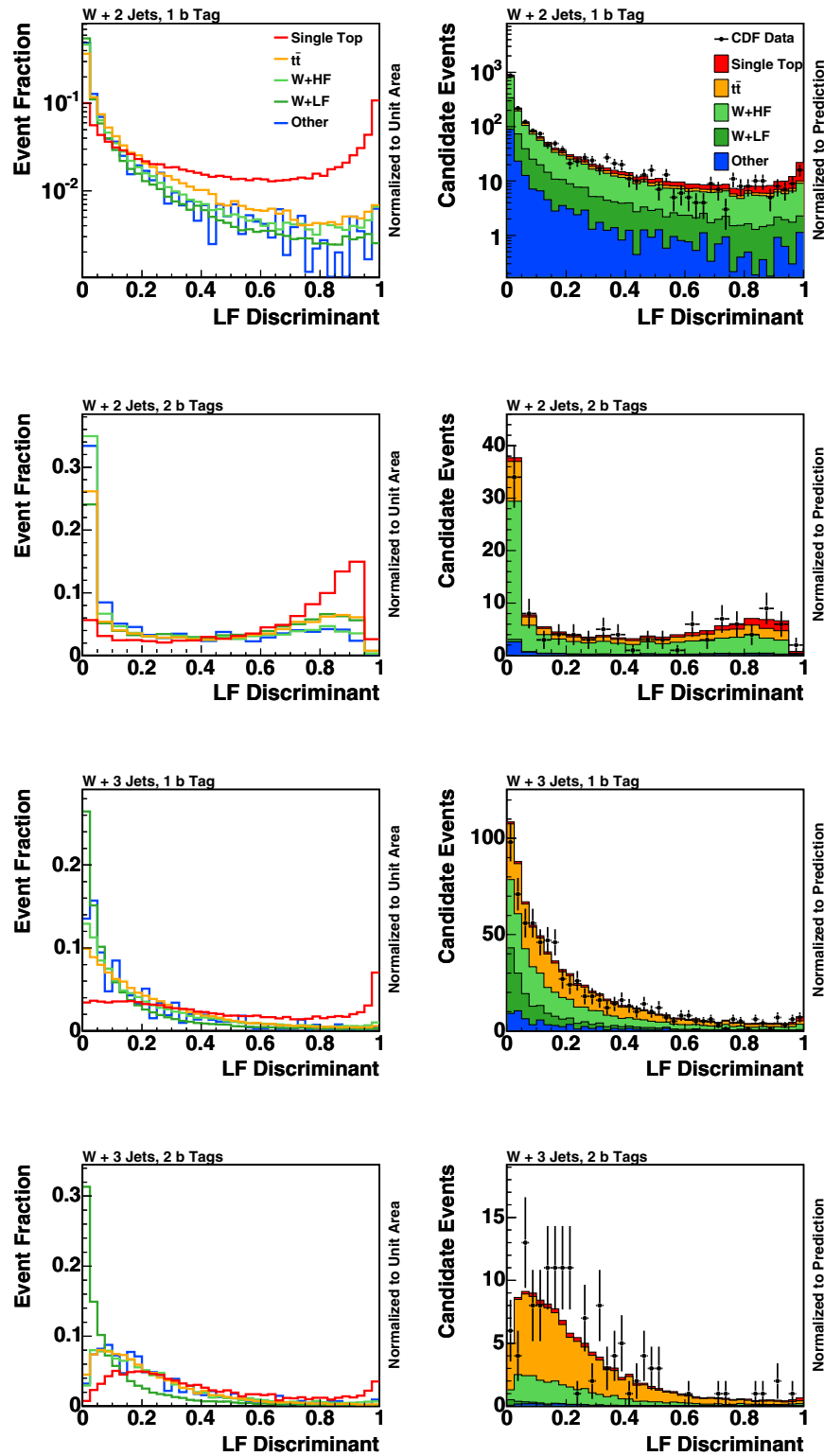
FIG. 21 (color online).   Templates of predictions for the signal and background processes, each scaled to unit area (left) and comparisons of the data with the sum of the predictions (right) of the likelihood function for each selected data sample. Single top quark events are predominantly found on the right-hand sides of the histograms while background events are mostly found on the left-hand sides. The two-jet, one-b-tag plots are shown on a logarithmic vertical scale for clarity, while the others are shown on a linear scale. The data are indicated by points with error bars, and the predictions are shown stacked, with the stacking order following that of the legend.

(a)   (b)
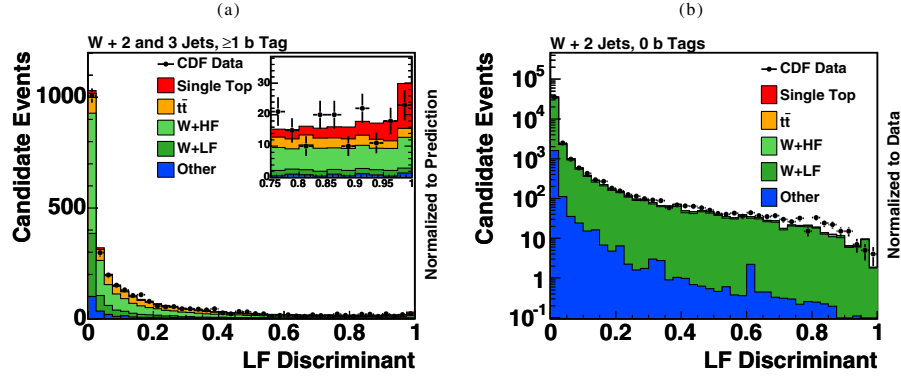
FIG. 22 (color online). Comparison of the data with the sum of the predictions of the likelihood function for the sum of all selected data samples (left) and for two-jet one-tag events (right) applied to the untagged sideband, the latter with appropriate modifications to variables that rely on *b* tagging. The stacking order follows that of the legend. The discrepancies between the prediction and the observation in the untagged sideband seen here are covered by systematic uncertainties on the W + jets background model.

tion $W(y, x)$, which encodes the detector resolution and is described in Sec. VII B 2. Thus, the event probability takes the form

$$P(x) = \frac{1}{\sigma} \int d\sigma(y) dq_1 dq_2 [f(|q_1^z/p_{\text{beam}}|) f(|q_2^z/p_{\text{beam}}|) \\ \times W(y, x)], \tag{13}$$

where $d\sigma(y)$ is the differential cross section in terms of the particle variables; $f(q_i^z/p_{\text{beam}})$ are the PDFs, which are functions of the fraction of the proton momentum p_{beam} carried by quark i. The initial quark momentum is assumed to be in the direction of the beam axis for purposes of this calculation. Substituting Eqs. (11) and (12) into Eq. (13) transforms the event probability to
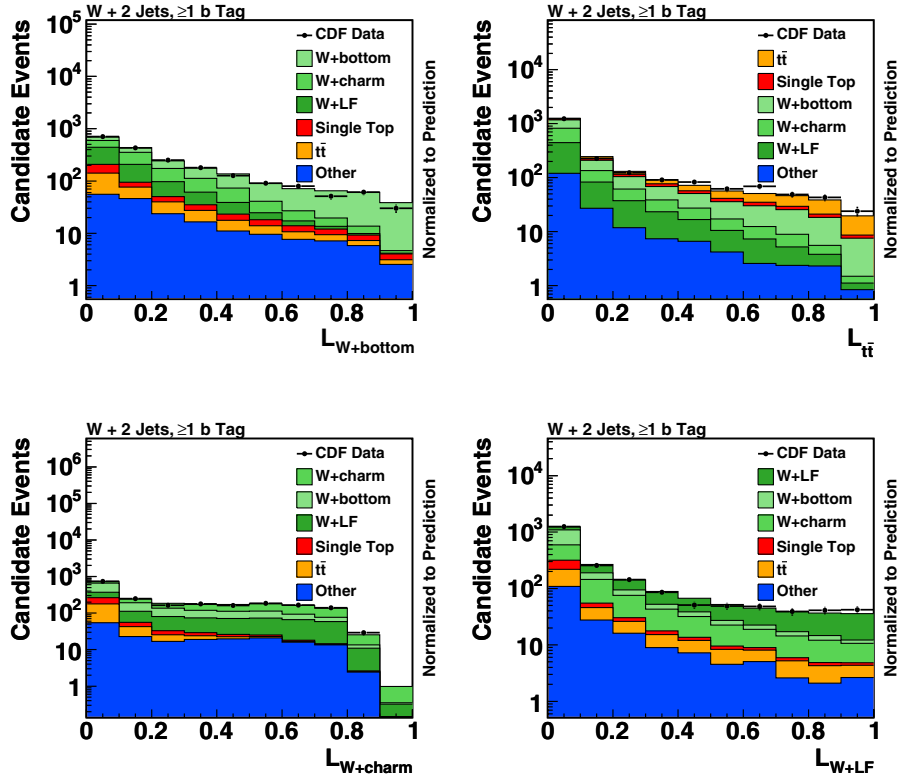
FIG. 23 (color online). Distributions of $L_{W+\text{bottom}}$, $L_{t\bar{t}}$, $L_{W+\text{charm}}$, and $L_{W+\text{LF}}$ for *b*-tagged W + 2 jet events passing our event selection. The signal and background contributions are normalized to the same predicted rates that are used in the signal extraction histograms. In each plot, the background process which the discriminant treats as signal is stacked on top of the other background processes. The stacking orderings follow those of the legends.

$$P(x) = \frac{1}{\sigma} \int 2\pi^4 |\mathcal{M}|^2 \frac{f(E_{q_1}/E_{\text{beam}})}{E_{q_1}}$$

$$\times \frac{f(E_{q_2}/E_{\text{beam}})}{E_{q_2}} W(y, x) d\Phi_4 dE_{q_1} dE_{q_2}, \quad (14)$$

where we have used the approximation $\sqrt{(q_1 \cdot q_2)^2 - m_{q_1}^2 m_{q_2}^2} \simeq 2E_{q_1}E_{q_2}$, neglecting the masses and transverse momenta of the initial partons.

We calculate the squared matrix element $|\mathcal{M}|^2$ for the event probability at LO by using the helicity amplitude subroutines for Feynman diagram evaluations (HELAS) package [89]. The correct subroutine calls for a given process are automatically generated by MADGRAPH [50]. We calculate event probabilities for all significant signal and background processes that can be easily modeled to first order: s-channel and t-channel single top quark production as well as the $Wb\bar{b}$, Wcg, Wgg (shown in Fig. 8), and $t\bar{t}$ (Fig. 9) processes. The Wcg and Wgg processes are only calculated for two-jet events because they have very little contribution to three-jet background.

The matrix elements correspond to fixed-order tree-level calculations and thus are not perfect representations of the probabilities for each process. Since the integrated matrix elements are not interpreted as probabilities but instead are used to form functions that separate signal events from background events, the choice of the matrix element calculation affects the sensitivity of the analysis but not its accuracy. The fully simulated Monte Carlo uses parton showers to approximate higher-order effects on kinematic distributions, and systematic uncertainties are applied to the Monte Carlo modeling in this analysis in the same way as for the other analyses.

While the matrix element analysis does not directly use input variables that are designed to separate signals from backgrounds based on specific kinematic properties such as $M_{\ell\nu b}$, the information carried by these reconstructed variables is represented in the matrix element probabilities. For $M_{\ell\nu b}$ in particular, the pole in the top quark propagator in $\mathcal{M}$ provides sensitivity to this reconstructed quantity. While the other multivariate analyses use the best-fit kinematics corresponding to the measured quantities on each event, the matrix element analysis, by integrating over the unknown parton momenta, extracts more information, also using the measurement uncertainties.

2. Transfer functions

The transfer function, $W(y, x)$, is the probability of measuring the set of observable variables x given specific values of the parton variables y. In the case of well-measured quantities, $W(y, x)$ is taken as a δ function (i.e. the measured momenta are used in the differential cross-section calculation). When the detector resolution cannot be ignored, $W(y, x)$ is a parametrized resolution function

based on fully simulated Monte Carlo events. For unmeasured quantities, such as the three components of the momentum of the neutrino, the transfer function is constant. Including a transfer function between the neutrino's transverse momentum and $\vec{E}_T$ would double-count the transverse momentum sum constraint. The choice of the transfer function affects the sensitivity of the analysis but not its accuracy, since the same transfer function is applied to both the data and the Monte Carlo samples.

The energies of charged leptons are relatively well measured with the CDF detector and we assume δ functions for their transfer functions. The angular resolution of the calorimeter and the muon chambers is also good and we assume δ functions for the transfer functions of the charged lepton and jet directions. The resolution of jet energies, however, is broad and it is described by a transfer function $W_{\text{jet}}(E_{\text{parton}}, E_{\text{jet}})$.

The jet energy transfer functions map parton energies to measured jet energies after correction for instrumental detector effects [49]. This mapping includes effects of radiation, hadronization, measurement resolution, and energy outside the jet cone not included in the reconstruction algorithm. The jet transfer functions are obtained by parametrizing the jet response in fully simulated Monte Carlo events. We parametrize the distribution of the difference between the parton and jet energies as a sum of two Gaussian functions: one to account for the sharp peak and one to account for the asymmetric tail. We determine the parameters of the $W_{\text{jet}}(E_{\text{parton}}, E_{\text{jet}})$ by performing a maximum likelihood fit to jets in events passing the selection requirements. The jets are required to be aligned within a cone of $\Delta R < 0.4$ with a quark or a gluon coming from the hard scattering process.

We create three transfer functions: one for b jets, which is constructed from the b quark from top quark decay in s-channel single top quark events; one for light jets, which is constructed from the light quark in t-channel single top quark events; and one for gluons, which is constructed from the radiated gluon in Wcg events. In each process, the appropriate transfer function is used for each final-state parton.

3. Integration

To account for poorly measured variables, the differential cross section must be integrated over all variables—14 variables for two-jet events, corresponding to the momentum vectors of the four final-state particles (12 variables) and the longitudinal momenta of the initial-state partons (2 variables). There are 11 delta functions inside the integrals: four for total energy and momentum conservation and seven in the transfer functions (three for the charged lepton's momentum vector and four for the jet angles). The calculation of the event probability therefore involves a three-dimensional integration. The integration is performed numerically over the energies of the two quarks

and the longitudinal momentum of the neutrino (p_z^ν). For three-jet events, the additional jet adds one more dimension to the integral.

Because it is not possible to tell which parton resulted in a given jet, we try all possible parton combinations, using the b-tagging information when possible. These probabilities are then added together to create the final event probability.

Careful consideration must be given to $t\bar{t}$ events falling into the $W + 2$ jet and $W + 3$ jet samples because these events have final-state particles that are not observed. In two-jet events, these missing particles could be a charged lepton and a neutrino (in the case of $t\bar{t} \rightarrow \ell^+ \nu_\ell \ell'^- \bar{\nu}_{\ell'} b\bar{b}$ decays) or two quarks (in the case of $t\bar{t} \rightarrow \ell^+ \nu_\ell q\bar{q}' b\bar{b}$ decays), and since both of these are decay products of a W boson, we treat the matrix element in either case as having a final-state W boson that is missed in the detector. The particle assignment is not always correct, but the purpose of the calculation is to construct variables that have maximal separation power between signal and background events, and not that they produce a correct assignment of particles in each event. The choice of which particles are assumed to have been missed is an issue of the optimization of the analysis and not of the validity of the result. We integrate over the three components of the hypothetical missing W boson's momentum, resulting in a six-dimensional integral. In the three-jet case, we integrate over the momenta of one of the quarks from the W boson decay.

The numerical integration for the simpler two-jet s- and t-channel and $Wb\bar{b}$ diagrams is performed using an adaptation of the CERNLIB routine RADMUL [90]. This is a deterministic adaptive quadrature method that performs well for smaller integrations. For the higher-dimensional integrations needed for the three-jet and $t\bar{t}$ matrix elements, a faster integrator is needed. We use the DIVONNE algorithm implemented in the CUBA library [91], which uses a Monte Carlo based technique of stratified sampling over quasirandom numbers to produce its answer.

4. Event probability discriminant

Event probabilities for all processes are calculated for each event for both data events and Monte Carlo simulated events. For each event, we use the event probabilities as ingredients to build an event probability discriminant (*EPD*), a variable for which the distributions of signal events and background events are as different as possible. Motivated by the Neyman-Pearson lemma [92], which states that a likelihood ratio is the most sensitive variable for separating hypotheses, we define the *EPD* to be $EPD = P_s/(P_s + P_b)$, where P_s and P_b are estimates of the signal and background probabilities, respectively. This discriminant is close to zero if $P_b \gg P_s$ and close to unity if $P_s \gg P_b$. There are four *EPD* functions in all, for $W +$ two- or three-jet events with one or two b tags.

Several background processes in this analysis have no b jet in the final state, and the matrix element probabilities do not include detector-level discrimination between b jets and non-b jets. In order to include this extra information, we define the b-jet probability as $b = (b_{NN} + 1)/2$ and use it to weight each matrix element probability by the b flavor probability of its jets. Since single top quark production always has a b quark in the final state, we write the event-probability-discriminant as

$$EPD = \frac{b \cdot P_s}{b \cdot (P_s + P_{Wb\bar{b}} + P_{t\bar{t}}) + (1 - b) \cdot (P_{Wc\bar{c}} + P_{Wcg} + P_{Wgg})}, \tag{15}$$

where $P_s = P_{s\text{-channel}} + P_{t\text{-channel}}$. Each probability is multiplied by an arbitrary normalization factor, which is chosen to maximize the expected sensitivity. Different values are chosen in each b-tag and jet category in order to maximize the sensitivity separately in each. The resulting templates and distributions are shown for all four *EPD* functions in their respective selected data samples in Fig. 24. All of them provide good separation between single top quark events and background events. The sums of predictions normalized to our signal and background models, which are described in Sections IV and V, respectively, are compared with the data. Figure 25(a) corresponds to the sum of all four b-tag and jet categories.

5. Validation

We validate the performance of the Monte Carlo to predict the distribution of each *EPD* by checking the untagged $W +$ jets control samples, setting $b_{NN} = 0.5$ so that it does not affect the *EPD*. An example is shown in Fig. 25(b), for $W +$ two-jet events. The agreement in this control sample gives us confidence that the information used in this analysis is well modeled by the Monte Carlo simulation.

Because the $t\bar{t}$ background is the most signal-like of the background contributions in this analysis, the matrix element distribution is specifically checked in the b-tagged four-jet control sample, which is highly enriched in $t\bar{t}$
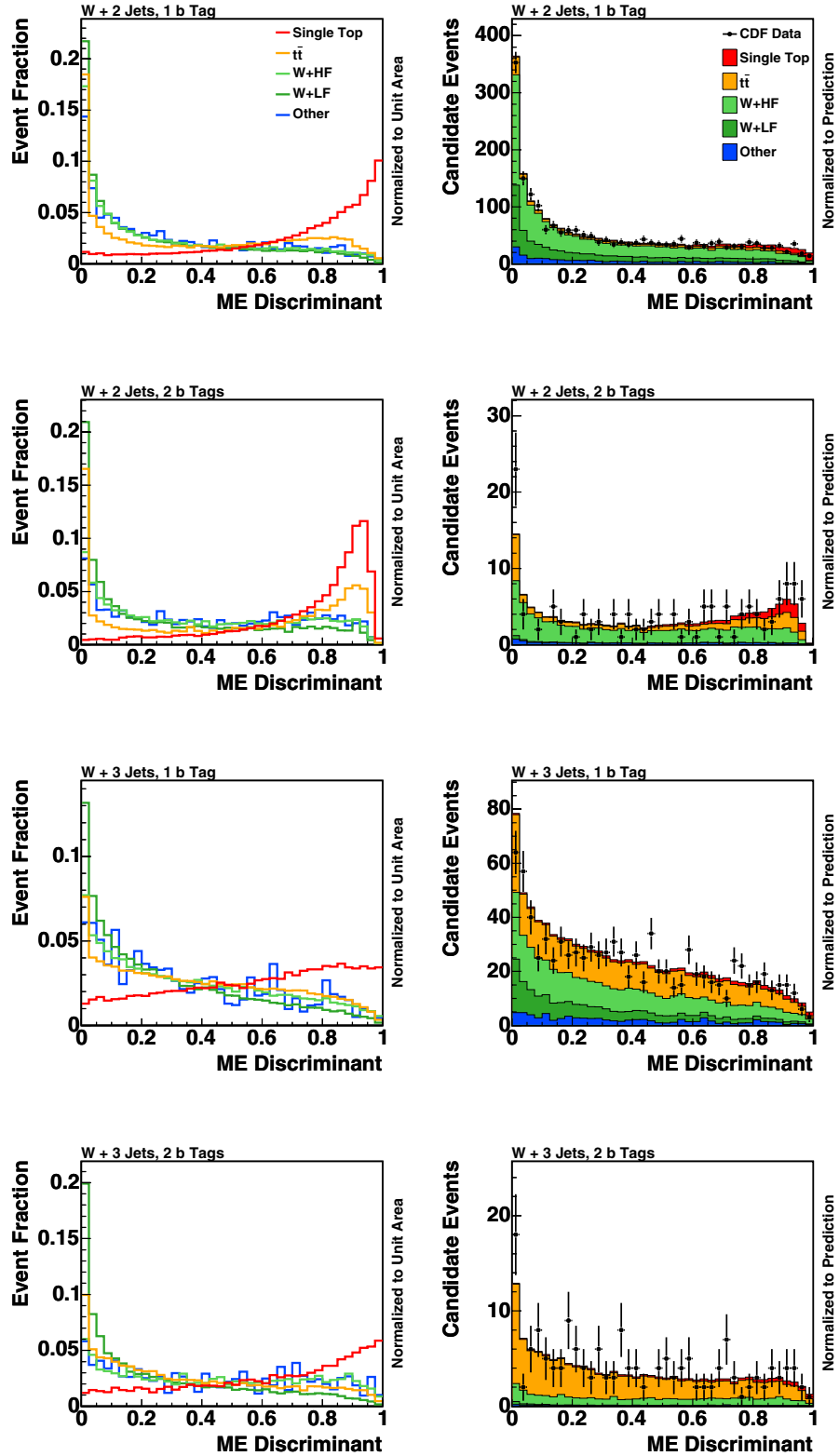
FIG. 24 (color online).   Templates of predictions for the signal and background processes, each scaled to unit area (left) and comparisons of the data with the sum of the predictions (right) of the ME discriminant *EPD* for each selected data sample. Single top quark events are predominantly found on the right-hand sides of the histograms while background events are mostly found on the left-hand sides. The data are indicated by points with error bars, and the predictions are shown stacked, with the stacking order following that of the legend.

(a)   (b)

FIG. 25 (color online).   Comparison of the data with the sum of the predictions of the matrix element discriminant for the sum of all selected data samples (left). The discriminant output for two-jet one-*b*-tag events applied to the untagged *W* + 2 jet control sample (right) shows that the Monte Carlo *W* + 2 jet samples model the ME distribution of the data well. The data are indicated by points with error bars, and the predictions are shown stacked, with the stacking order following that of the legend.

events. Each *EPD* function is validated in this way, for two or three jets, and one or two *b* tags, using the highest-E_T jets in *W* + four-jet events with the appropriate number of *b* tags. An example is shown in Fig. 26 for the two-jet one-*b*-tag *EPD* function.

C. Artificial neural network

A different approach uses artificial neural networks to combine sensitive variables to distinguish a single top quark signal from background events. As with the neural-network flavor separator b_{NN} described in Sec. VI, the NEUROBAYES [83] package is used to create the neural networks. We train a different neural network in each

FIG. 26 (color online).   The event probability discriminant for two-jet one-*b*-tag events applied to the *b*-tagged *W* + 4 jet control sample, showing that the Monte Carlo *t$\bar{t}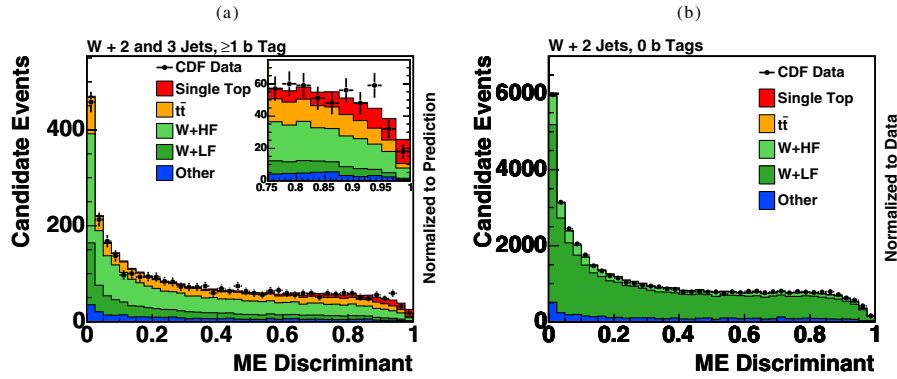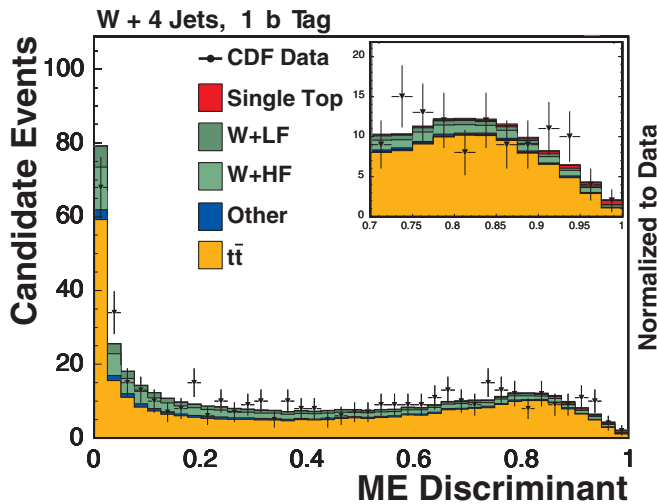$* samples model the *EPD* distribution of the data well. The data are indicated by points with error bars, and the predictions are shown stacked, with the stacking order following that of the legend.

selected data sample—indexed by the number of jets, the number of *b*-tagged jets, and whether the charged lepton candidate is a triggered lepton or an EMC lepton. For all samples, the *t*-channel Monte Carlo is used as the signal training sample except for the two-jet two-*b*-tag events, in which *s*-channel events are treated as a signal. The background training sample is a mix of standard model processes in the ratios of the estimated yields given in Tables I and II.

Each training starts with more than 50 variables, but the training procedure removes those with no significant discriminating power, reducing the number to 11–18 variables. Each neural network has one hidden layer of 15 nodes and one output node.

As in other cases, the transverse momentum of the neutrino is inferred from the $\not{E}_T$ of the event. The component of the momentum of the neutrino along the beam axis is calculated from the assumed mass of the *W* boson and the measured energy and momentum of the charged lepton. A quadratic equation in p_z^ν must be solved. If there is one real solution, we use it. If there are two real solutions, we use the one with the smaller $|p_z^\nu|$. If the two solutions are complex, a kinematic fit which varies the transverse components of $\vec{\not{E}}_T$ is performed to find a solution as close as possible to $\vec{\not{E}}_T$ [93] which results in a real p_z^ν.

If only one jet is *b*-tagged, it is assumed to be from top quark decay. If there is more than one *b*-tagged jet, the jet with the largest $Q_\ell \times \eta$ is chosen. More detailed information about this method can be found in [62].

1 Input variables

The variables used in each network are summarized in Table III. The following are descriptions of the variables:
   (i) $M_{\ell\nu b}$: the reconstructed top quark mass.
   (ii) $M_{\ell\nu bb}$: the reconstructed mass of the charged lepton, the neutrino, and the two *b*-tagged jets in the event.

TABLE III. Summary of variables used in the different neural networks in this analysis. An explanation of the variables is given in the text.

Variable	2-jet		3-jet	
	1-tag	2-tag	1-tag	2-tag
$M_{\ell\nu b}$	X	X	X	
$M_{\ell\nu bb}$		X		X
$M_T^{\ell\nu b}$	X	X	X	X
M_{jj}	X	X	X	X
M_T^W	X	X		
$E_T^{b_{\text{top}}}$		X	X	
$E_T^{b_{\text{other}}}$				X
$\sum E_T^{jj}$			X	X
E_T^{light}	X			X
p_T^ℓ	X			
$p_T^{\ell\nu jj}$			X	X
H_T	X		X	
$\not{E}_T$		X		
$\not{E}_{T,\text{sig}}$			X	
$\cos\theta_{\ell j}$	X		X	X
$\cos\theta_{\ell W}^W$	X			
$\cos\theta_{\ell W}^t$	X			
$\cos\theta_{jj}^t$		X		X
$Q \times \eta$	X		X	X
η_ℓ		X		
η_W	X	X		
$\sum \eta_j$	X		X	
$\Delta\eta_{jj}$			X	X
$\Delta\eta_{t,\text{light}}$			X	
$\sqrt{\hat s}$				X
Centrality				X
Jet flavor separator	X	X	X	

(iii) $M_T^{\ell\nu b}$: the transverse mass of the reconstructed top quark.

(iv) M_{jj}: the invariant mass of the two jets. In the three-jet networks, all combinations of jets are included as variables.

(v) M_T^W: the transverse mass of the reconstructed W boson.

(vi) $E_T^{b_{\text{top}}}$: the transverse energy of the b quark from top decay.

(vii) $E_T^{b_{\text{other}}}$: the transverse energy of the b quark not from top decay.

(viii) $\sum E_T^{jj}$: the sum of the transverse energies of the two most energetic jets. In the three-jet one-tag network, all combinations of two jets are used to construct separate $\sum E_T^{jj}$ input variables.

(ix) E_T^{light}: the transverse energy of the untagged or lowest-energy jet.

(x) p_T^ℓ: the transverse momentum of the charged lepton.

(xi) $p_T^{\ell\nu jj}$: the magnitude of the vector sum of the transverse momentum of the charged lepton, the neutrino, and all the jets in the event.

(xii) H_T: the scalar sum of the transverse energies of the charged lepton, the neutrino, and all the jets in the event.

(xiii) $\not{E}_T$: the missing transverse energy.

(xiv) $\not{E}_{T,\text{sig}}$: the significance of the missing transverse energy $\not{E}_T$, as defined in Eq. (4).

(xv) $\cos\theta_{\ell j}$: the cosine of the angle between the charged lepton and the untagged or lowest-energy jet in the top quark's reference frame.

(xvi) $\cos\theta_{\ell W}^W$: the cosine of the angle between the charged lepton and the reconstructed W boson in the W boson's reference frame.

(xvii) $\cos\theta_{\ell W}^t$: the cosine of the angle between the charged lepton and the reconstructed W boson in the top quark's reference frame.

(xviii) $\cos\theta_{jj}^t$: the cosine of the angle between the two most energetic jets in the top quark's reference frame.

(xix) $Q \times \eta$: the charge of the lepton multiplied by the pseudorapidity of the untagged jet.

(xx) η_ℓ: the pseudorapidity of the charged lepton.

(xxi) η_W: the pseudorapidity of the reconstructed W boson.

(xxii) $\sum \eta_j$: the sum of the pseudorapidities of all jets.

(xxiii) $\Delta\eta_{jj}$: the difference in pseudorapidity of the two most energetic jets. In the three-jet two-tag network, the difference between the two least energetic jets is also used.

(xxiv) $\Delta\eta_{t,\text{light}}$: the difference in pseudorapidity between the untagged or lowest-energy jet and the reconstructed top quark.

(xxv) $\sqrt{\hat s}$: the energy of the center-of-mass system of the hard interaction, defined as the $\ell\nu b$ system plus the recoiling jet.

(xxvi) Centrality: the sum of the transverse energies of the two leading jets divided by $\sqrt{\hat s}$.

(xxvii) b_{NN}: the jet flavor separator neural-network output described in Sec. VI. For two-tag events, the sum of the two outputs is used.

2. Distributions

In each data sample, distinguished by the number of identified jets and the number of b tags, a neural network is constructed with the input variables described above. The outputs lie between -1.0 and $+1.0$, where -1.0 is background-like and $+1.0$ is signal-like. The predicted distributions of the signals and the expected background processes are shown in Fig. 27 for the four b-tag and jet categories. The templates, each normalized to unit area, are shown separately, indicating the separation power for the
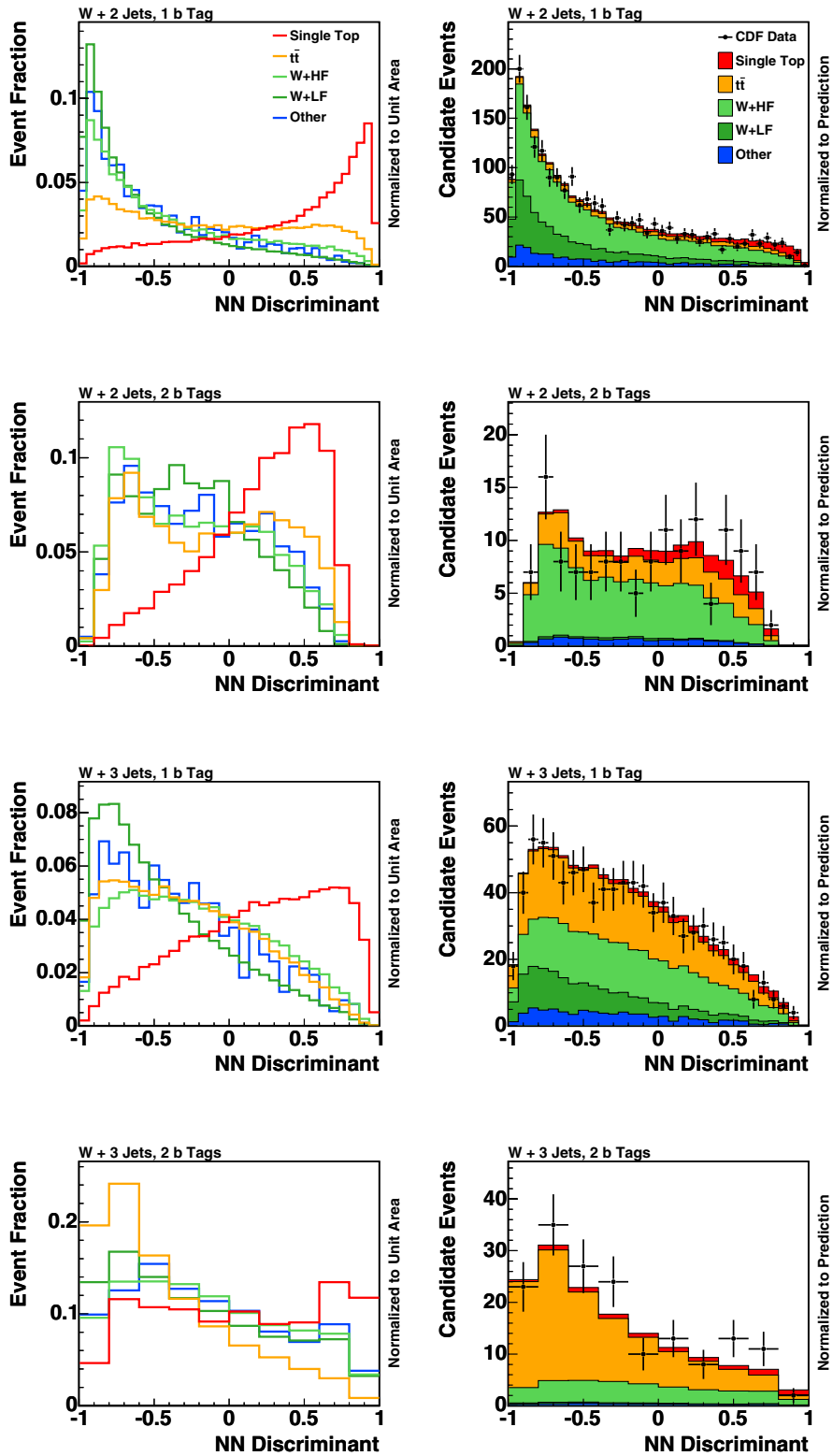
FIG. 27 (color online). Templates of predictions for the signal and background processes, each scaled to unit area (left) and comparisons of the data with the sum of the predictions (right) of the neural-network output for each signal region. Single top quark events are predominantly found on the right-hand sides of the histograms while background events are mostly found on the left-hand sides. The data are indicated by points with error bars, and the predictions are shown stacked, with the stacking order following that of the legend.
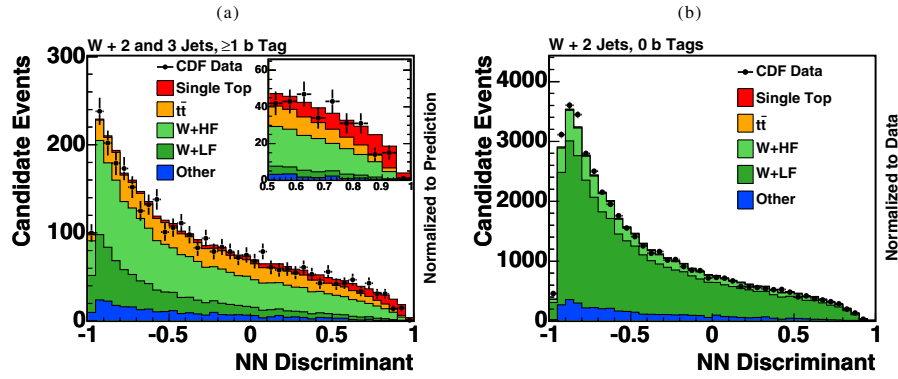
FIG. 28 (color online). Comparison of the data with the sum of the predictions of the neural-network output for the sum of all selected signal data samples (left) and the neural-network output for two-jet one-b-tag events applied to the untagged control sample, showing close modeling of the data and good control over the W + light-flavor shape. The data are indicated by points with error bars, and the predictions are shown stacked, with the stacking order following that of the legend.

small signal. The sums of predictions normalized to our signal and background models, which are described in Secs. IV and V, respectively, are compared with the data. Figure 28(a) corresponds to the sum of all four b-tag and jet categories.

3. Validation

The distributions of the input variables to each neural network are checked in the zero-, one-, and two-tag samples for two- and three-jet events. Comparisons of the observed and predicted distributions of some of the variables which confer the most sensitivity are shown in Secs. V E and VII. The good agreement seen between the predictions and the observations in both the input variables and the output variables gives us confidence in the Monte Carlo modeling of the output discriminant distributions.

We validate the performance of each network by checking it in the untagged sideband, appropriately modifying variables that depend on tagging information. An example is shown in Fig. 28(b). The agreement in this sideband

gives us confidence that the information used in this analysis is well modeled by the Monte Carlo simulation.

4. High NN discriminant output

To achieve confidence in the quality of the signal contribution in the highly signal-enriched region of the NN discriminant, further studies have been conducted. By requiring a NN discriminant output above 0.4 in the event sample with 2 jets and 1 b tag, a signal-to-background ratio of about 1:3 is achieved. This subsample of signal candidates is expected to be highly enriched with signal candidates and is simultaneously sufficient in size to check the Monte Carlo modeling of the data. We compare the expectations of the signal and background processes to the observed data of this subsample in various highly discriminating variables. The agreement is good, as is shown, for example, for the invariant mass of the charged lepton, the neutrino, and the b-tagged jet $M_{\ell\nu b}$ in Fig. 29(a). Since only very signal-like background events are within this subsample, the background shapes are very similar to the signal shapes. This is because the $M_{\ell\nu b}$ is one of the most
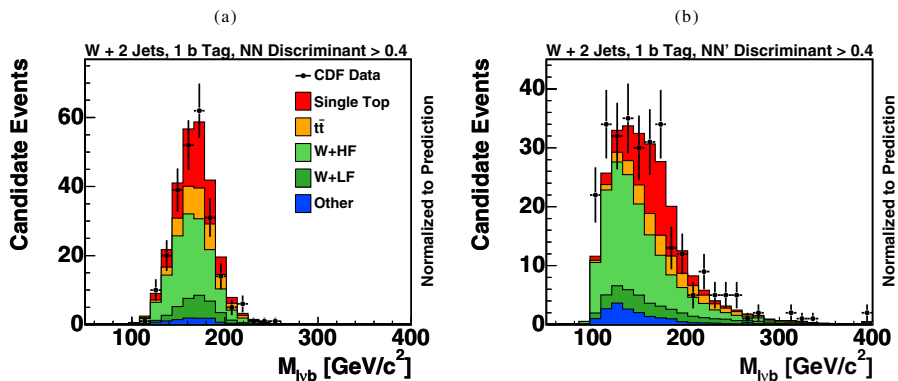

FIG. 29 (color online). Comparison of the predictions and the data for $M_{\ell\nu b}$ for events with an output above 0.4 of the original NN (left) and a specially trained NN$'$ (right) discriminant. The data are indicated by points with error bars, and the predictions are shown stacked, with the stacking order following that of the legend.

important input variables of the NN discriminant, leading to a signal-like sculpted shape for background events in this subsample. As a consequence, the shape of this distribution does not carry information as to whether a signal is present or absent.

To overcome the similar shapes of signal and background events in the signal-enriched subsample, a special neural-network discriminant (NN′) is constructed in exactly the same way as the original, but without $M_{\ell\nu b}$ as an input. Since $M_{\ell\nu b}$ is highly correlated with other original neural-network input variables, such as $M_{\rm T}^{\ell\nu b}$ (with a correlation coefficient of 65%), $H_{\rm T}$ (45%), and M_{jj} (24%), these variables are also omitted for the training of the special NN′ discriminant. Despite the loss of discrimination through the removal of some very important input variables, the NN′ discriminant is still powerful enough to enrich a subsample of events with signal. With the requirement NN′ > 0.4, the signal-to-background ratio is somewhat reduced compared with that of the original NN discriminant. The benefit of this selection is that the predicted distributions of the signal and background are now more different from each other. We predict that background events are dominant at lower values of $M_{\ell\nu b}$ while the single top quark signal is concentrated around the reconstructed top quark mass of 175 GeV/c^2, as shown in Fig. 29(b). Because of the more distinct shapes of the signal and background expectations, the observed shape of the data distribution is no longer explicable by the background prediction alone; a substantial amount of signal events is needed to describe the observed distribution. The NN′ network is used only for this cross-check; it is not included in the main results of this paper.

D. Boosted decision tree

A decision tree classifies events with a series of binary choices; each choice is based on a single variable. Each node in the tree splits the sample into two subsamples, and a decision tree is built using those two subsamples, continuing until the number of events used to predict the signal and background in a node drops below a set minimum. In constructing a tree, for each node, the variable used to split the node's data into subsamples and the value of the variable on the boundary of the two subsamples are chosen to provide optimal separation between signal and background events. The same variable may be used in multiple nodes, and some variables may not be used at all. This procedure results in a series of final nodes with maximally different signal-to-background ratios.

Decision trees allow many input variables to be combined into a single output variable with powerful discrimination between signal and background. Additionally, decision trees are insensitive to the inclusion of poorly discriminating input variables because the training algorithm will not use nondiscriminating variables when constructing its nodes. In this analysis, we train a different BDT in each data sample. We use the TMVA [94] package to perform this analysis [95]. The boosting procedure is described below.

The criterion used to choose the variable used to split each node's data and to set the value of the variable on the boundary is to optimize the Gini index [96] $p(1-p) = sb/(s+b)^2$, where $p = s/(s+b)$ is the purity and s and b are the number of signal and background events in the node, respectively.

A shortcoming of decision trees is their instability with respect to statistical fluctuations in the training sample from which the tree structure is derived. For example, if two input variables exhibit similar separation power, a fluctuation in the training sample may cause the algorithm to decide to use one variable early in the decision chain, while a slightly different training sample may result in a tree which uses the other variable in its place, resulting in a substantially different tree.

This problem is overcome by a boosting [97] procedure that extends this concept from one tree to several trees which form a "forest" of decision trees. The trees are derived from the same training ensemble by reweighting events, and are finally combined into a single classifier which is given by a weighted average of the individual decision trees. Boosting stabilizes the response of the decision trees with respect to fluctuations in the training sample and is able to considerably enhance the performance with respect to a single tree.

This analysis uses the ADABOOST [97] (adaptive boost) algorithm, in which the events that were misclassified in one tree are multiplied by a common boost weight α in the training of the next tree. The boost weight is derived from the fraction of misclassified events, r, of the previous tree,

$$\alpha = \frac{1-r}{r}. \qquad (16)$$

The resulting event classification $y_{\rm BDT}(x)$ for the boosted tree is given by

$$y_{\rm BDT}(x) = \sum_{i \in {\rm forest}} \ln(\alpha_i) \cdot h_i(x), \qquad (17)$$

where the sum is over all trees in the forest. Large (small) values of $y_{\rm BDT}(x)$ indicate a signal-like (background-like) event. The result $h_i(x)$ of an individual tree can either be defined to be +1 (−1) for events ending up in a signal-like (background-like) leaf node according to the majority of training events in that leaf, or $h_i(x)$ can be defined as the purity of the leaf node in which the event is found. We found that the latter option performs better for single-tag samples, while the double tag samples—which have fewer events—perform better when trained with the former option.

While nonoverlapping samples of Monte Carlo events are used to train the trees and to produce predictions of the distributions of their outputs, there is the possibility of "over-training" the trees. If insufficient Monte Carlo events are classified in a node of a tree, then the training
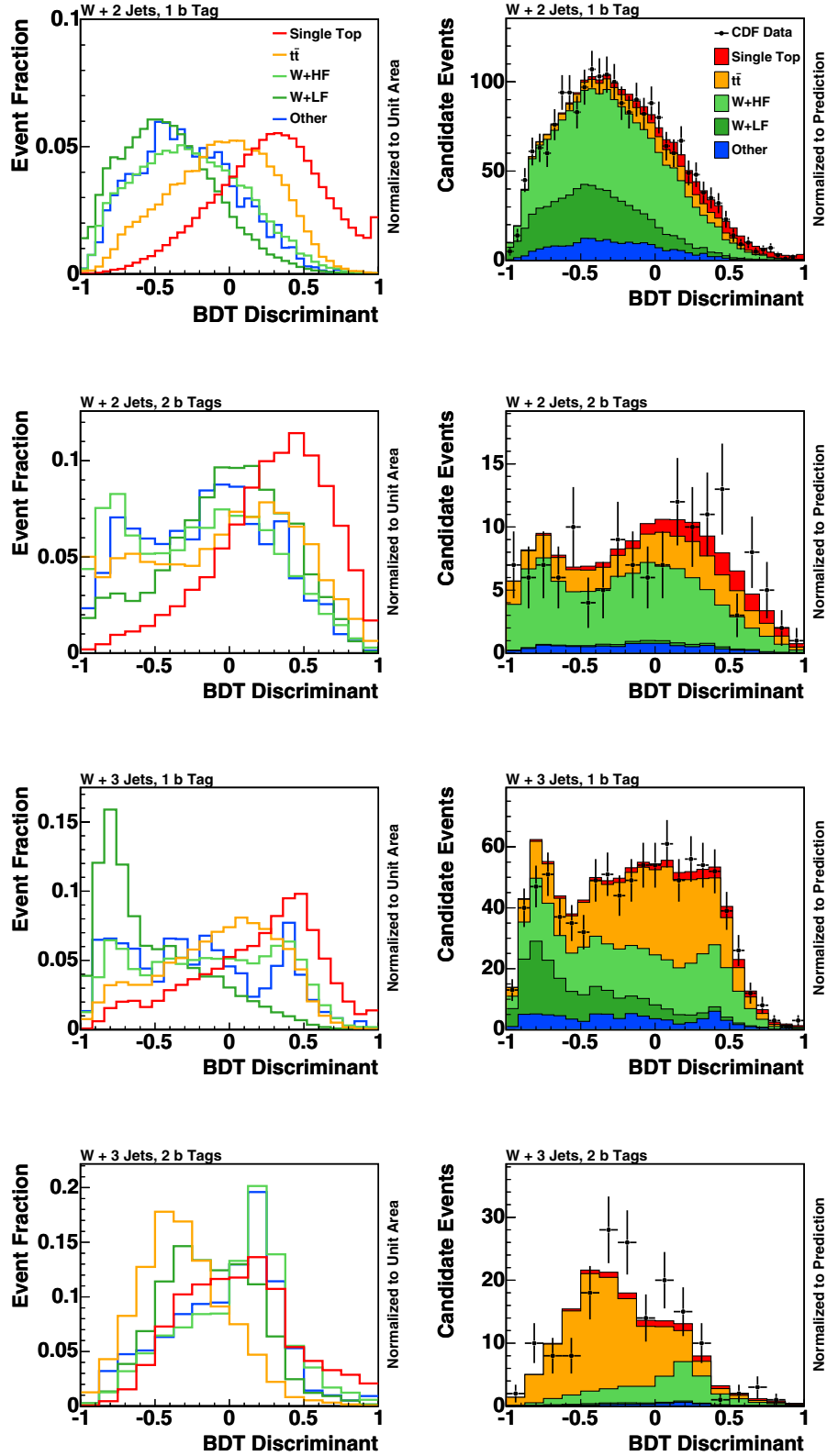
FIG. 30 (color online).   Templates of predictions for the signal and background processes, each scaled to unit area (left) and comparisons of the data with the sum of the predictions (right) of the boosted decision tree output for each data sample. Single top quark events are predominantly found on the right-hand sides of the histograms while background events are mostly found on the left-hand sides. The data are indicated by points with error bars, and the predictions are shown stacked, with the stacking order following that of the legend.

(a)   (b)
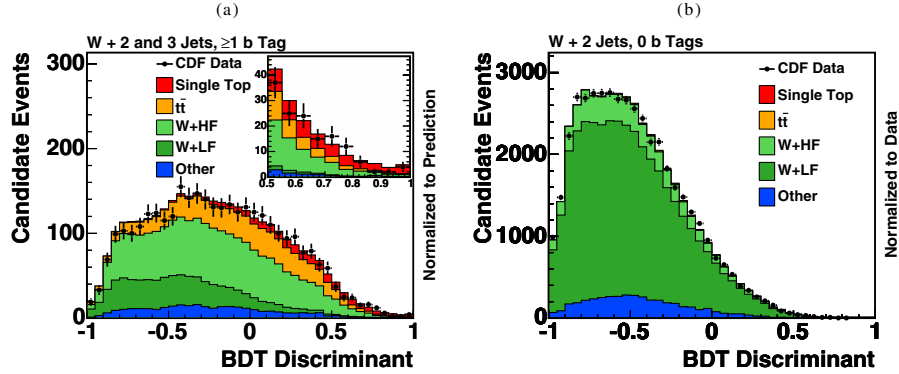
FIG. 31 (color online). Comparison of the data with the sum of the predictions of the BDT output for the sum of all selected data samples (left) and the BDT output for two-jet one-*b*-tag events applied to the untagged two-jet control sample (right), where the dominant contributing process is *W* + light-flavored jets. The data are indicated by points with error bars, and the predictions are shown stacked, with the stacking order following that of the legend.

procedure can falsely optimize to separate the few events it has in the training sample and perform worse on a statistically independent testing sample. In order to remove statistically insignificant nodes from each tree we employ the cost complexity [98] pruning algorithm. Pruning is the process of cutting back a tree from the bottom up after it has been built to its maximum size. Its purpose is to remove statistically insignificant nodes and thus reduce the overtraining of the tree.

The background processes included in the training are $t\bar{t}$ and $Wb\bar{b}$ for double-*b*-tag channels, and those as well as Wc and W + LF for the single-*b*-tag channels. Including the nondominant background processes is not found to significantly increase the performance of the analysis.

1. Distributions

In each data sample, distinguished by the number of identified jets and the number of *b* tags, a BDT is constructed with the input variables described above. The output for each event lies between -1.0 and 1.0, where -1.0 indicates the event has properties that make it appear much more to be a background event than a signal event, and 1.0 indicates the event appears much more likely to have come from a single top signal. The predicted distributions of the signals and the expected background processes are shown in Fig. 30 for the four *b*-tag and jet categories. The templates, each normalized to unit area, are shown separately, indicating the separation power for the small signal. The sums of predictions normalized to our signal and background models, which are described in Secs. IV and V, respectively, are compared with the data. Figure 31(a) corresponds to the sum of all four *b*-tag and jet categories.

2. Validation

The distributions of the input variables to each BDT are checked in the zero, one, and two *b*-tag samples for two-

and three-jet events, and also in the four-jet sample containing events with at least one *b* tag. Some of the most important variables' validation plots are shown in Secs. V E and VII. The good agreement seen between the predictions and the observations in both the input variables and the output variables gives us confidence in the Monte Carlo modeling of the distributions of the discriminant outputs.

We validate the modeling of the backgrounds in each boosted tree by checking it in the sample of events with no *b* tags, separately for events with two and three jets. For variables depending on *b*-tagging information like $M_{\ell\nu b}$ and $Q \times \eta$, the leading jet is chosen as the *b*-tagged jet, and for the $b_{\rm NN}$ variable the output value is randomly taken from a W + LF template. An example is shown in
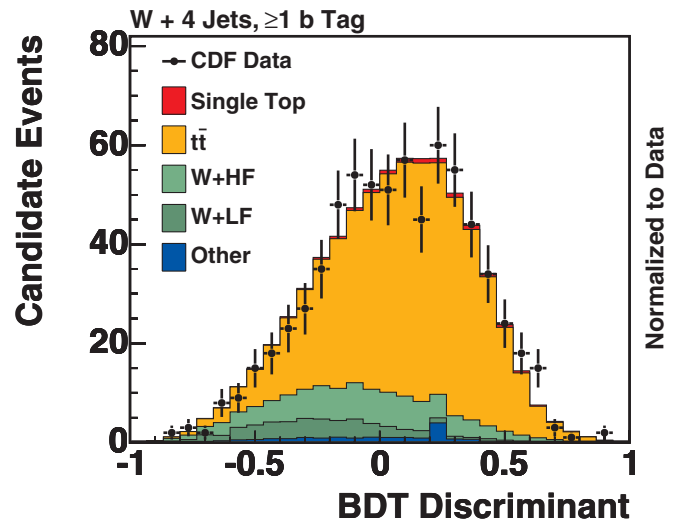

FIG. 32 (color online). The BDT output for four-jet events containing one or more *b* tags. The dominant source of background is $t\bar{t}$ events. The data are indicated with points and the stacked histograms show the prediction, scaled to the total data rate, with the stacking order following that of the legend.

Fig. 31(b), which shows the two-jet, one b-tag BDT tested with the two-jet, zero b-tag sample. The dominant source of background tested in Fig. 31(b) is $W + LF$, and the ALPGEN Monte Carlo predicts the BDT output very well. We further test the four-jet sample with one or more b-tags, shown in Fig. 32, taking the leading two jets to test the two-jet, one b-tag BDT. The dominant background in this test is $t\bar{t}$, and the good modeling of the distribution of the output of the BDT by PYTHIA raises our confidence that this background, too, is modeled well in the data samples.

VIII. SYSTEMATIC UNCERTAINTIES

The search for single top quark production and the measurement of the cross section require substantial input from theoretical models, Monte Carlo simulations, and extrapolations from control samples in data. We assign systematic uncertainties to our predictions and include the effects of these uncertainties on the measured cross sections as well as the significance of the signal.

We consider three categories of systematic uncertainty: uncertainty in the predicted rates of the signal and background processes, uncertainty in the shapes of the distributions of the discriminant variables, and uncertainty arising from the limited number of Monte Carlo events used to predict the signal and background expectations in each bin of each discriminant distribution. Sources of uncertainty may affect multiple signal and background components. The effects of systematic uncertainty from the same source are considered to be fully correlated. For example, the integrated luminosity estimate affects the predictions of the Monte Carlo based background processes and the signal, so the uncertainty on the integrated luminosity affects all of these processes in a correlated way. The effects of different sources of systematic uncertainty are considered to be uncorrelated.

The effects of all systematic uncertainties are included in the hypothesis tests and cross-section measurements performed by each analysis, as described in Sec. IX. Detailed descriptions of the sources of uncertainty and their estimation are given below.

A. Rate uncertainties

Rate uncertainties affect the expected contributions of the signal and background samples. Some sources have asymmetric uncertainties. All rate uncertainties are assigned truncated Gaussian priors, where the truncation prevents predictions from being negative for any source of signal or background. The sources of rate uncertainties in this analysis are described below, and their impacts on the signal and background predictions are summarized in Table IV.

(1) *Integrated luminosity:* A symmetric uncertainty of $\pm 6\%$ is applied to all Monte Carlo based predictions. This uncertainty includes the uncertainty in the $p\bar{p}$ inelastic cross section as well as the uncertainty in the acceptance of CDF's luminosity monitor [44]. The requirement that the primary vertex position in z is within ± 60 cm of the origin causes a

TABLE IV. Sources of systematic uncertainty considered in this analysis. Some uncertainties are listed as ranges, as the impacts of the uncertain parameters depend on the numbers of jets and b tags, and which signal or background component is predicted. The sources "Single top normalization" and "Top mass" are used only in the calculation of the p value.

Source of uncertainty	Rate	Shape	Processes affected
Jet energy scale	0–16%	X	all
Initial-state radiation	0–11%	X	single top, $t\bar{t}$
Final-state radiation	0–15%	X	single top, $t\bar{t}$
Parton distribution functions	2–3%	X	single top, $t\bar{t}$
Acceptance and efficiency scale factors	0–9%		single top, $t\bar{t}$, diboson, $Z/\gamma^* +$ jets
Luminosity	6%		single top, $t\bar{t}$, diboson, $Z/\gamma^* +$ jets
Jet flavor separator		X	all
Mistag model		X	$W +$ light
Non-W model		X	Non-W
Factorization and renormalization scale		X	$Wb\bar{b}$
Jet η distribution		X	all
Jet ΔR distribution		X	all
Non-W normalization	40%		Non-W
$Wb\bar{b}$ and $Wc\bar{c}$ normalization	30%		$Wb\bar{b}$, $Wc\bar{c}$
Wc normalization	30%		Wc
Mistag normalization	17–29%		$W +$ light
$t\bar{t}$ normalization	12%		$t\bar{t}$
Monte Carlo generator	1–5%		single top
Single top normalization	12%		single top
Top mass	2–12%	X	single top, $t\bar{t}$

small acceptance uncertainty that is included as well.

(2) *Theoretical cross sections:* Our MC-based background processes are scaled to theoretical predictions at NLO (or better). We apply the associated theoretical uncertainties. We separate out the effects of the top quark mass from the other sources of uncertainty affecting the theoretical predictions. Not every theoretical cross-section uncertainty is used in each result; details are given in Sec. IX.

(3) *Monte Carlo generator:* Different Monte Carlo generators for the signal result in different acceptances. The deviations are small but are still included as a rate uncertainty on the signal expectation as described in Sec. IV.

(4) *Acceptance and efficiency scale factors:* The predicted rates of the Monte Carlo background processes and of the signals are affected by trigger efficiency, mismodeling of the lepton identification probability, and the *b*-tagging efficiency. Known differences between the data and the simulation are corrected for by scaling the prediction, and uncertainties on these scale factors are collected together in one source of uncertainty since they affect the predictions in the same way.

(5) *Heavy-flavor fraction in W + jets:* The prediction of the $Wb\bar{b}$, $Wc\bar{c}$, and Wc fractions in the $W + 2$ jet and $W + 3$ jet samples are extrapolated from the $W + 1$ jet sample as described in Sec V. It is found that ALPGEN underpredicts the $Wb\bar{b}$ and $Wc\bar{c}$ fractions in the $W + 1$ jet sample by a factor of 1.4 ± 0.4. We assume that the $Wb\bar{b}$ and $Wc\bar{c}$ predictions are correlated. The uncertainty on this scale factor comes from the spread in the measured heavy-flavor fractions using different variables to fit the data, and in the difference between the $Wb\bar{b}$ and $Wc\bar{c}$ scale factors. The Wc prediction from ALPGEN is compared with CDF's measurement [81] and is found not to require scaling, but a separate, uncorrelated uncertainty is assigned to the Wc prediction, with the same relative magnitude as the $Wb\bar{b} + Wc\bar{c}$ uncertainty.

(6) *Mistag estimate:* The method for estimating the yield of events with incorrectly *b*-tagged events is described in Sec. V D. The largest source of systematic uncertainty in this estimate comes from extrapolating from the negative tag rate in the data to positive tags by estimating the asymmetry between positive light-flavor tags and negative light-flavor tags. Other sources of uncertainty come from differences in the negative tag rates of different data samples used to construct the mistag matrix.

(7) *Non-W multijet estimate:* The non-*W* rate prediction varies when the $\not{E}_T$ distribution is constructed with a different number of bins or if different models are used for the non-*W* templates. The $\not{E}_T$ fits also suffer from small data samples, particularly in the double-tagged samples. A relative uncertainty of $\pm 40\%$ is assesed on all non-*W* rate predictions.

(8) *Initial-state radiation (ISR):* The model used for ISR is PYTHIA's "backwards evolution" method [52]. This uncertainty is evaluated by generating new Monte Carlo samples for $t\bar{t}$ and single top quark signals with Λ_{QCD} doubled or divided in half, to generate samples with more ISR and less ISR, respectively. Simultaneously, the initial transverse momentum scale is multiplied by four or divided by four, and the hard scattering scale of the shower is multiplied by four or divided by four, for more ISR and less ISR, respectively. These variations are chosen by comparing Drell-Yan Monte Carlo and data samples. The p_T distributions of dileptons are compared as a function of the dilepton invariant mass, and the ISR more/less prescriptions generously bracket the available data [99]. Since the ISR prediction must be extrapolated from the Z mass scale to the higher-Q^2 scales of $t\bar{t}$ and single top quark events, the variation chosen is much more than is needed to bracket the p_T^Z data.

(9) *Final-state radiation (FSR):* PYTHIA's model of gluon radiation from partons emitted from the hard scattering interaction has been tuned with high precision to LEP data [52]. Nonetheless, uncertainty remains in the radiation from beam remnants, and parameters analogous to those adjusted for ISR are adjusted in PYTHIA for the final-state showering, except for the hard scattering scale parameter. The effects of variations in ISR and FSR are treated as 100% correlated with each other. ISR and FSR rate uncertainties are not evaluated for the $W + $ jets Monte Carlo samples because the rates are scaled to data-driven estimates with associated uncertainties, and the kinematic shapes of all predictions have factorization and renormalization scale uncertainties applied, as discussed below.

(10) *Jet energy scale (JES):* The calibration of the calorimeter response to jets is a multistep process, and each step involves an uncertainty which is propagated to the final jet energy scale [49]. Raw measurements of the jet energies are corrected according to test-beam calibrations, detector non-uniformity, multiple interactions, and energy that is not assigned to the jet because it lies outside of the jet cone. The uncertainties in the jet energy scale are incorporated by processing all events in all Monte Carlo samples with the jet energy scale varied upwards and again downwards. The kinematic properties of each event are affected, and some events are recategorized as having a different
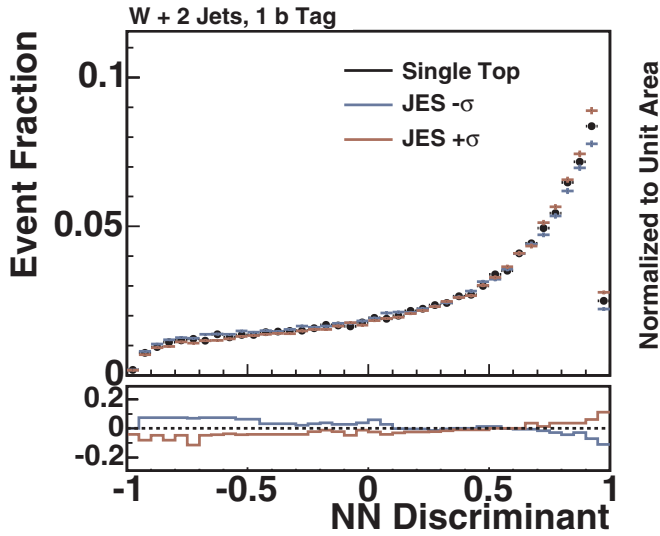
FIG. 33 (color online). An example of systematically shifted shape templates. This figure shows the jet energy scale shifted histograms for the single top quark signal in two-jet one-b-tag events for the NN discriminant. The plot below shows the relative difference between the central shape and the two alternate shapes.

number of jets as jets change their E_T inducing correlated rate and shape uncertainties. An example of the shape uncertainty to the NN analysis's discriminant is shown in Fig. 33.

(11) *Parton distribution functions:* The PDFs used in this analysis are the CTEQ5L set of leading-order PDFs [51]. To evaluate the systematic uncertainties on the rates due to uncertainties in these PDFs, we add in quadrature the differences between the predictions of the following pairs of PDFs:

    (a) CTEQ5L and MRST72 [100], PDF sets computed by different groups. MRST72 is also a leading-order PDF set.

    (b) MRST72 and MRST75, which differ in their value of α_s. The former uses 0.1125; the latter uses 0.1175.

    (c) CTEQ6L and CTEQ6L1, of which the former has a 1-loop α_s correction, and the latter has a 2-loop α_s correction.

    (d) The 20 signed eigenvectors of CTEQ6M, each compared with the default CTEQ5L PDFs.

The PDF uncertainty induces a correlated rate and shape uncertainty in the applicable templates.

B. Shape-only uncertainties

Many of the sources of rate uncertainty listed above also induce distortions in the shapes of the templates for the signals and background processes used to model the data. These include ISR, FSR, JES, and PDF uncertainties. Here

we list the sources of shape uncertainties which do not have associated rate uncertainties.

Shape uncertainty templates are all smoothed with a median smoothing algorithm. This procedure takes the ratio of the systematically shifted histograms to the central histograms and replaces the contents of each bin with the median of the ratios of a five-bin window around the bin. The first two bins and the last two bins are left unaffected by this procedure. The five-bin window was chosen as the minimum size that provides adequate smoothing, as judged from many shape variation ratio histograms. The smoothed ratio histograms are then multiplied by the central histograms to obtain the new varied template histograms. This procedure reduces the impact of limited Monte Carlo statistics in the bins of the central and varied templates.

(i) *Jet flavor separator modeling:* The distribution of b_{NN} for light-flavor jets is found to require a small correction, as described in Sec. VI. The full difference between the uncorrected light-flavor Monte Carlo prediction and the data-derived corrected distribution is taken as a one-sided systematic uncertainty. Since a pure sample of charm jets is not available in the data, a systematic uncertainty is also assessed on the shape of the charm prediction, taking the difference between the distribution predicted by the Monte Carlo simulation and the Monte Carlo distribution altered by the light-flavor correction function. These shifts in the distributions of b_{NN} for these samples are propagated through to the predictions of the shapes of the corresponding discriminant output histograms.

(ii) *Mistag model:* To cover uncertainty in modeling the shape of the analysis discriminant output histograms for mistagged events, the untagged data, weighted by the mistag matrix weights, are used to make an alternate shape template for the mistags. The untagged data largely consist of $W +$ light flavored jets, but there is a contamination from $Wb\bar{b}$, $Wc\bar{c}$, $t\bar{t}$, and even single top quark signal events, making the estimate of the systematic uncertainty conservative.

(iii) *Factorization and renormalization scale:* Because ALPGEN performs fixed-order calculations to create $W +$ jets diagrams, it requires factorization and renormalization scales as inputs. Both of these scales are set for each event in our ALPGEN samples to

$$\sqrt{M_W^2 + \sum_{partons} m_T^2}, \qquad (18)$$

where $m_T^2 = m^2 + p_T^2/c^2$ is the transverse mass of the generated parton. For light partons, u, d, s, g, the mass m is approximately zero; m_b is set to 4.7 GeV/c^2 and m_c is set to 1.5 GeV/c^2. The sum is over all final-state partons excluding the W

boson decay products. In addition, ALPGEN evaluates α_s separately at each gqq and ggg vertex, and the scale at which this is done is set to the transverse momentum of the vertex. The three scales are halved and doubled together in order to produce templates that cover the scale uncertainty. Although ALPGEN's W + heavy-flavor cross-section predictions are strongly dependent on the input scales, we do not assign additional rate uncertainties on the W + heavy flavor yields because we do not use ALPGEN to predict rates; the yields are calibrated using the data. We do not consider the calibrations of these yields to constrain the values of the scales for purposes of estimating the shape uncertainty; we prefer to take the customary variation described above.

(iv) *Non-W flavor composition:* The distribution of b_{NN} is used to fit the flavor fractions in the low-$\not{E}_T$ control samples in order to estimate the central predictions of the flavor composition of b-tagged jets in non-W events, as described in Sec. VI. The limited statistical precision of these fits and the necessity of extrapolating to the higher-$\not{E}_T$ signal region motivates an uncertainty on the flavor composition. The central predictions for the flavor composition are 45% b jets, 40% c jets, and 15% light-flavored jets. The "worst-case" variation of the flavor composition is 60% b jets, 30% c jets, and 10% light-flavor jets, which we use to set our uncertainty. The predictions of the yields are unchanged by this uncertainty, but the distribution of b_{NN} is varied in a correlated way for each analysis, and propagated to the predictions of the discriminant output histograms.

(v) *Jet η distribution:* Checks of the untagged W + 2 jet control region show that the rate of appearance of jets at high $|\eta|$ in the data is underestimated by the prediction [Fig. 34(a)]. Inaccurate modeling of the

distribution of this variable has a potentially significant impact on the analysis because of use of the sensitive variable $Q \times \eta$, which is highly discriminating for events with jets at large $|\eta|$. Three explanations for the discrepancies between data and MC are possible—beam halo overlapping with real W + jets events, miscalibration of the jet energy scale in the forward calorimeters, and ALPGEN mismodeling. We cannot distinguish between these possibilities with the data, and thus choose to reweight all Monte Carlo samples by a weighting factor based on the ratio of the data and Monte Carlo in the untagged sideband, to make alternate shape templates for the discriminants for all Monte Carlo samples. No corresponding rate uncertainty is applied.

(vi) *Jet ΔR distribution:* Similarly, the distribution of $\Delta R(j_1, j_2) = \sqrt{(\Delta \eta)^2 + (\Delta \phi)^2}$, a measure of the angular separation between two jets, is found to be mismodeled in the untagged control sample [Fig. 34(b)]. Modeling this distribution correctly is important because of the use of the input variable M_{jj}, which is highly correlated with $\Delta R(j_1, j_2)$ in our discriminants. The mismodeling of $\Delta R(j_1, j_2)$ is believed to be due to the gluon splitting fraction in ALPGEN, but since this conclusion is not fully supported, we take as a systematic uncertainty the difference in predictions of all Monte Carlo based templates after reweighting them using the ratio of the untagged data to the prediction.

IX. INTERPRETATION

The analyses presented in this paper have two goals: to evaluate the significance of the excess of events compared with the background prediction, and to make a precise measurement of the cross section. These goals have much in common: better separation of signal events from

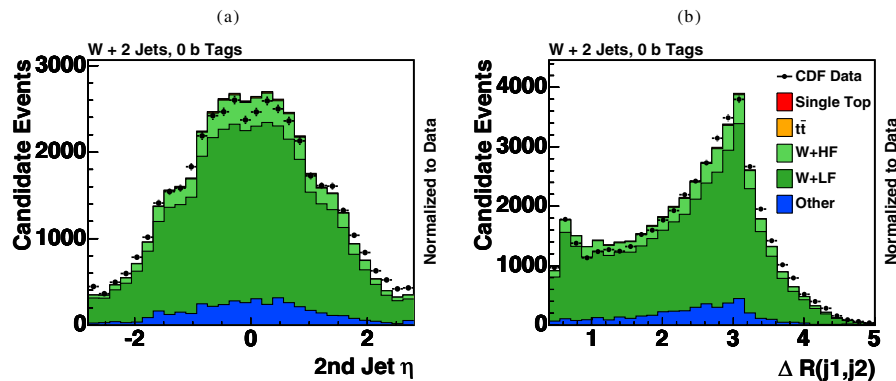FIG. 34 (color online). Graphs showing the poor modeling of the second jet pseudorapidity and the distance between the two jets in the η-ϕ plane. These are accounted for with systematic uncertainties on the shapes of the W + jets predictions. The data are indicated by points with error bars, and the predictions are shown stacked, with the stacking order following that of the legend.

background events and the reduction of uncertainties help improve both the cross-section measurements and the expected significance if a signal is truly present. But there are also differences. For example, the systematic uncertainty on the signal acceptance affects the precision of the cross-section measurement, but it has almost no effect on the observed significance level, and only a minor effect on the predicted significance level; Sec. IX D discusses this point in more detail. More importantly, a precision cross-section measurement relies most on increasing acceptance and understanding the background in a larger sample. The significance of an excess, however, can be much larger if one bin in an analysis has a very low expected background yield and has data in it that are incompatible with that background, even though that bin may not contribute much information to the cross-section measurement.

The contents of the low signal-to-background bins are important for the proper interpretation of the high signal-to-background bins. They serve as signal-depleted control samples which can be used to help constrain the background predictions. Not all bins are fully depleted in signal, and the signal-to-background ratio varies from very small to about 2:1 in some analyses. Simultaneous use of all bins' contents, comparing the observations to the predictions, is needed to optimally measure the cross section and to compute the significance. Systematic uncertainties on the predicted rates and shapes of each component of the background and the two signals (*s*-channel and *t*-channel), and also bin-by-bin systematic uncertainties, affect the extrapolation of the background fits to the signal regions.

These considerations are addressed below, and the procedures for measuring the cross section and the significance of the excess are performed separately. The handling of the systematic uncertainties is Bayesian, in that priors are assigned for the values of the uncertain nuisance parameters, the impacts of the nuisance parameters on the predictions are evaluated, and integrals are performed as described below over the values of the nuisance parameters.

A. Likelihood function

The likelihood function we use in the extraction of the cross section and in the determination of the significance is the product of Poisson probabilities for each bin in each histogram of the discriminant output variable of each channel. Here, the channels are the nonoverlapping data samples defined by the number of jets, the number of *b* tags, and whether the charged lepton candidate is a triggered electron or muon, or whether it was an extended muon coverage candidate event. We do not simply add the distributions of the discriminants in these very different samples because doing so would collect bins with a higher signal purity with those of lower signal purity, diluting our sensitivity. The Poisson probabilities are functions of the number of observed data events in each bin d_i and the

predictions in each bin μ_i, where i ranges from 1 to n_{bins}. The likelihood function is given by

$$L = \prod_{i=1}^{n_{\text{bins}}} \frac{\mu_i^{d_i} e^{-\mu_i}}{d_i!}. \tag{19}$$

The prediction in each bin is a sum over signal and background contributions:

$$\mu_i = \sum_{k=1}^{n_{\text{bkg}}} b_{ik} + \sum_{k=1}^{n_{\text{sig}}} s_{ik}, \tag{20}$$

where b_{ik} is the background prediction in bin i for background source k; n_{bkg} is the total number of background contributions. The signal is the sum of the *s*-channel and *t*-channel contributions; $n_{\text{sig}} = 2$ is the number of signal sources, and the s_{ik} are their predicted yields in each bin. The predictions b_{ik} and s_{ik} depend on n_{nuis} uncertain nuisance parameters θ_m, where $m = 1 \ldots n_{\text{nuis}}$, one for each independent source of systematic uncertainty. These nuisance parameters are given Gaussian priors centered on zero with unit width, and their impacts on the signal and background predictions are described in the steps below.

In the discussion below, the procedure for applying systematic shifts to the signal and background predictions is given step by step, for each kind of systematic uncertainty. Shape uncertainties are applied first, then bin-by-bin uncertainties, and finally rate uncertainties. The bin-by-bin uncertainties arise from limited Monte Carlo (or data from a control sample) statistics and are taken to be independent of each other and all other sources of systematic uncertainty. The steps are labeled b^0 for the central, unvaried background prediction in each bin, and b^4 for the prediction with all systematic uncertainties applied.

The contribution to a bin's prediction from a given source of shape uncertainty is modified by linearly interpolating and extrapolating the difference between the central prediction b_{ik}^0 and the prediction in a histogram corresponding to a $+1\sigma$ variation $\kappa_{b,ik}^{m+}$ if $\theta_m > 0$, and performing a similar operation using a -1σ varied histogram if $\theta_m < 0$:

$$b_{ik}^1 = b_{ik}^0 + \sum_{m=1}^{n_{\text{nuis}}} \begin{cases} (\kappa_{b,ik}^{m+} - b_{ik}^0)\theta_m : & \theta_m \geq 0 \\ (b_{ik}^0 - \kappa_{b,ik}^{m-})\theta_m : & \theta_m < 0 \end{cases}. \tag{21}$$

The parameter list is shared between the signal and background predictions because some sources of systematic uncertainty affect both in a correlated way. The application of shape uncertainties is not allowed to produce a negative prediction in any bin for any source of background or signal:

$$b_{ik}^2 = \max(0, b_{ik}^1). \tag{22}$$

Each template histogram, including the systematically varied histograms, has a statistical uncertainty in each bin. These bin-by-bin uncertainties are linearly interpolated in

each bin in the same way as the predicted values. This procedure works well when the shape-variation templates share all or most of the same events, but it overestimates the bin-by-bin uncertainties when the alternate shape templates are filled with independent samples. If the bin-by-bin uncertainty on b_{ik}^0 is $\delta_{b,ik}^0$, and the bin-by-bin uncertainty on $b_{ik}^{m\pm}$ is $\delta_{b,ik}^{m\pm}$, then

$$\delta_{b,ik}^1 = \delta_{b,ik}^0 + \sum_{m=1}^{n_{\text{nuis}}} \begin{cases} (\delta_{b,ik}^{m+} - \delta_{b,ik}^0)\theta_m: & \theta_m \geq 0 \\ (\delta_{b,ik}^0 - \delta_{b,ik}^{m-})\theta_m: & \theta_m < 0 \end{cases}. \quad (23)$$

Each bin of each background has a nuisance parameter $\eta_{b,ik}$ associated with it;

$$b_{ik}^3 = b_{ik}^2 + \delta_{b,ik}^1 \eta_{b,ik}, \quad (24)$$

where $\eta_{b,ik}$ is drawn from a Gaussian centered on zero with unit width when integrating over it. If $b_{ik}^3 < 0$, then $\eta_{b,ik}$ is redrawn from that Gaussian.

Finally, rate uncertainties are applied multiplicatively. If the fractional uncertainty on b_{ik}^0 due to nuisance parameter m is $\rho_{b,ik}^{m+}$ for a $+1\sigma$ variation and it is $\rho_{b,ik}^{m-}$ for a negative variation, then a quadratic function is determined to make a smooth application of the nuisance parameter to the predicted value:

$$\begin{aligned} b_{ik} &= b_{ik}^4 \\ &= b_{ik}^3 \prod_{m=1}^{n_{\text{nuis}}} \left(1 + \frac{\rho_{b,ik}^{m+} + \rho_{b,ik}^{m-}}{2}\theta_m^2 + \frac{\rho_{b,ik}^{m+} - \rho_{b,ik}^{m-}}{2}\theta_m \right). \end{aligned} \quad (25)$$

The rate uncertainties are applied multiplicatively because most of them affect the rates by scale factors, such as the luminosity and acceptance uncertainties, and they are applied last because they affect the distorted shapes in the same way as the undistorted shapes. Multiple shape uncertainties are treated additively because most of them correspond to events migrating from one bin to another.

The signal predictions are based on their standard model rates. These are scaled to test other values of the single top quark production cross sections:

$$s_{ik} = s_{ik}^4 \beta_k, \quad (26)$$

where β_s scales the s-channel signal and β_t scales the t-channel signal, and the superscript, 4, indicates that the same chain of application of nuisance parameters is applied to the signal prediction as is applied to the background.

The likelihood is a function of the observed data $\mathbf{D} = \{d_i\}$, the signal scale factors $\boldsymbol{\beta} = \{\beta_s, \beta_t\}$, the nuisance parameters $\boldsymbol{\theta} = \{\theta_m\}$ and $\boldsymbol{\eta} = \{\eta_{s,ik}, \eta_{b,ik}\}$, the central values of the signal and background predictions $\boldsymbol{s} = \{s_{ik}^0\}$ and $\boldsymbol{b} = \{b_{ik}^0\}$, and the rate, shape, and bin-by-bin uncertainties $\boldsymbol{\rho} = \{\rho_{b,ik}^{m\pm}, \rho_{s,ik}^{m\pm}\}$, $\boldsymbol{\kappa} = \{\kappa_{b,ik}^{m\pm}, \kappa_{s,ik}^{m\pm}\}$, $\boldsymbol{\delta} = \{\delta_{b,ik}^0, \delta_{b,ik}^{m\pm}, \delta_{s,ik}^0, \delta_{s,ik}^{m\pm}\}$:

$$L = L(\mathbf{D}|\boldsymbol{\beta}, \boldsymbol{\theta}, \boldsymbol{\eta}, s, b, \boldsymbol{\rho}, \boldsymbol{\kappa}, \boldsymbol{\delta}). \quad (27)$$

B. Cross-section measurement

Because the signal template shapes and the $t\bar{t}$ background template rates and shapes are functions of m_t, we quote the single top quark cross section assuming a top quark mass of $m_t = 175\ \text{GeV}/c^2$ and also evaluate $\partial\sigma_{s+t}/\partial m_t$. We therefore do not include the uncertainty on the top quark mass when measuring the cross section.

1. Measurement of σ_{s+t}

We measure the total cross section of single top quark production σ_{s+t}, assuming the SM ratio between s-channel and t-channel production: $\beta_s = \beta_t \equiv \beta$. We use a Bayesian marginalization technique [10] to incorporate the effects of systematic uncertainty:

$$L'(\beta) = \int L(\mathbf{D}|\beta, \boldsymbol{\theta}, \boldsymbol{\eta}, s, b, \boldsymbol{\rho}, \boldsymbol{\kappa}, \boldsymbol{\delta})\pi(\boldsymbol{\theta})\pi(\boldsymbol{\eta})d\boldsymbol{\theta}d\boldsymbol{\eta}, \quad (28)$$

where the π functions are the Bayesian priors assigned to each nuisance parameter. The priors are unit Gaussian functions centered on zero which are truncated whenever the value of a nuisance parameter would result in a nonphysical prediction. The measured cross section corresponds to the maximum of L', which occurs at β^{max}:

$$\sigma_{s+t}^{\text{meas}} = \sigma_{s+t}^{\text{SM}}\beta^{\text{max}}. \quad (29)$$

The uncertainty corresponds to the shortest interval $[\beta_{\text{low}}, \beta_{\text{high}}]$ containing 68% of the integral of the posterior, assuming a uniform positive prior in β $\pi(\beta) = 1$:

$$0.68 = \frac{\int_{\beta_{\text{low}}}^{\beta_{\text{high}}} L'(\beta)\pi(\beta)d\beta}{\int_0^\infty L'(\beta)\pi(\beta)d\beta}. \quad (30)$$

This prescription has the property that the numerical value of the posterior on the low end of the interval is equal to that on the high end of the interval.

Following the example of other top quark properties analyses, the single top quark cross section is measured assuming a top quark mass of $175\ \text{GeV}/c^2$. This measurement is repeated with separate Monte Carlo samples and background estimates generated with masses of $170\ \text{GeV}/c^2$ and $180\ \text{GeV}/c^2$, and the result is used to find $d\sigma_{s+t}/dm_t$.

2. Extraction of bounds on $|V_{tb}|$

The parameter

$$\beta = \frac{\sigma_{s+t}^{\text{meas}}}{\sigma_{s+t}^{\text{SM}}} \quad (31)$$

is identified in the standard model as $|V_{tb}|^2$, under the assumption that $|V_{td}|^2 + |V_{ts}|^2 \ll |V_{tb}|^2$, and that new physics contributions affect only $|V_{tb}|$. The theoretical

uncertainty on $\sigma_{s+t}^{\mathrm{SM}}$ must be introduced for this calculation. The 95% confidence lower limit on $|V_{tb}|$ is calculated by requiring $0 \leq |V_{tb}| \leq 1$ and finding the point at which 95% of the likelihood curve lies to the right of the point. This calculation uses a prior which is flat in $|V_{tb}|^2$.

C. Check for bias

As a cross-check of the cross-section measurement method, simulated pseudoexperiments were generated, randomly fluctuating the systematically uncertain nuisance parameters, propagating their impacts on the predictions of each signal and background source in each bin of each histogram, and drawing random Poisson pseudodata in those bins from the fluctuated means. Samples of pseudoexperiments were generated assuming different signal cross sections, and the cross-section posterior was formed for each one in the same way as it is for the data. We take the value of the cross section that maximizes the posterior as the best-fit value, and calculate the total uncertainty on it in the same way as for the data. The resulting pull distribution is a unit Gaussian, provided that the input cross section for the pseudoexperiments is sufficiently far away from zero.

Because the prior for the cross section does not allow negative values, the procedure described here cannot produce a negative cross-section measurement. For an input cross section of zero, half of the pseudoexperiments will have measured cross sections that are exactly zero, and the other half form a distribution of positive cross sections. We therefore compare the median measured cross section with the input cross section of the pseudoexperiments because the average measured cross section is biased. Distributions of 68% and 95% of extracted cross sections centered on the median are shown as a function of the input cross section in Fig. 35, demonstrating that the measurement technique does not introduce bias for any value of the cross section used as input to the pseudoexperiments. These checks were performed for each analysis; Fig. 35 shows the results for the super discriminant combination, which is described in Sec. X. Some nuisance parameters have asymmetric priors, and the inclusion of their corresponding systematic uncertainties will shift the fitted cross section. This is not a bias which must be corrected but rather it is a consequence of our belief that the values of the uncertain parameters are not centered on their central values.

D. Significance calculation

The other goal of the search is to establish observation of single top quark production. The significance is summarized by a p value, the probability of observing an outcome of an experiment at least as signal-like as the one observed, assuming that a signal is absent. We follow the convention that a p value less than 1.35×10^{-3} constitutes evidence for a signal, and that a p value less than 2.87×10^{-7} constitutes a discovery. These are the one-sided integrals
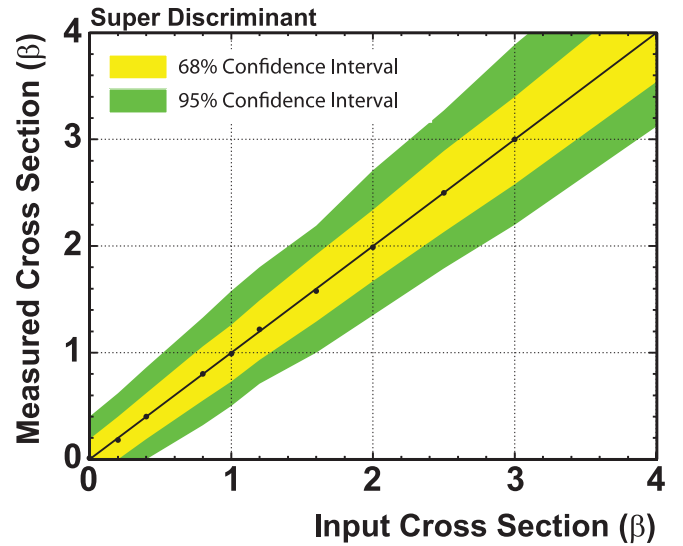

FIG. 35 (color online). Check of the bias of the cross-section measurement method using pseudoexperiments, for the super discriminant combination described in Sec. X. The points indicate the median fit cross section, and the bands show the 68% and 95% quantiles of the distribution of the fitted cross section as functions of the input cross section. A line is drawn showing equal input and fitted cross sections; it is not a fit to the points.

of the tails of a unit Gaussian distribution beyond $+3\sigma$ and $+5\sigma$, respectively.

We rank experimental outcomes on a one-dimensional scale using the likelihood ratio [92]

$$-2\ln Q = -2\ln \frac{L(\mathbf{D}|\beta, \hat{\boldsymbol{\theta}}_{\mathrm{SM}}, \hat{\boldsymbol{\eta}}_{\mathrm{SM}}, s = s_{\mathrm{SM}}, \mathbf{b}, \boldsymbol{\rho}, \boldsymbol{\kappa}, \boldsymbol{\delta})}{L(\mathbf{D}|\beta, \hat{\boldsymbol{\theta}}_0, \hat{\boldsymbol{\eta}}_0, s = 0, \mathbf{b}, \boldsymbol{\rho}, \boldsymbol{\kappa}, \boldsymbol{\delta})},$$
(32)

where $\hat{\boldsymbol{\theta}}_{\mathrm{SM}}$ and $\hat{\boldsymbol{\eta}}_{\mathrm{SM}}$ are the best-fit values of the nuisance parameters which maximize L given the data $\mathbf{D}$, assuming the single top quark signal is present at its SM rate, and $\hat{\boldsymbol{\theta}}_0$ and $\hat{\boldsymbol{\eta}}_0$ are the best-fit values of the nuisance parameters which maximize L assuming that no single top quark signal is present. These fits are employed not to incorporate systematic uncertainties, but to optimize the sensitivity. Fits to other nuisance parameters do not appreciably improve the sensitivity of the search and are not performed. Therefore, only the most important nuisance parameters are fit for the heavy-flavor fraction in $W +$ jets events and the mistag rate.

The desired p value is, then,

$$p = p(-2\ln Q \leq -2\ln Q_{\mathrm{obs}}|s = \mathbf{0}),$$
(33)

since signal-like outcomes have smaller values of $-2\ln Q$ than background-like outcomes. Systematic uncertainties are included not in the definition of $-2\ln Q$, which is a known function of the observed data and is not uncertain, but rather in the expected distributions of $-2\ln Q$ assuming $s = 0$ or $s = s_{\mathrm{SM}}$, since our expectation is what is uncer-

tain. These uncertainties are included in a Bayesian fashion by averaging the distributions of $-2\ln Q$ over variations of the nuisance parameters, weighted by their priors. In practice, this is done by filling histograms of $-2\ln Q$ with the results of simulated pseudoexperiments, each one of which is drawn from predicted distributions after varying the nuisance parameters according to their prior distributions. The fit to the main nuisance parameters insulates $-2\ln Q$ from the fluctuations in the values of the nuisance parameters and optimizes our sensitivity in the presence of uncertainty.

The measured cross section and the p value depend on the observed data. We gauge the performance of our techniques not based on the single random outcome observed in the data but rather by the sensitivity—the distribution of outcomes expected if a signal is present. The sensitivity of the cross section measurement is given by the median expected total uncertainty on the cross section, and the sensitivity of the significance calculation is given by the median expected significance. The distributions from which these sensitivities are computed are Monte Carlo pseudoexperiments with all nuisance parameters fluctuated according to their priors. Optimizations of the analyses were based on the median expected p values, without reference to the observed data. Indeed, the data events passing the event selection requirements were hidden during the analysis optimization.

In the computation of the observed and expected p values, we include all sources of systematic uncertainty in the pseudoexperiments, including the theoretical uncertainty in the signal cross sections and the top quark mass. Because the observed p value is the probability of an upward fluctuation of the background prediction to the observed data, with the outcomes ordered as signal-like based on $-2\ln Q$, the observed p value depends only weakly on the predicted signal model, and, in particular, almost not at all on the predicted signal rate. Hence, the inclusion of the signal rate systematic uncertainty in the observed p value has practically no impact, and the shape uncertainties in the signal model also have little impact (the background shape uncertainties are quite important though). On the other hand, the expected p value and the cross-section measurement depend on the signal model and its uncertainties; a large signal is expected to be easier to discover than a small signal, for example.

X. COMBINATION

The four analyses presented in Sec. VII each seek to establish the existence of single top quark production and to measure the production cross section, each using the same set of selected events. Furthermore, the same models of the signal and background expectations are shared by all four analyses. We therefore expect the results to have a high degree of statistical and systematic correlation. Nonetheless, the techniques used to separate the signal

from the background are different and are not guaranteed to be fully optimal for observation or cross-section measurement purposes; the figures of merit optimized in the construction of each of the discriminants are not directly related to either of our goals, but instead are synthetic functions designed to be easy to use during the training, such as the Gini function [96] used by the BDT analysis, and a sum of classification errors squared used by the neural-network analysis.

The discriminants all perform well in separating the expected signal from the expected background, and in fact their values are highly correlated, event to event, as is expected, since they key on much of the same input information, but in different ways. The coefficients of linear correlation between the four discriminants vary between 0.55 and 0.8, depending on the pair of discriminants chosen and the data or Monte Carlo sample used to evaluate the correlation. Since any invertible function of a discriminant variable has the same separating power as the variable itself, and since the coefficients of linear correlation between pairs of variables change if the variables are transformed, these coefficients are not particularly useful except to verify that indeed the results are highly, but possibly not fully, correlated.

As a more relevant indication of how correlated the analyses are, pseudoexperiments are performed with fully simulated Monte Carlo events analyzed by each of the analyses, and the correlations between the best-fit cross-section values are computed. The coefficients of linear correlation of the output fit results are given in Table V.

The four discriminants, LF, ME, NN, BDT make use of different observable quantities as inputs. In particular, the LF, NN, and BDT discriminants use variables that make assignments of observable particles to hypothetical partons from single top quark production, while the ME method integrates over possible interpretations. Furthermore, since the correlations between pairs of the four discriminants are different for the different physics processes, we expect this information also to be useful in separating the signal from the background processes. In order to extract a cross section and a significance, we need to interpret each event once, and not 4 times, in order for Poisson statistics to apply. We therefore choose to combine the analyses by forming a super discriminant, which is a scalar function of the four input discriminants, and which can be evaluated

TABLE V. Correlation coefficients between pairs of cross-section measurements evaluated on Monte Carlo pseudoexperiments.

	LF	ME	NN	BDT
LF	1.0	0.646	0.672	0.635
ME	...	1.0	0.718	0.694
NN	...	...	1.0	0.850
BDT	...	...	...	1.0

for each event in the data and each event in the simulation samples. The functional form we choose is a neural network, similar to that used in the 2.2 fb^{-1} single top quark combination at CDF [26] as well as the recent $H \rightarrow WW$ search at CDF [102]. The distributions of the super discriminant are used to compute a cross section and a significance in the same way as is done for the component analyses.

In order to train, evaluate, and make predictions which can be compared with the observations for the super discriminant, a common set of events must be analyzed in the ME, NN, LF, and BDT frameworks. The discriminant values are collected from the separate analysis teams for each data event and for each event simulated in Monte Carlo. Missing events or extra events in one or more analyses are investigated and are restored or omitted as discrepancies are found and understood. The $W +$ jets predictions, in particular, involve weighting Monte Carlo events by mistag probabilities and by generator luminosity weights, and these event weights are also unified across four analysis teams. The procedure of making a super discriminant combination provides a strong level of cross checks between analysis teams. It has identified many kinds of simple mistakes and has required us to correct them before proceeding. All of these crosschecks were performed at the stage in which event data were exchanged and before the training of the final discriminant, preserving the blindness of the result.

We further take the opportunity during the combination procedure to optimize our final discriminant for the goal that we set, that is, to maximize the probability of observing single top quark production. A typical approach to neural-network training uses a gradient descent method, such as back-propagation, to minimize the classification error, defined by $\sum(o_i - t_i)^2$, where o_i is the output of the neural network and t_i is the desired output, usually zero for background and one for signal. Although back propagation is a powerful and fast technique for training neural networks, it is not necessarily true that minimizing the classification error will provide the greatest sensitivity in a search. The best choice is to use the median expected p value for discovery of single top quark production as the figure of merit to optimize, but it cannot be computed quickly. Once a candidate network is proposed, the Monte Carlo samples must be run through it, the distributions made, and many millions of pseudoexperiments run in order to evaluate its discovery potential. Even if a more lightweight figure of merit can be computed from the predicted distributions of the signals and background processes, the step of reading through all of the Monte Carlo samples limits the number of candidate neural networks that can be practically considered.

We therefore use the novel neural-network training method of neuro-evolution, which uses genetic algorithms instead of back propagation, to optimize our networks.

This technique allows us to compute an arbitrary figure of merit for a particular network configuration which depends on all of the training events and not just one at a time. The software package we use here is Neuro-Evolution of Augmenting Topologies (NEAT) [103]. NEAT has the ability to optimize both the internode weights and the network topology, adding and rearranging nodes as needed to improve the performance.

We train the NEAT networks using half of the events in each Monte Carlo sample, reserving the other half for use in predicting the outcomes in an unbiased way, and to check for over-training. All background processes are included in the training except non-W because the non-W sample suffers from extremely low statistics. The output values are stored in histograms which are used for the figure of merit calculation. We use two figures of merit which are closely related to the median expected p value, but which can be calculated much more quickly:

(i) *o value:* This figure of merit (so named because it is closely related to the expected p value) is obtained from an ensemble of pseudoexperiments by taking the difference in the median of the test statistic $-2\ln Q$ for the background-only and signal-plus-background hypotheses, divided by the quadrature sum of the widths of those distributions:

$$o = \frac{-2\ln Q_B^{\text{med}} + 2\ln Q_{S+B}^{\text{med}}}{\sqrt{(\Delta 2\ln Q_B)^2 + (\Delta 2\ln Q_{S+B})^2}}. \qquad (34)$$

Typically, 2500 pseudoexperiments give a precision of roughly 1–2% and require one to two minutes to calculate. This is still too slow to be used directly in the evolution, but it is used at the end to select the best network from a sample of high-performing networks identified during the evolution. This figure of merit includes all rate and shape systematic uncertainties.

(ii) *Analytic figure of merit:* As a faster alternative to the figure of merit defined above, we calculate the quadrature sum of an expected signal divided by the square root of the expected background $(s/\sqrt{b})$ in each bin of each histogram. To account for the effects of finite Monte Carlo statistics, this figure of merit is calculated repeatedly, each time letting the value of the expected signal and background processes fluctuate according to a Gaussian distribution with a width corresponding to the Monte Carlo statistical error on each bin. The median of these trials is quoted as the figure of merit. This figure of merit does not include rate and shape systematic uncertainties.

The network training procedure also incorporates an optimization of the binning of the histograms of the network output. In general, the sensitivity is increased by separating events into bins of different purity; combining the contents of bins of different purity degrades our ability
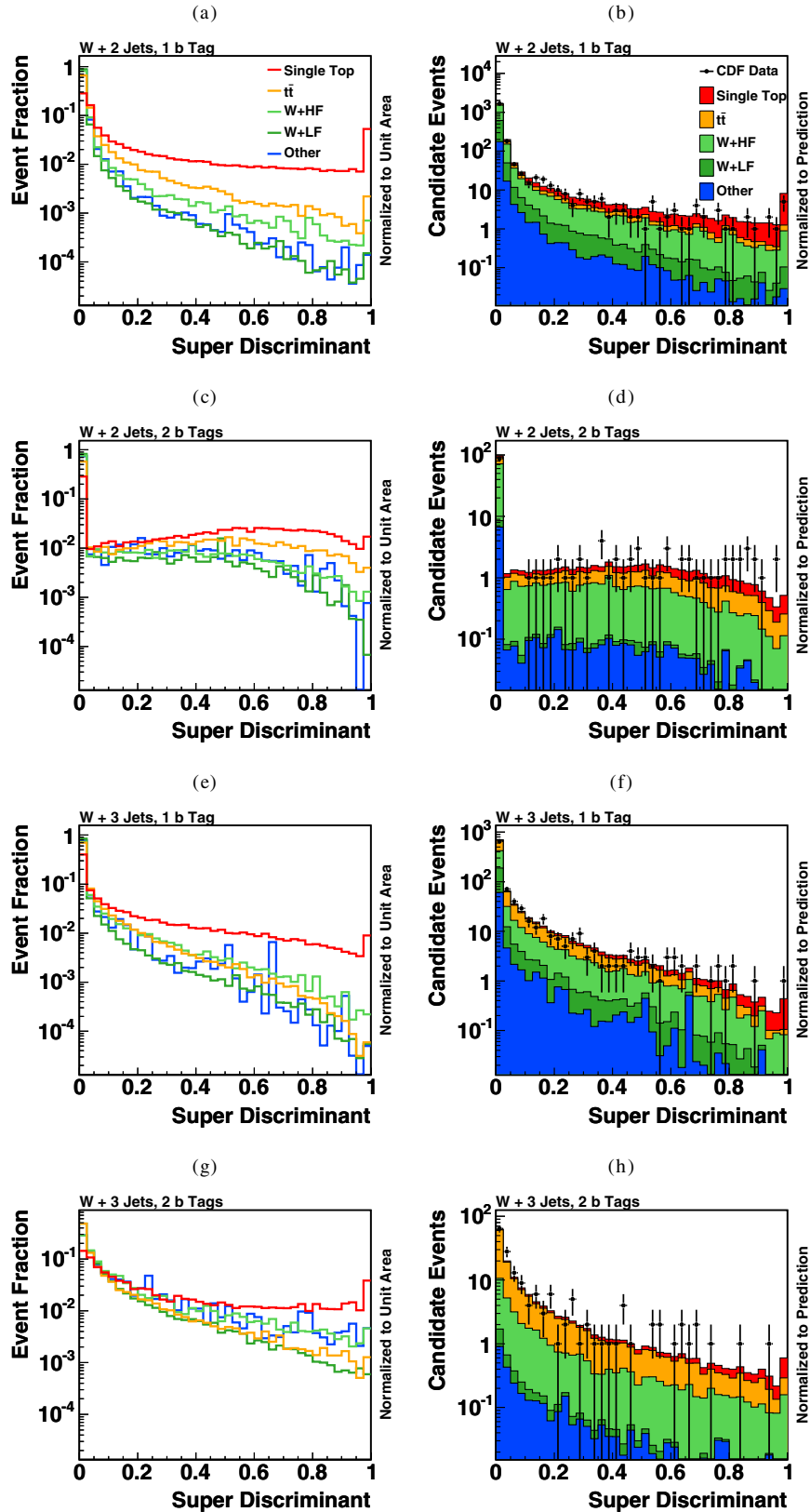
FIG. 36 (color online).   Normalized templates (left) and plots comparing the predicted distributions with data (right) of the final combined neural-network output for each selected data sample. These distributions are more sensitive than any single analysis. The data are indicated by points with error bars, and the predictions are shown stacked, with the stacking order following that of the legend.

to test for the existence of the signal and to measure the cross section. Competing against our desire for fine gradations of purity is our need to have solid predictions of the signal and background yields in each bin with reliable uncertainties—binning the output histogram too finely can result in an overestimate of the sensitivity due to downward fluctuations in the Monte Carlo background predictions. Care is taken here, as described below, to allow the automatic binning optimization to maximize our sensitivity without overestimating it.

The procedure, applied to each channel separately, is to first use a fixed binning of 100 bins in the neural-network output from zero to one. The network output may not necessarily fill all 100 bins; different choices of network parameters, which are optimized by the training, will fill different subsets of these bins. To avoid problems with Monte Carlo statistics at the extreme ends of the distributions, bins at the high end of the histogram are grouped together, and similarly at the low end, sacrificing a bit of separation of signal from background for more robust predictions. At each step, the horizontal axis is relabeled so that the histogram is defined between zero (lowest signal purity) and one (highest purity). The bins are grouped first so that there are no bins with a total background prediction of zero. Next, we require that the histograms have a monotonically decreasing purity as the output variable decreases from one toward zero. If a bin shows an anomalously high purity, its contents are collected with those of all bins with higher network outputs to form a new end bin. Finally, we require that on the high-purity side of the histogram, the background prediction does not drop off too quickly. We expect $\ln \int_x^1 B \propto \ln \int_x^1 S$ for all x in the highest purity region of the histogram. If the background decreases at a faster rate, we group the bins on the high end together until this condition is met. After this procedure, we achieve a signal-to-background ratio exceeding 5:1 in the highest-discriminant output bins in the two-jet, one b-tag sample.

The resulting templates and distributions are shown for all four selected data samples in Fig. 36. In the comparisons of the predictions to the data, the predictions are normalized to our signal and background models, which are described in Secs. IV and V, respectively. Each distribution is more sensitive than any single analysis.

XI. ONE-DIMENSIONAL FIT RESULTS

We use the methods described in Sec. IX to extract the single top cross section, the significance of the excess over the background prediction, and the sensitivity, defined to be the median expected significance, separately for each component analysis described in Sec. VII, and for the SD, which is described in Sec. X. The results are listed in Table VI. The cross-section measurements of the individual analyses are quite similar, which is not surprising due to the overlap in the selected data samples. The measurements are only partially correlated, though, as shown in

TABLE VI. A summary of the analyses covered in this paper, with their measured cross sections, observed significances, and sensitivities, defined to be their median expected p values, converted into Gaussian standard deviations. The analyses are combined into a SD, which is combined with the orthogonal $\cancel{E}_{\mathrm{T}}$ + jets sample (MJ) to make the final CDF combination.

Analysis	Cross section	Significance	Sensitivity
	[pb]	[σ]	[σ]
LF	$1.6^{+0.8}_{-0.7}$	2.4	4.0
ME	$2.5^{+0.7}_{-0.6}$	4.3	4.9
NN	$1.8^{+0.6}_{-0.6}$	3.5	5.2
BDT	$2.1^{+0.7}_{-0.6}$	3.5	5.2
SD	$2.1^{+0.6}_{-0.5}$	4.8	>5.9
MJ	$4.9^{+2.5}_{-2.2}$	2.1	1.4
SD + MJ combination	$2.3^{+0.6}_{-0.5}$	5.0	>5.9

Table V, indicating that the separate analyses extract highly correlated but not entirely identical information from each event.

Because the super discriminant has access to the most information on each event, and because it is optimized for the expected sensitivity, it is the most powerful single analysis. It is followed by the NN and BDT) analyses, and the ME analysis. The LF analysis result in the table is shown only for the t-channel optimized likelihood functions, although the s-channel signals were included in the templates.

A separate result, a measurement just of the s-channel signal cross section, is extracted from just the two-jet, two-b-tag LF analysis, assuming the t-channel signal cross section is at its SM value. The result thus obtained is $\sigma_s^{\mathrm{LF}} = 1.5^{+0.9}_{-0.8}$ pb, with an observed significance of 2.0σ and an expected significance of 1.1σ.

The super discriminant analysis, like the component analyses, fits separately the distributions of events in eight nonoverlapping categories, defined by whether the events have two or three jets passing the selection requirements, one or two b-tags, and whether the charged lepton was a TLC, as opposed to a nontriggered EMC. A separate cross-section fit is done for each of these categories, and the results are shown in Table VII. The dominant components of the uncertainties are statistical, driven by the small data sample sizes in the most pure bins of our discriminant distributions. The cross sections extracted for each final state are consistent with each other within their uncertainties.

The results described above are obtained from the $\ell + \cancel{E}_{\mathrm{T}}$ + jets selection. An entirely separate analysis conducted by CDF is the search for single top quark events in the $\cancel{E}_{\mathrm{T}}$ plus two- and three-jet sample [28] (MJ), which uses a data sample corresponding to 2.1 fb^{-1} of data. The events selected by the MJ analysis do not overlap with those described in this paper because the MJ analysis imposes a charged lepton veto and an isolated high-p_{T}

TABLE VII.   A summary of the measured values of the single top production cross section $\sigma_s + \sigma_t$ using the super discriminant analysis, separately for each of the nonoverlapping final-state categories, based on the number of jets, the number of b tags, and the lepton category. Also listed are the MJ cross-section fit results by b-tagging category.

Category	Cross section [pb]
SD 2-Jet, 1-Tag, TLC	$1.7^{+0.7}_{-0.6}$
SD 2-Jet, 2-Tag, TLC	$4.1^{+2.3}_{-1.9}$
SD 3-Jet, 1-Tag, TLC	$2.4^{+2.1}_{-1.7}$
SD 3-Jet, 2-Tag, TLC	$6.3^{+4.9}_{-4.2}$
SD 2-Jet, 1-Tag, EMC	$2.3^{+1.4}_{-1.1}$
SD 2-Jet, 2-Tag, EMC	$9.8^{+5.7}_{-4.4}$
SD 3-Jet, 1-Tag, EMC	$7.2^{+5.5}_{-4.6}$
SD 3-Jet, 2-Tag, EMC	$0.0^{+8.8}_{-0.0}$
SD	$2.1^{+0.6}_{-0.5}$
MJ 2-Tag	$5.9^{+4.2}_{-3.7}$
MJ 1-Tag + JETPROB	$2.7^{+4.6}_{-2.7}$
MJ 1-Tag	$4.3^{+2.6}_{-2.3}$
MJ	$4.9^{+2.5}_{-2.2}$
SD + MJ combination	$2.3^{+0.6}_{-0.5}$

track veto. The MJ analysis separates its candidate events into three subsamples based on the b-tagging requirements [28], and the results are summarized in Table VII.

The distributions of the super discriminant in the $\ell + \not{E}_T + $ jets sample and the MJ neural-network discriminant in the $\not{E}_T + $ jets sample are shown in Fig. 37, summed over the event categories, even though the cross section fits are performed and the significances are calculated separating the categories. The sums over event categories add the contents of bins of histograms with different s/b together and thus do not show the full separation power of the analyses. Another way to show the combined data set is to collect bins with similar s/b in all of the channels of the SD and MJ discriminant histograms and graph the resulting distribution as a function of $\log_{10}(s/b)$, which is shown in

Fig. 38(a). This distribution isolates, at the high s/b side, the events that contribute the most to the cross-section measurement and the significance. Figure 38(b) shows the integral of this distribution, separately for the background prediction, the signal-plus-background prediction, and the data. The distributions are integrated from the highest s/b side downwards, accumulating events and predictions in the highest s/b bins. The data points are updated on the plot as bins with data entries in them are added to the integral, and thus are highly correlated from point to point. A clear excess of data is seen over the background prediction, not only in the most pure bins, but also as the s/b requirement is loosened, and the excess is consistent with the standard model single top prediction.

Because the $\ell + \not{E}_T + $ jets sample and the $\not{E}_T + $ jets sample have no overlapping events, they can be combined as separate channels using the same likelihood technique described in Sec. IX. The joint posterior distribution including all 11 independent categories simultaneously is shown in Fig. 39(a). From this distribution, we obtain a single top quark cross-section measurement of $\sigma_{s+t} = 2.3^{+0.6}_{-0.5}$ pb, assuming a top quark mass of 175 GeV/c^2. The dependence of the measured cross section on the assumed top quark mass is $\partial\sigma_{s+t}/\partial m_t = +0.02$ pb/(GeV/c^2). Table VII shows the results of fitting for σ_s and σ_t in the separate jet, b-tag, and lepton categories. The dominant source of uncertainty is the statistical component from the data sample size. Our best-fit single top quark cross section is approximately 1 standard deviation below the standard model prediction of [9,10]. The prediction of [11] is somewhat higher, but it is also consistent with our measurement.

To extract $|V_{tb}|$ from the combined measurement, we take advantage of the fact that the production cross section σ_{s+t} is directly proportional to $|V_{tb}|^2$. We use the relation

$$|V_{tb}|^2_{\text{measured}} = \sigma^{\text{measured}}_{s+t}|V_{tb}|^2_{\text{SM}}/\sigma^{\text{SM}}_{s+t}, \qquad (35)$$

where $|V_{tb}|^2_{\text{SM}} \approx 1$ and $\sigma^{\text{SM}}_{s+t} = 2.86 \pm 0.36$ [9,10].
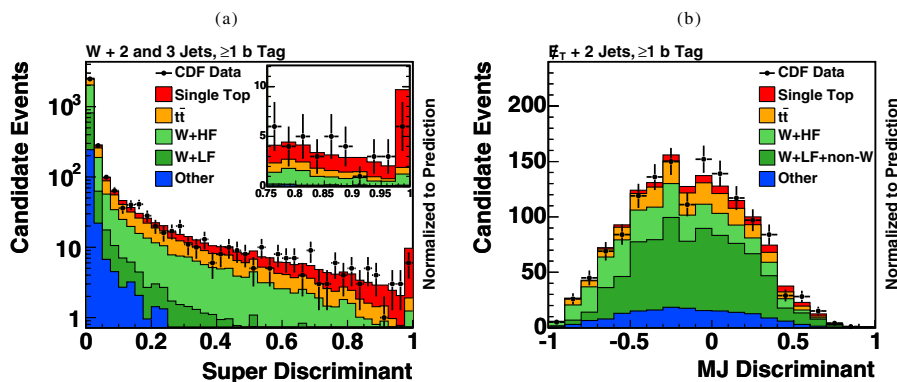

FIG. 37 (color online).   Comparison of the predicted distributions with data summed over all selected data samples of the super discriminant (left) and the MJ discriminant (right). Points with error bars indicate the observed data, while the stacked, shaded histograms show the predictions, including a standard model single top signal. In each panel, the order of the stacked components follows that of the legend.
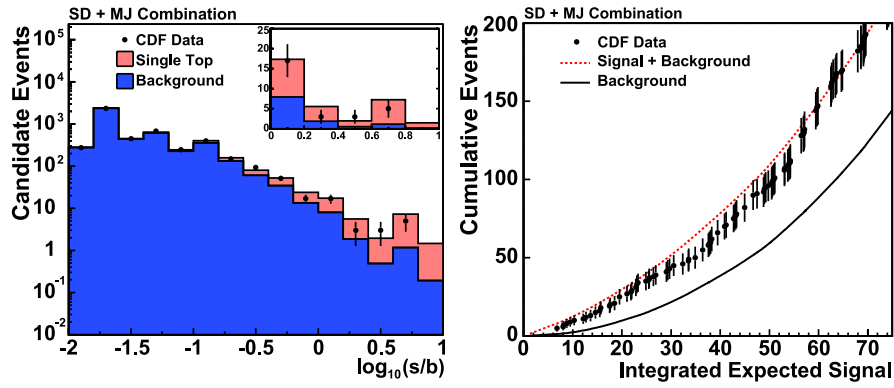
FIG. 38 (color online).   Distributions of data and predictions for the SD and MJ analyses, where bins of similar s/b have been collected together (left). The points with error bars indicate the observed data, while the stacked, shaded histograms show the predictions, including a standard model single top signal. These distributions are integrated starting on the high-s/b side and the resulting cumulative event counts are shown on the right, separately for the observed data, for the background-only prediction and the signal-plus-background prediction.

Equation (35) further assumes that $|V_{tb}|^2 \gg |V_{ts}|^2 + |V_{td}|^2$, because we are assuming that the top quark decays to Wb 100% of the time, and because we assume that the production cross section scales with $|V_{tb}|^2$, while the other CKM matrix elements may contribute as well if they were not very small. We drop the "measured" subscripts and superscripts elsewhere. Figure 39(b) shows the joint posterior distribution of all of our independent channels as a
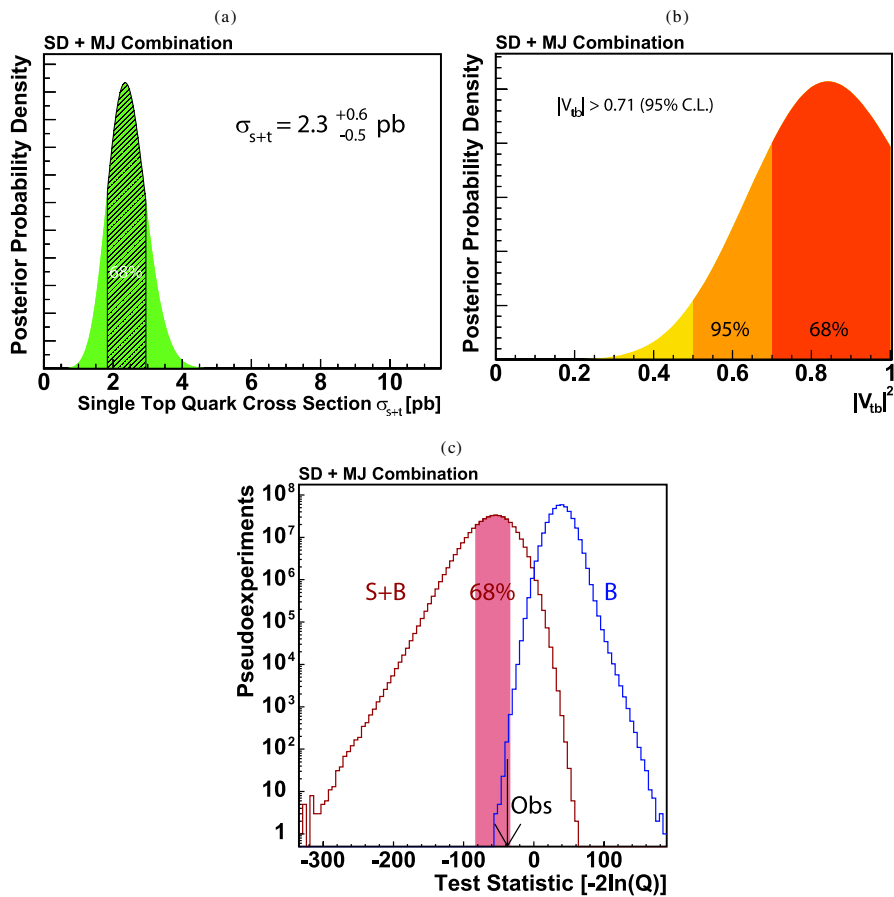

FIG. 39 (color online).   The posterior curve of the cross-section measurement calculated with (a) the super discriminant histograms as inputs, (b) the posterior curve for the $|V_{tb}|$ calculation, and (c) the distributions of $-2\ln Q$ in simulated $S + B$ and B-only pseudoexperiments, assuming a standard model single top quark signal. The value of $-2\ln Q$ observed in the data is indicated with an arrow.

function of $|V_{tb}|^2$ (which includes the theoretical uncertainty on the predicted production rate, which is not part of the cross-section posterior), from which we obtain $|V_{tb}| = 0.91 \pm 0.11(\text{stat} + \text{syst}) \pm 0.07(\text{theory})$ and a 95% confidence level lower limit of $|V_{tb}| > 0.71$.

We compute the p value for the significance of this result as described in Sec. IX D. The distributions of $-2\ln Q$ from which the p value is obtained, are shown in Fig. 39(c). We obtain a p value of 3.1×10^{-7} which corresponds to a 4.985 standard deviation excess of data above the background prediction. We quote this to two significant digits as a 5.0 standard deviation excess. The median expected p value is in excess of 5.9 standard deviations; the precision of this estimate is limited by the number of pseudoexperiments which were fit. The fact that the observed significance is approximately one sigma below its SM expectation is not surprising given that our cross-section measurement is also approximately one sigma below its expectation, although this relation is not strictly guaranteed.

Recently, the cross-section measurement shown here has been combined with that measured by D0 [24]. The same technique for extracting the cross section in combination as for each individual measurement is used [104], and the best-fit cross section is $\sigma_{s+t} = 2.76^{+0.58}_{-0.47}$ pb, assuming $m_t = 170 \text{ GeV}/c^2$.

XII. TWO-DIMENSIONAL FIT RESULTS

The extraction of the combined signal cross section σ_{s+t} proceeds by constructing a one-dimensional Bayesian posterior with a uniform prior in the cross section to be measured. An extension of this is to form the posterior in the two-dimensional plane, σ_s vs σ_t, and to extract the s-channel and the t-channel cross sections separately. We assume a uniform prior in the σ_s vs σ_t plane, and integrate over the nuisance parameters in the same way as we did for the one-dimensional cross-section extraction. The input histograms for this extraction are the distributions of the super discriminant for the W + jets analyses, and the MJ discriminant histograms are also included, exactly as is done for the one-dimensional cross-section fit.

The best-fit cross section is the one for which the posterior is maximized, and corresponds to $\sigma_s = 1.8^{+0.7}_{-0.5}$ pb and $\sigma_t = 0.8^{+0.4}_{-0.4}$ pb. The uncertainties on the measurements of σ_s and σ_t are correlated with each other because s-channel and t-channel signals both populate the signal-like bins of each of our discriminant variables. Regions of 68.3%, 95.5%, and 99.7% credibility are derived from the distribution of the posterior by evaluating the smallest region in area that contains 68.3%, 95.5% or 99.7% of the integral of the posterior. Each region has the property that the numerical values of the posterior along the boundary of the region are equal to each other. The best-fit values, the credibility regions, and the SM predictions of σ_s and σ_t are shown in Fig. 40. We compare these with the
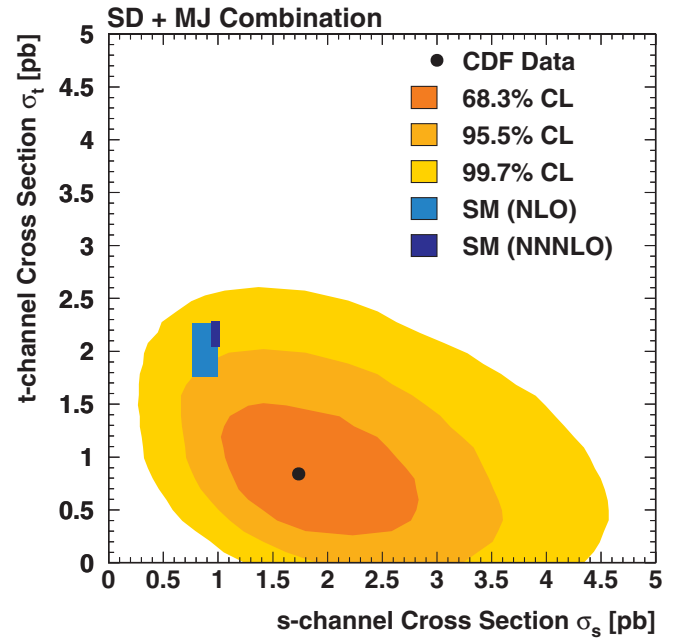

FIG. 40 (color online). The results of the two-dimensional fit for σ_s and σ_t. The black point shows the best-fit value, and the 68.3%, 95.5%, and 99.7% credibility regions are shown as shaded areas. The SM predictions are also indicated with their theoretical uncertainties. The SM predictions shown are those of [9,10] (NLO) and [11] (NNNLO).

NLO SM predictions of $\sigma_t = 1.98 \pm 0.25$ pb and $\sigma_s = 0.88 \pm 0.11$ pb [9,10], and also with the NNNLO predictions of $\sigma_t = 2.16 \pm 0.12$ pb and $\sigma_s = 0.98 \pm 0.04$ pb [11].

The coverage of the technique is checked by generating 1500 pseudo-datasets randomly drawn from systematically varied predictions assuming that a single top signal is present as predicted by the SM, and performing the two-dimensional extraction of σ_s and σ_t for each one in the same way as is done for the data. No bias is seen in the median fit σ_s and σ_t values. Each pseudo-dataset has a corresponding set of regions at 68.3%, 95.5%, and 99.7% credibility. The fractions of the pseudo-datasets' fit bands that contain the input prediction for σ_s and σ_t are consistent with the credibility levels at which the bands are quoted.

The two-dimensional fit result is not in good agreement with the SM prediction; the difference is at approximately the 2 standard deviation level of significance. The differences between the measured values of the s- and t-channel cross sections and their SM predictions are driven by the deficit of events observed in the high-discriminant output regions of the two-jet, one-b-tag channels relative to the SM signal-plus background prediction as shown in Fig. 36(b), and the excess of events observed in the two-jet, two-b-tag distributions, as shown in Fig. 36(d). The measured total cross sections in these jet and b-tagging

categories, listed in Table VII, show the effects of these discrepancies with respect to the SM predictions.

The newer calculation of the t-channel kinematic distributions [56,57] predicts a larger fraction of t-channel signal events with a visible recoiling b jet, which is normally not reconstructed because it is beyond the forward acceptance of the detector or because the jet E_T is too small. This calculation has almost the same overall cross-section prediction for σ_t as the one we use elsewhere in this paper [9], but it reduces the two-jet, one b-tag prediction for the t-channel signal and raises the two-jet two-b-tag and 3-jet predictions. After fully simulating and reconstructing the signal events, the effects on the predicted yields are small; the 3-jet channels' contribution to our measurement sensitivity is also small. The change to the 1D and 2D fit results is not noticeable when using the model of [56,57] compared to our central prediction within the rounding precision of the results we quote.

The t-channel process is sensitive to the b quark PDF of the proton, while the s-channel process is not. The low measured value of σ_t reported here is not in good agreement with the SM predictions. The D0 Collaboration has recently measured $\sigma_t = 3.14^{+0.94}_{-0.80}$ pb using a data sample corresponding to 2.3 fb^{-1} of integrated luminosity [105], which is larger than the standard model prediction. Taken together, there is insufficient evidence to exclude a standard model explanation of the results.

XIII. SUMMARY

The observation of single top quark production poses many difficult experimental challenges. CDF performs this analysis in proton-antiproton collisions at 1.96 TeV in events with a leptonically decaying W boson and jets. The low signal-to-background ratio in the data samples passing our selection requirements necessitates precise modeling of the signal and background kinematic distributions with matrix element Monte Carlo generators using full parton showering and detailed detector simulation, and also requires the normalization of the dominant background rates to measured rates in sideband data samples. The small signals and large, uncertain background processes also require us to take maximum advantage of the expected kinematic and flavor differences between the signals and the background processes. We develop novel, powerful techniques for combining information from several observable quantities computed for each event. We purify a subsample of single top quark events with a predicted signal-to-background ratio exceeding 5:1 from a sample starting with a signal-to-background ratio of 1:16 after b tagging.

Our final discriminant variables are functions of many kinematic and b-tagging variables. Incorrect modeling of one or more variables, or even of the correlations between variables, can bias the results. We therefore evaluate an exhaustive list of systematic uncertainties which affect the predicted signal and background components' rates and kinematic distributions, including both theoretical uncertainties and uncertainties which arise from discrepancies observed between the data and the simulations in control regions. The correlations between the systematic uncertainties on the rate and shape predictions of the signal and background processes in several data samples are taken into account in all of the results and in computing the expected sensitivities presented in this paper. We also consider Monte Carlo statistical uncertainties in each bin of each template histogram in each channel independently. We constrain the major background rates *in situ* in the selected event samples to further reduce the uncertainties in their values and to improve the sensitivity of our results.

Our analyses were optimized based on predictions and were blinded to the data during their development. The analyses were cross-checked using the data in control samples before looking at the data in the signal regions. We perform many checks of our methods—we compare the observed and predicted distributions of the discriminant input and output variables in independent control samples, and we also train discriminants that enrich samples of each background as if it were signal. The vast majority of our cross checks show that the predictions model the data very well, and those that show discrepancies contribute to our systematic uncertainties.

The four analyses in the $\ell + \not{E}_T + $ jets sample described in this paper are combined with a statistically independent analysis in the $\not{E}_T + $ jets sample [28] to maximize the total sensitivity. We report an observation of electroweak single top quark production with a p value of 3.1×10^{-7}, which corresponds to a significance of 5.0 standard deviations. The measured value of the combined s- and t-channel cross section is $\sigma_{s+t} = 2.3^{+0.6}_{-0.5}$ pb assuming the top quark mass is 175 GeV/c^2, and also assuming the SM value of σ_s/σ_t. The dependence of the measured cross section on the assumed top quark mass is $\partial \sigma_{s+t}/\partial m_t = +0.02$ pbc^2/GeV. We extract a value of $|V_{tb}| = 0.91 \pm 0.11$(stat + syst) ± 0.07(theory) and a 95% confidence level lower limit of $|V_{tb}| > 0.71$, using the prediction of [9,10] for the SM cross section, and also assuming that $|V_{tb}|^2 \gg |V_{ts}|^2 + |V_{td}|^2$. With a two-dimensional fit for σ_s and σ_t, using the same combination of analyses as the one-dimensional fit, we obtain $\sigma_s = 1.8^{+0.7}_{-0.5}$ pb and $\sigma_t = 0.8^{+0.4}_{-0.4}$ pb.

[1] Tevatron Electroweak Working Group, CDF Collaboration, and D0 Collaboration, arXiv:1007.3178.
[2] F. Abe *et al.* (CDF Collaboration), Phys. Rev. Lett. **74**, 2626 (1995).
[3] S. Abachi *et al.* (D0 Collaboration), Phys. Rev. Lett. **74**, 2632 (1995).
[4] A. Abulencia *et al.* (CDF Collaboration), Phys. Rev. Lett. **97**, 082004 (2006).
[5] D. E. Acosta *et al.* (CDF Collaboration), Phys. Rev. Lett. **95**, 102002 (2005).
[6] A. Abulencia *et al.* (CDF Collaboration), Phys. Rev. D **73**, 111103 (2006).
[7] C. Amsler *et al.* (Particle Data Group), Phys. Lett. B **667**, 1 (2008).
[8] S. S. D. Willenbrock and D. A. Dicus, Phys. Rev. D **34**, 155 (1986).
[9] B. W. Harris, E. Laenen, L. Phaf, Z. Sullivan, and S. Weinzierl, Phys. Rev. D **66**, 054024 (2002).
[10] Z. Sullivan, Phys. Rev. D **70**, 114012 (2004).
[11] N. Kidonakis, Phys. Rev. D **74**, 114012 (2006).
[12] N. Kidonakis, arXiv:0705.2431.
[13] N. Kidonakis, arXiv:0909.0037.
[14] N. Kidonakis, Phys. Rev. D **81**, 054028 (2010).
[15] LEP Electroweak Working Group, ALEPH, DELPHI Collaboration, L3 Collaboration, OPAL Collaboration, and SLD Collaboration, Phys. Rep. **427**, 257 (2006).
[16] J. Alwall *et al.*, Eur. Phys. J. C **49**, 791 (2007).
[17] T. M. P. Tait and C. P. Yuan, Phys. Rev. D **63**, 014018 (2000).
[18] K. A. Assamagan *et al.*, arXiv:hep-ph/0406152.
[19] N. Kidonakis and R. Vogt, Phys. Rev. D **68**, 114014 (2003).
[20] G. Mahlon and S. J. Parke, Phys. Rev. D **55**, 7249 (1997).
[21] T. Stelzer, Z. Sullivan, and S. Willenbrock, Phys. Rev. D **58**, 094021 (1998).
[22] V. M. Abazov *et al.* (D0 Collaboration), Phys. Rev. Lett. **98**, 181802 (2007).
[23] V. M. Abazov *et al.* (D0 Collaboration), Phys. Rev. D **78**, 012005 (2008).
[24] V. M. Abazov *et al.* (D0 Collaboration), Phys. Rev. Lett. **103**, 092001 (2009).
[25] V. M. Abazov *et al.* (D0 Collaboration), Phys. Lett. B **690**, 5 (2010).
[26] T. Aaltonen *et al.* (CDF Collaboration), Phys. Rev. Lett. **101**, 252001 (2008).
[27] T. Aaltonen *et al.* (CDF Collaboration), Phys. Rev. Lett. **103**, 092002 (2009).
[28] T. Aaltonen *et al.* (CDF Collaboration), Phys. Rev. D **81**, 072003 (2010).
[29] A. Abulencia *et al.* (CDF Collaboration), J. Phys. G **34**, 2457 (2007).
[30] D. E. Acosta *et al.* (CDF Collaboration), Phys. Rev. D **71**, 032001 (2005).
[31] D. E. Acosta *et al.* (CDF Collaboration), Phys. Rev. D **71**, 052003 (2005).
[32] C. S. Hill (CDF Collaboration), Nucl. Instrum. Methods Phys. Res., Sect. A **530**, 1 (2004).
[33] A. Sill (CDF Collaboration), Nucl. Instrum. Methods Phys. Res., Sect. A **447**, 1 (2000).
[34] A. A. Affolder *et al.* (CDF Collaboration), Nucl. Instrum. Methods Phys. Res., Sect. A **453**, 84 (2000).
[35] A. A. Affolder *et al.* (CDF Collaboration), Nucl. Instrum. Methods Phys. Res., Sect. A **526**, 249 (2004).
[36] L. Balka *et al.* (CDF Collaboration), Nucl. Instrum. Methods Phys. Res., Sect. A **267**, 272 (1988).
[37] M. G. Albrow *et al.* (CDF Collaboration), Nucl. Instrum. Methods Phys. Res., Sect. A **480**, 524 (2002).
[38] S. Bertolucci *et al.* (CDF Collaboration), Nucl. Instrum. Methods Phys. Res., Sect. A **267**, 301 (1988).
[39] F. Abe *et al.* (CDF Collaboration), Phys. Rev. Lett. **68**, 1104 (1992).
[40] G. Apollinari, K. Goulianos, P. Melese, and M. Lindgren, Nucl. Instrum. Methods Phys. Res., Sect. A **412**, 515 (1998).
[41] G. Ascoli *et al.*, Nucl. Instrum. Methods Phys. Res., Sect. A **268**, 33 (1988).
[42] R. Blair *et al.* (CDF Collaboration), Report No. FERMILAB-PUB-96-390-E, 1996.
[43] A. Artikov *et al.*, Nucl. Instrum. Methods Phys. Res., Sect. A **538**, 358 (2005).
[44] D. Acosta *et al.*, Nucl. Instrum. Methods Phys. Res., Sect. A **494**, 57 (2002).
[45] S. Klimenko, J. Konigsberg, and T. M. Liss, Report No. FERMILAB-FN-0741, 2003.
[46] E. J. Thomson *et al.*, IEEE Trans. Nucl. Sci. **49**, 1063 (2002).
[47] R. Downing *et al.*, Nucl. Instrum. Methods Phys. Res., Sect. A **570**, 36 (2007).
[48] G. Gomez-Ceballos *et al.*, Nucl. Instrum. Methods Phys. Res., Sect. A **518**, 522 (2004).
[49] A. Bhatti *et al.*, Nucl. Instrum. Methods Phys. Res., Sect. A **566**, 375 (2006).
[50] F. Maltoni and T. Stelzer, J. High Energy Phys. 02 (2003) 027.
[51] H. L. Lai *et al.* (CTEQ Collaboration), Eur. Phys. J. C **12**, 375 (2000).
[52] T. Sjöstrand *et al.*, Comput. Phys. Commun. **135**, 238 (2001).

[53] T. Sjöstrand, S. Mrenna, and P. Skands, J. High Energy Phys. 05 (2006) 026.
[54] Z. Sullivan, Phys. Rev. D **72**, 094034 (2005).
[55] E. E. Boos, V. E. Bunichev, L. V. Dudko, V. I. Savrin, and A. V. Sherstnev, Phys. At. Nucl. **69**, 1317 (2006).
[56] J. M. Campbell, R. Frederix, F. Maltoni, and F. Tramontano, Phys. Rev. Lett. **102**, 182003 (2009).
[57] J. M. Campbell, R. Frederix, F. Maltoni, and F. Tramontano, J. High Energy Phys. 10 (2009) 042.
[58] Y. L. Dokshitzer, Sov. Phys. JETP **46**, 641 (1977).
[59] V. N. Gribov and L. N. Lipatov, Sov. J. Nucl. Phys. **15**, 438 (1972).
[60] G. Altarelli and G. Parisi, Nucl. Phys. **B126**, 298 (1977).
[61] J. Lueck, diplom thesis, University of Karlsruhe, 2006, [Report No. FERMILAB-MASTERS-2006-01].
[62] J. Lueck, Ph.D. thesis, University of Karlsruhe, 2009, [Report No. FERMILAB-THESIS-2009-33].
[63] G. Abbiendi et al. (OPAL Collaboration), Eur. Phys. J. C **8**, 217 (1999).
[64] J. Donini et al., Nucl. Instrum. Methods Phys. Res., Sect. A **596**, 354 (2008).
[65] S. Jadach, Z. Was, R. Decker, and J. H. Kuhn, Comput. Phys. Commun. **76**, 361 (1993).
[66] R. Bonciani, S. Catani, M. L. Mangano, and P. Nason, Nucl. Phys. **B529**, 424 (1998).
[67] M. Cacciari, S. Frixione, M. L. Mangano, P. Nason, and G. Ridolfi, J. High Energy Phys. 04 (2004) 068.
[68] E. L. Berger and H. Contopanagos, arXiv:hep-ph/9706356.
[69] J. M. Campbell and R. K. Ellis, Phys. Rev. D **60**, 113006 (1999).
[70] M. L. Mangano, M. Moretti, F. Piccinini, R. Pittau, and A. D. Polosa, J. High Energy Phys. 07 (2003) 001.
[71] T. Aaltonen et al. (CDF Collaboration), Phys. Rev. Lett. **100**, 102001 (2008).
[72] Z. Bern, L. J. Dixon, D. A. Kosower, and S. Weinzierl, Nucl. Phys. **B489**, 3 (1997).
[73] Z. Bern, L. J. Dixon, and D. A. Kosower, Nucl. Phys. **B513**, 3 (1998).
[74] W. T. Giele, S. Keller, and E. Laenen, Nucl. Phys. B, Proc. Suppl. **51C**, 255 (1996).
[75] R. K. Ellis and S. Veseli, Phys. Rev. D **60**, 011501 (1999).
[76] F. Febres Cordero, L. Reina, and D. Wackeroth, Phys. Rev. D **74**, 034007 (2006).
[77] J. M. Campbell, R. K. Ellis, F. Maltoni, and S. Willenbrock, Phys. Rev. D **75**, 054015 (2007).
[78] J. M. Campbell et al., Phys. Rev. D **79**, 034023 (2009).
[79] F. F. Cordero, L. Reina, and D. Wackeroth, Phys. Rev. D **80**, 034015 (2009).
[80] T. Aaltonen et al. (CDF Collaboration), Phys. Rev. D **77**, 011108 (2008).
[81] T. Aaltonen et al. (CDF Collaboration), Phys. Rev. Lett. **100**, 091803 (2008).
[82] S. Richter, Ph.D. thesis, University of Karlsruhe, 2007, [Report No. FERMILAB-THESIS-2007-35].
[83] M. Feindt and U. Kerzel, Nucl. Instrum. Methods Phys. Res., Sect. A **559**, 190 (2006).
[84] C. P. Yuan, Phys. Rev. D **41**, 42 (1990).
[85] K. Ackerstaff et al. (OPAL Collaboration), Eur. Phys. J. C **1**, 425 (1998).
[86] S. R. Budd, Ph.D. thesis, University of Illinois, 2008, [Report No. FERMILAB-THESIS-2008-41].
[87] K. Nakamura, Ph.D. thesis, University of Tsukuba, 2009, [Report No. FERMILAB-THESIS-2009-13].
[88] P. J. Dong, Ph.D. thesis, University of California at Los Angeles, 2008, [Report No. FERMILAB-THESIS-2008-12].
[89] I. Murayama, H. Watanabe, and K. Hagiwara, Tech. Report No. 91-11, KEK, 1992.
[90] A. Genz and A. Malik, J. Comput. Appl. Math. **6**, 295 (1980), implemented as CERNLIB algorithm D120, documented in http://wwwasdoc.web.cern.ch/wwwasdoc/shortwrupsdir/d151/top.html.
[91] T. Hahn, Comput. Phys. Commun. **168**, 78 (2005).
[92] J. Neyman and E. Pearson, Phil. Trans. R. Soc. A **31**, 289 (1933).
[93] A. Papaikonomou, Ph.D. thesis, University of Karlsruhe, 2009, [Report No. FERMILAB-THESIS-2009-21].
[94] A. Hocker et al., Proc Sci, ACAT (2007) 040.
[95] B. Casal Larana, Ph.D. thesis, University of Cantabria, 2010, [Report No. FERMILAB-THESIS-2010-04].
[96] C. Gini, in Memorie di Metodologia Statistica, edited by E. Pizetti and T. Savemini, (Libreria Eredi Virgilio Veschi, Rome, 1955).
[97] Y. Freund and R. Schapire, J. Comput. Syst. Sci. **55**, 119 (1997).
[98] L. Breiman, J. Friedman, R. Olshen, and C. Stone, Classification and Regression Trees (Chapman & Hall/CRC Press, Boca Raton, 1984).
[99] A. Abulencia et al. (CDF Collaboration), Phys. Rev. D **73**, 032003 (2006).
[100] A. D. Martin, R. G. Roberts, W. J. Stirling, and R. S. Thorne, Eur. Phys. J. C **4**, 463 (1998).
[101] Please see p. 234 of Ref. [7].
[102] T. Aaltonen et al. (CDF Collaboration), Phys. Rev. Lett. **102**, 021802 (2009).
[103] K. Stanley and R. Miikkulainen, Evolutionary computation **10**, 99 (2002).
[104] Tevatron Electroweak Working Group, arXiv:0908.2171.
[105] V. M. Abazov et al. (D0 Collaboration), Phys. Lett. B **682**, 363 (2010).